CHARACTERIZATION AND MEASUREMENT OF MICROSTRUCTURAL FEATURES IN LASER PROCESSED ALLOYS

by

Kathryn A. Small

A dissertation submitted to Johns Hopkins University in conformity with the requirements for

the degree of Doctor of Philosophy

Baltimore, Maryland

June 2021

Abstract

Laser processes such as laser-powder bed fusion, surface laser polishing, and laser engraving are under intense investigation due to their great potential in design and manufacturing of complex structural materials. The localized thermal environment including large thermal gradients and fast cooling rates inherent in laser processing result in unique microstructures and mechanical properties which are not currently predictable. Residual stress is a prominent defect in laser processed metals and has resulted in decreased mechanical life for AM parts, while phase transformations which accompany laser processes have been reported to decrease certain mechanical properties even while improving properties such as corrosion resistance in steels. The absence of measurement techniques for microscale residual stress has inhibited the full characterization of the microstructure of laser processed alloys, although its magnitude and distribution are known to affect component failure. The microstructure of laser processed alloys typically contains non-equilibrium dislocation cells due to cellular solidification at steep thermal gradients and fast solidification rates. These cells have been reported to improve mechanical properties, however their non-equilibrium nature means that they can be processed away in certain conditions. The evolution of these cells is not fully understood, although recent results suggest that residual strain is crucial to their formation during laser additive manufacturing. The characterization of microscale elastic strain and dislocation density combined with statistical analysis and thermal simulation enables the establishment of processing-structure relationships during laser processing.

In this thesis, electron microscopy combined with thermal simulations is used to describe the evolution of elastic strain and non-equilibrium dislocation cells in laser processed metals. A method of microscale elastic strain calculation is optimized for laser processed alloys and is used to connect the thermal gradients in additive manufacturing to the evolution of dislocation cell structures during processing. The relationship between cell structure evolution and elastic strain distribution during laser processing impacts the final material and mechanical properties of a component, and the description of that relationship move toward improved predictive capabilities of laser processing.

Advisor: Dr. Mitra Taheri

Readers: Dr. Jaafar El-Awady, Dr. James Spicer, Dr. Jonah Erlebacher, Dr. Andrew Birnbaum

Acknowledgements

Dr. Mitra Taheri, thank you for pulling me into the world of microscopy and helping me to get the best out of the results I had, all of the great opportunities I've had over the past few years were due to your guidance.

To all of the members of my committee, thank you for taking the time to listen to and improve the results from the experiments I've done. Particularly Dr. Jaafar El-Awady and Dr. Andrew Birnbaum for helping to focus the characterization techniques toward the improvement of the additive manufacturing community.

My thanks also go to all of the collaborators and co-authors I've worked with. Dr. David Fullwood and his student Zach Clayburn from Brigham Young University were essential to the optimization of elastic strain calculation in AM alloys. The teams at Army ARDEC – Ryan Carpenter, Matthew Clemente and Elias Jelis, Hoeganaes Corp. – Alex Zwiren and George Bernhard, for fabrication of the BJ3DP samples, and NASA LRC – Jacob Hocchalter, for fabrication of EBF3 samples. Dr. Anna Carlsson at ThermoFisher Scientific, thank you for TEM data collection and analysis. Dr. Ian McCue at JHU APL, thank you for cheerfully running CFD simulations, even on short notice, and patiently teaching me about the different parameters and conditions for thermal simulations. Dr. Markus Sudmanns, thank you for the same thing, only with DDD simulations. Kat Johnston and Ian Donaldson, thank you for being patient while wrestling our results into a coherent manuscript.

My friends in the Dynamic Characterization Group all helped me enormously at different times and with different aspects of the work presented here. James Nathaniel, Elaf Anber,

Cassandra Pate, David Beaudry, Emily Hopkins, Nick Gigliotti, and particularly Dan Foley and Caleb Andrews, thank you for helping with TEM analysis and elastic strain calculation.

The administrative staff in the DMSE department of JHU were incredibly helpful through the move from Drexel to Johns Hopkins, Ellen Libao and Jeanine Majewski – thank you so much for your help with every aspect of the transition, and with preparing me for being the first from our group to graduate from JHU.

Erin Sampson of Five Parks Yoga – thank you for all you did for me virtually, unknowingly, posting videos online allowing me to relax, workout, and improve my focus during the past few years.

All of my friends and family are integral to my continued sanity and success. My parents, Carline Anderson and William Small, thank you for helping me with (literally) every aspect of life. My siblings Leanne Fox, Steven Small and Dylan Anderson did a tremendous amount for me during my graduate school years, as did Jeff Fox, Nancy Trieu and Anatoly Klypin. My nieces and nephews Henry Fox, Tycho Trieu, Betty Fox and Jorani Small were some of the most fun and best distractions to have around during stressful times. Finally, Ryan DeMott helped me in every way imaginable during the production of these results and this thesis – thank you for being patient and kind when I wasn't.

Table of Contents

List of Tables

List of Figures

Chapter 1. Introduction

Overview

The thermal environment of metal fabrication is known to affect the final microstructure, and therefore the final material properties, of a component. Varying the cooling rates and thermal gradients can influence features including grain size, homogeneity, dislocation content and thereby impact the fracture or tensile properties of the final component. Laser welding, for example, is a process which imparts high temperatures, often above the melting temperature, to the metals it is joining and is accompanied by high cooling rates on the order of 10^5-10^7K/s. Laser methods including welding, alloying, cladding and additive manufacturing therefore result in often heterogeneous and unpredictable microstructures leading to varying performance of structural components. Despite the difficulties present in laser processes, they have great potential for fabricating complex geometries and precision modification of local properties. Laser additive manufacturing methods including laser-powder bed fabrication (L-PBF) in particular have therefore come under increased scrutiny over the last few decades, with the hope that bulk components may someday be manufactured faster and with less waste than by conventional practices.

L-PBF still has several hurdles to overcome before it is a commercially viable processing technique, and other laser and additive processes are still not well understood. Residual stress and strain is a significant source of failure in AM parts; however, the characterization and manipulation of this feature is difficult, particularly on the meso- and microscales. This thesis aims to use a novel strain characterization technique and statistical analysis of unique microstructures present in laser processed nickel and steel alloys to demonstrate mechanisms of microstructural evolution and improve predictive capabilities of these processes.

The remainder of this introduction will discuss the thermal environments present in laser processing techniques as well as other additive manufacturing (AM) processes, including their unique microstructures and present understanding of residual stress and strain and its characterization. This introduction will also introduce the simulation methods and predictive technologies in use and under development for laser additive techniques.

Additive Manufacturing and Laser Processes

Additive manufacturing (AM, also termed 3D printing) was first introduced in 1987 by 3D Systems, which used a stereolithography (SL) system to create 3D objects by melting layers of polymers together[1]. Decades of development later, AM has evolved to be nearly ubiquitous in research and development of industries as varied as sports and transportation, growing into a $11.8 billion market in 2019 and projected to reach $35.6 billion in 2024 [2]. In addition to SL systems, there is a myriad of AM techniques utilizing a variety of source materials and binding methods including visible and UV light and fusion of filaments for polymeric production; the focus in this thesis is on laser processes and AM of metals [1,3]. The attractiveness of AM to industries such as aerospace and medicine is due to its potential for fast production, speedy design and testing processes, and the possibility of producing complex parts as single entities, instead of piece by piece through conventional manufacturing methods [4–6]. Additionally, there is necessity in some industries for localized functionality which AM has the ability to impart. Because the laser or electron beam is a highly localized heat source, only the material directly in its path may be affected by the thermal cycling and rapid cooling rates, and the layer by layer process of AM results in unique thermal gradients and repetitive thermal cycles not seen in conventional techniques. This can give rise to local misorientations and

heterogeneous microstructures which give rise to heterogeneous mechanical properties [7,8]. However, there are still barriers to widespread commercialization of AM methods including the lack of reliability and the difficulty in qualification of final components, which has led to the belief that the control of microstructures is key to achieving the desired properties in AM components [9,10].

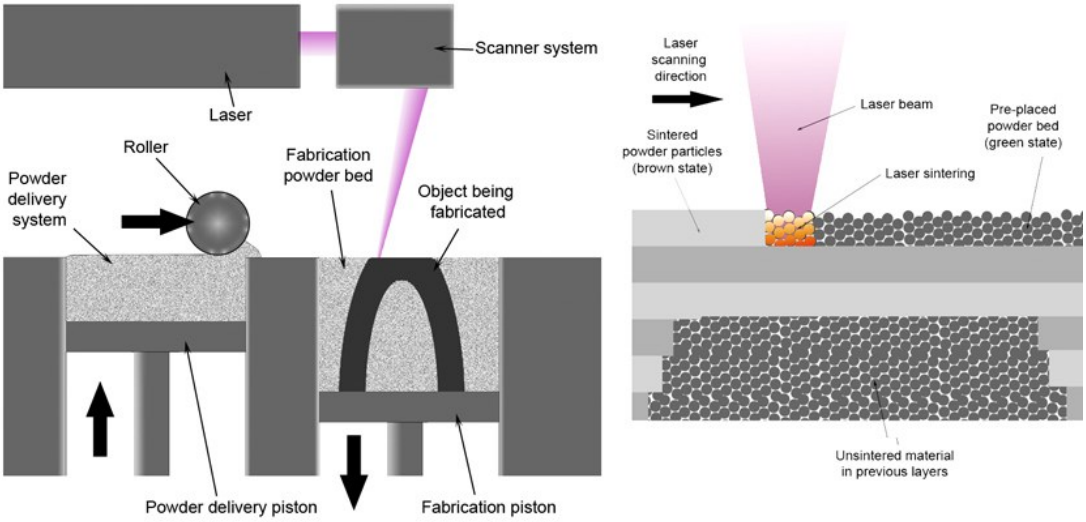

Figure 1-1. Schematic of laser additive manufacturing process [By Materialgeeza - Own work, CC BY-SA 3.0, https://commons.wikimedia.org/w/index.php?curid=4032088]

AM methods utilize a CAD model to print a 3D part layer by layer from raw materials in the form of powder or wire (Figure 1-1), thereby enabling fabrication of complex geometries using a single manufacturing process with minimal waste. Table 1-1 lists some of the most investigated AM methods, including wire and powder feedstock with laser, electron beam, or binder jet as the binding method. Each AM technique has unique processing parameters which result in varying microstructures and mechanical properties, and these parameters have not

been fully optimized for reliable material properties of complex metal parts. Advanced characterization of AM components, including in-situ monitoring of the AM process, is therefore an intense area of investigation for establishment of AM techniques [5,9,11–14]. Laser and electron based additive techniques like laser-powder bed fusion (L-PBF), electron beam melting (EBM) and direct energy deposition (DED) result in microstructures and material properties that differ from those of cast or wrought alloys; parameters including build direction, laser power, laser or electron beam shape, scan speed and others can have a significant effect on various properties [15–19].

Table 1-1. Powder and wire AM techniques using binder jet, laser, and e-beam binding methods

AM Process	Raw Material	Processing Parameters	Typical Micro/structures	Selected References
Laser-powder bed fusion (L-PBF)	Powder	Laser speed, beam shape, laser power, hatch spacing, layer thickness, laser path	Columnar grains elongated in the build direction, intragranular misorientation, dislocation cells, residual stress	[20–22]
Binder Jet 3D Printing (BJ3DP)	Powder	Binder saturation, sintering schedule powder diameter, layer thickness	Equiaxed, large grains of uniform orientation, porosity, precipitates	[23–26]
Electron Beam Melting (EBM)	Powder	e-beam voltage, current, layer thickness, scan speed	Columnar grains elongated in the build direction, porosity, low angle GBs, high dislocation density	[27–29]
Electron Beam Freeform Fabrication (EBF3)	Wire	e-beam voltage, wire diameter, deposition rate, current	Wavy GBs, high dislocation density, surface roughness, dendritic grains	[30–33]
Direct Energy Deposition (DED)	Wire/Powder	Laser vs. e-beam, speed, voltage, wire diameter, deposition rate, inert atmosphere vs. vacuum	Surface roughness, columnar grains, dislocation cells, residual stress	[34–36]

The increasing use of AM has resulted in a myriad of techniques, each differing from the next by source material or binding agent. AM techniques used for printing metal components can vary widely in their thermal environment and processing parameters, and two components built using the same AM machine can result in structural and geometrical differences by varying

the process parameters. Laser additive methods, for example, usually result in columnar grains in the direction of the build due to the high thermal gradient in this direction, while binder jet printing results in largely equiaxed structures in which porosity or precipitates are perhaps the most problematic feature [refs]. This thesis is focused mainly on laser powder bed fusion (L-PBF), however, in chapter 3, a comparison between L-PBF, binder jet 3D printer (BJ3DP) and electron beam freeform fabrication (EBF3) is presented in order to gain an understanding of the variations in thermal gradients between methods and their impacts on microstructural features and their organization.

Binder Jet 3D Printing (BJ3DP)

BJ3DP is perhaps the least intense AM process in terms of thermal environment. In this AM technique, metal powder feedstock is printed layer-by-layer and a liquid binder (here polyethylene glycol) is applied in the desired 2D pattern on every layer. The resulting 'green part' is very fragile as the powder is held together only by liquid binder and therefore must be sintered in a low temperature oven to strengthen the part [24]. After the low temperature anneal, the 'brown part' is sintered in a high temperature furnace to burn off the binder and increase the density of the component. The primary densification mechanism in BJ3DP is solidus-liquidus phase sintering (SLPS) in which a liquid forms inside the alloyed particle and spreads to particle contacts, causing a viscous flow which leads to grain growth during sintering and a grain structure similar to casting [24,37–39]. BJ3DP is an area of great interest for structural alloys due to the absence of a high energy laser or electron beam [11,23], and thus, lacks steep thermal gradients. The BJ3DP process has the most even thermal gradients and the slowest cooling rate of all three processes studied in this thesis, and it has been shown to result

in equiaxed microstructures with little intragranular misorientation in Ni superalloys [26,40]. However, this AM method is highly dependent on the powder size and binder saturation and is often complicated by porosity in final components which can have a detrimental effect on the mechanical properties of the final part and often requires post-processing steps such as hot isostatic pressing (HIP) [25].

Electron Beam Freeform Fabrication (EBF3)

Electron beam freeform fabrication (EBF3) is an additive technique developed by NASA Langley Research Center (LRC) in an effort to design a fabrication process free from powder for use in low gravity environments [41,42]. By using a feed material of metal wire and an electron beam, 3D components can be built quickly in a vacuum and with little waste material when compared to conventional manufacturing processes [30,31]. However, wire also leads to less accurate geometries and therefore EBF3 has been found to be most suitable for large, simple geometries [43]. During EBF3, a high-power stationary electron beam welds metal wire together on a preheated build plate that is mobile in three dimensions. Variations in microstructure have been accomplished by changing the parameters of the EBF3 process, for instance a slow build plate translation results in large grained dendritic microstructures, expected for processes with slow cooling rates [32]. Process maps have been used previously for single bead Ti-6Al-4V fabricated by EBF3, where beam power and plate velocity are used to control melt pool dimensions toward a predicted grain morphology [33].

Laser-Powder Bed Fabrication (L-PBF)

L-PBF is a more commonly used AM process than EBF3 in which a high-powered mobile laser in an inert environment is used to partially melt metal powder into a desired geometry. L-

PBF results in higher thermal gradients and faster cooling rates than are typical in EBF3 or BJ3DP, usually resulting in smaller grains and potentially undesirable mechanical properties including residual strains [21]. The cooling rate during L-PBF often surpasses the threshold for rapid solidification (RS, defined as at least 10^3 K/s), giving rise to non-equilibrium solidification processes and structures [refs]. RS can lead to martensitic transformations and increased residual stress 'frozen' into the microstructure of a component. The cyclic remelting and the layer by layer nature of many additive processes result in the well-known anisotropic microstructure and properties of AM components. Several studies of the anisotropy inherent in AM structures have found variations in microstructure and properties [44–47].

A layer is deposited once but may be remelted up to ten times and exposed to the heat affected zone (HAZ) more times than that, giving rise to microstructural evolution at a fixed position as the build continues. With a heat source such as a laser or electron beam, the temperatures can be very high, surpassing the melting temperature of the alloy and giving rise to a liquid melt pool (Figure 1-2). L-PBF is a complex process with a number of processing parameters which could alter the thermal gradients, cooling rates and effecting the character of the melt pool; however, this method is more attractive to some than EBF3 in part because L-PBF is more precise and results in parts with better manufacturing tolerances [22,48].While L-PBF has high potential for improving manufacturing cost and efficiency, the design of reliable L-PBF parts is still quite lengthy and expensive. This is because until recently the design and research of components fabricated by L-PBF consisted mainly of iterative design (Figure X. a schematic of iterative design vs. a schematic of model-based design).

L-PBF has been thoroughly investigated in a variety of alloy systems including stainless steels [34,49–51], Ti-6-4 [52–55], Ni alloys [17,56–59], and high and medium entropy alloys [60,61].The microstructure resulting from L-PBF is highly dependent on melt pool shape and energy density; Agrawal et al. found that at increased energy densities the grain size and aspect ratio increased, and texture was more random in 316L stainless steel [20] while Shi et al. used microstructural simulations to find that the shape of the laser beam has a strong effect on the shape of the melt pool and resulting grain growth and texture [19]. The residual strains imposed by the L-PBF process can be large enough to induce warping in the component after it is released from the build plate and can cause failed tolerances and mechanical failures in the absence of loading [22].

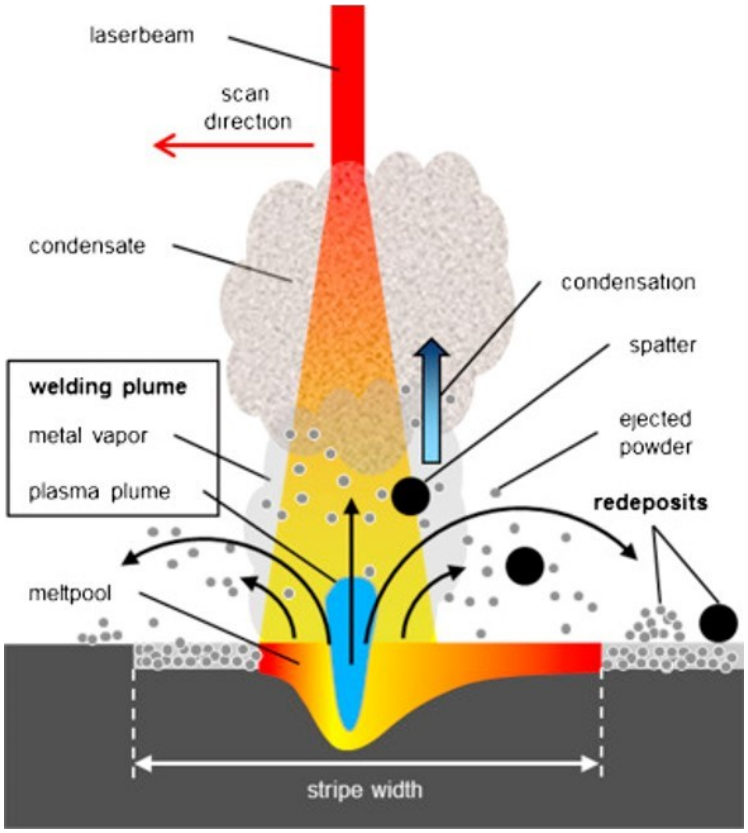

Figure 1-2. Schematic of possible process by-products in laser AM [62]

Dislocation and non-equilibrium structures have been seen in L-PBF fabricated components of steel and Nickel alloys and have been theorized to improve mechanical properties as well as relieve residual stress introduced during cooling [refs]. However, despite the level of interest in additive manufacturing and precision microstructural modification, the mechanisms of solidification and dislocation organization at extreme temperatures and solidification rates are little understood. The cooling rates during L-PBF fabrication have been found to range from 10^4-10^6 K/s or higher, well above the necessary cooling rate for rapid solidification, and a microstructure typical of RS has been observed previously in L-PBF fabricated IN625 [63–66]. The thermal environment of L-PBF also includes steep thermal gradients and repetitive heating by the tracking laser, each of which contributes to complex, non-equilibrium microstructures and diverse material properties [63,64,67,68]. The microstructure induced by L-PBF in several alloys has been observed to include metastable cellular structures within grains (**Error! Reference source not found.**-3) [69–71]. These cellular b oundaries have a high density of dislocations and solute elements ejected during solidification and the structures have been shown to decompose with annealing. There are many competing theories for the mechanism of evolution of these metastable subgrain structures; it is likely that the driving forces for their formation are dependent on alloy chemistry, with theories including both chemical supersaturation at solidification fronts and thermally induced residual elastic stresses [70–72]. Additionally, the effects of re-melting and the heat affected zone (HAZ) of subsequent laser tracking increases the complexity of the solidification environment and the extent of microstructural evolution during these laser passes is unknown.

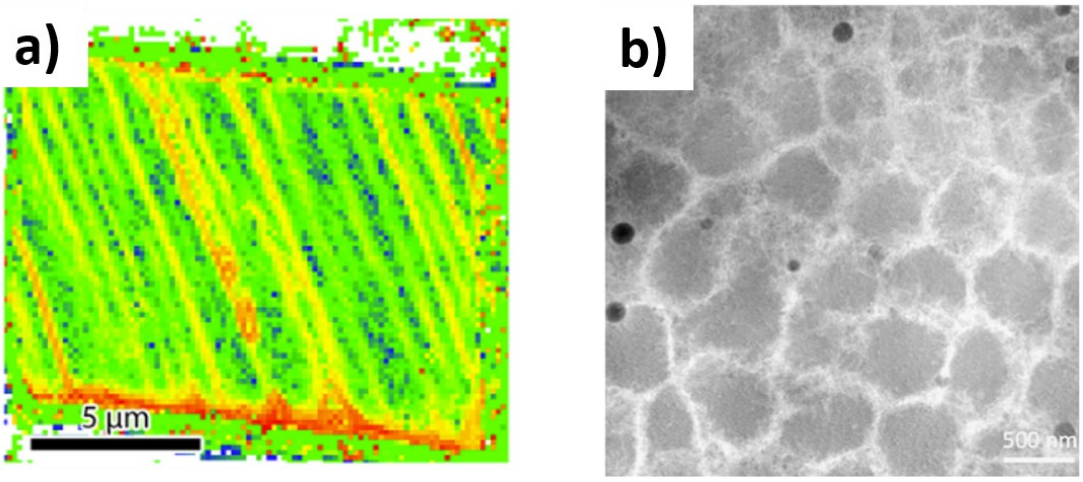

Figure 1-3. Intragranular cell structures bound by high dislocation density in IN718 (a) and stainless steel 316L (b). Adapted from [69] (a) and [73] (b).

Surface Laser Processes

Laser processing of metals is an active area of research due to the desire for precision modification of microstructures and the resulting local functionality of a component [19,74,75]. Different surface laser processes may be utilized for desired results; for example, vaporization of component surfaces with a laser enables welding and cutting, while surface melting may result in transformation hardening. Additionally, laser surface modification (LSM) has been widely used in tool steels in an effort to increase their performance by altering the surface structure through laser treatment [76,77]. Laser processes such as laser polishing have emerged as structure and property tailoring methods; laser surface treatment was found to significantly improve corrosion resistance in Ti-6Al-4V as well as producing a smooth, crack free surface, while laser surface quenching was used to eliminate selective phase corrosion in Nickel-Aluminum Bronze by transforming the surface layer to a single phase, fine grained structure [78,79]. Laser peening has been reported to result in deeper compressive stresses than shot peening, but results in a generally less smooth surface finish [80].

Surface laser processing is also useful for the post-treatment of many AM parts for either enhanced mechanical properties or due to surface roughness, a common result of AM processes which can include unmelted particles or the staircase effect due to layer-by-layer fabrication [81]. It has been reported that, in addition to resulting in a substantially reduced surface roughness, laser polishing increased tensile strength and dislocation density, including cellular substructures, on the surface of stainless steel 316L fabricated by laser AM [82].

The rapid solidification inherent in laser AM and laser surface processes gives rise to changes in orientation as high as 15° in a single grain. These intragranular misorientations are accommodated by a high density of geometrically necessary dislocations (GNDs) or by increased elastic strain within the lattice structure. The measurement of stress and strain on the microscale in these materials is of interest because of the known effects of residual stresses on mechanical properties of AM components [83–85]; theories surrounding the mechanisms of dislocation cell formation during AM and the knowledge that microstructural strain gradients inform microstructural evolution have increased the need for characterization of elastic strain on the microscale.

Residual Stress in Laser Processed Alloys

Residual stresses in AM are a well-known problem that affect final tolerances and mechanical performance of components [7,86–88]. The development of residual stresses during laser AM can result in bulk distortion of the final component as well as decreased mechanical properties, particularly if large tensile stresses exist within the material. However, the prediction of these stresses is so far not practical and their characterization is difficult, especially when the stress is on the subgrain scale.

Residual stresses are inhomogeneous, self-equilibrating stresses that are present in a material in the absence of any external force. As the body remains at rest these stresses sum to zero over sufficient length scales. The classification of residual stresses is based on the length scale over which they equilibrate [89–92]:

- Type I stresses, or macrostresses, are bulk scale stresses which can be nearly homogeneous over large length scales in the hundreds of μm – mm range, and have an equilibrating length of several grains.
- Type II stresses, called homogeneous microstresses, are equilibrated over a few grains, e.g. in the tens – hundreds of μm range.
- Type III stresses, or inhomogeneous microstresses, equilibrate over subgrain length scales (nm-several μm) but are inhomogeneous over submicroscopic areas.

Figure 1-4 gives a demonstration of the different strains in a material around grain boundaries. Type I stresses exhibit a profile which is an average of Type II and III stresses, while the Type II stress profile is an average of the Type III stresses. In Figure 1-4, it is made clear that a characterization of type I stress leaves out the nuances of types II and III, and therefore is not a complete characterization of the residual stress of a component. Although bulk scale stresses are often the feature of interest to engineers, failure of technical components starts on the microscale, meaning that microstresses are at least as important as macrostresses. Despite their importance, type III stresses are not the subject of many investigations, primarily because their characterization is quite difficult [88,90].

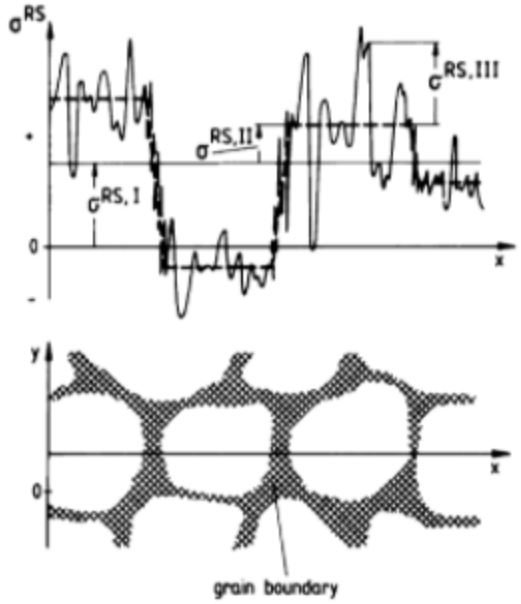

Figure 1-4. Types of residual stress classified by length over which they equilibrate. [67]

The reduction of residual stress during build has been an active area of investigation and there have been several attempts to reduced residual stress and distortion in AM. The laser scan strategy is known to impact the level of residual stress in a component, and so different scanning strategies have been attempted to manage the level of stress in a finished component [67]. Parry et al. used single layer simulations to determine the effect of unidirectional vs. alternating direction scan strategy on the von Mises stress distribution in Ti-6Al-4V (Figure 1-5).

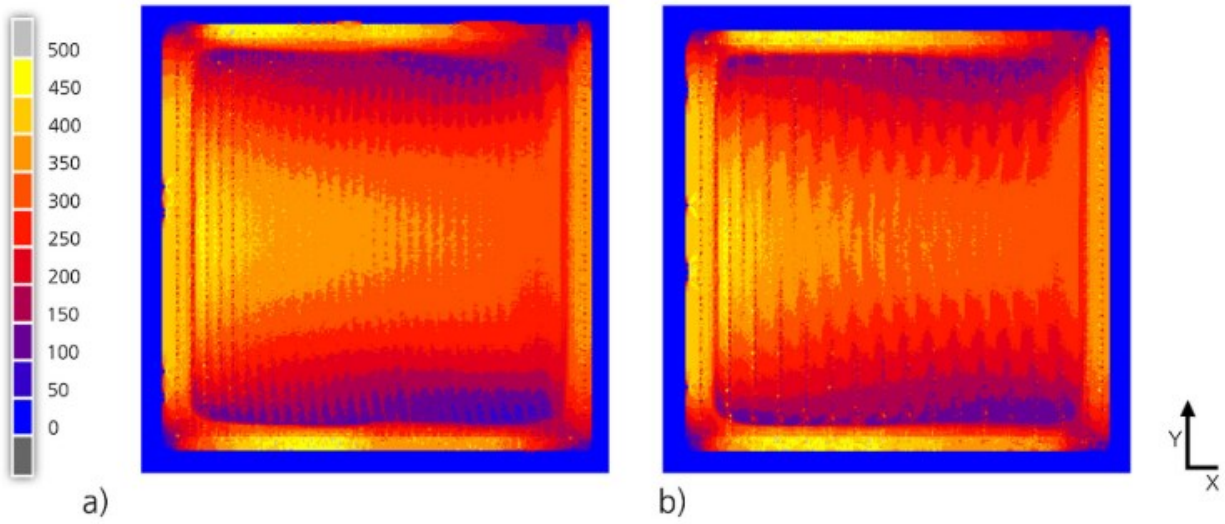

Figure 1-5. Simulated von Mises stress in Ti-6Al-4V using a) unidirection and b) alternating laser scan strategies [93]

Their findings demonstrated no significant difference in the magnitude of type II stresses between the two laser scan strategies, but a remarkable difference in the distribution of von Mises stresses. Rather, scan vector length was seen to have a greater impact on the level of residual stress, resulting in higher levels of stress in larger components [93]. Other experiments have found that island scanning strategies more effectively reduce the levels of residual stress in AM components [67,94]. The inclusion of support structures during fabrication has also been found to have an impact on residual stresses in laser AM built components, with contradictory results depending on the material and geometry. van Zyl et al. found that using a support structure decreased the residual stress measured by XRD in a Ti-6Al-4V sample, while Salmi et al. reported that including support structures during SLM of AlSi10Mg resulted in increased levels of stress before and after heat treatment, due to the added constraints of the supports [95,96]. The experimental efforts to reduce residual stress have resulted in the broad understanding that the thermal gradient, specifically the localized heat source of the laser, has

the greatest impact on residual stresses (Figure 1-6). The first mechanism of residual stress introduction by the laser is called thermal gradient mechanism (TGM). TGM results from the constraints of the lower, unmelted layers on the top layer being melted by the laser. The expansion of the top layer is prevented by the bottom layer, resulting in compressive stresses and a bending away from the laser beam. During cooling, the bottom layer once again inhibits the top layer, resulting in tensile stresses in the melt pool and compressive stresses in the bottom layer [67].

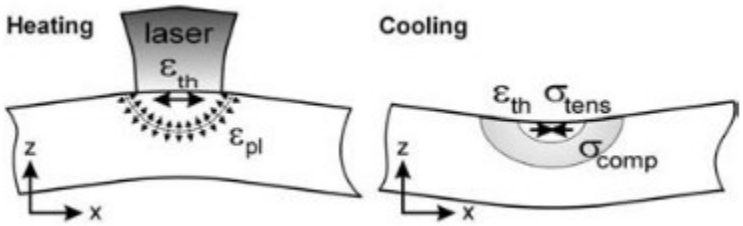

Figure 1-6. Thermal gradient mechanism (TGM) of residual stress introduction in laser processed metals [67]

The effects of trapped strains in AM material are widely considered detrimental, although compressive strains can be beneficial to the material properties of a component [90]. Residual strains during laser processing can result in large defects such as cracks as well as microcracking (Figure 1-7). Vrancken, et al. found that the high ductile to brittle transition temperature (DBTT) in W combined with the microscale residual stresses induced during SLM result in severe microcracking during processing [97]. In less brittle materials, the microscale residual stresses may be trapped during processing without inducing mechanical deformation,

however the level and distribution of type III strains is an important consideration in the final material properties of laser processed metals [98].

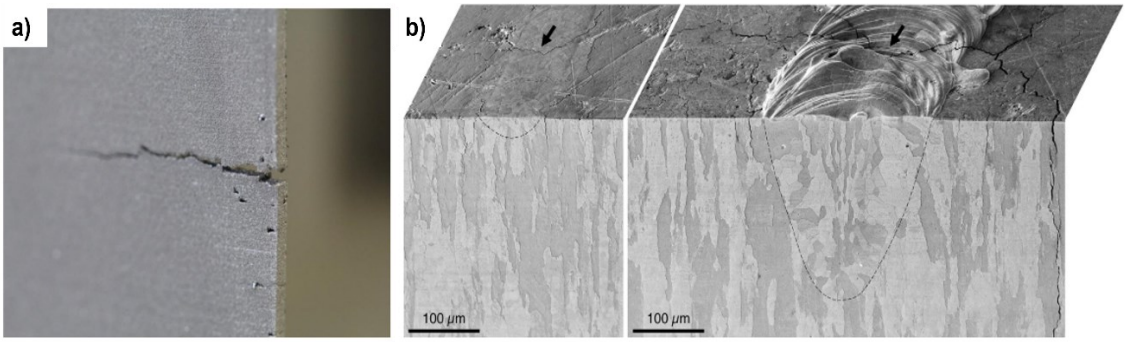

Figure 1-7. a) Crack induced during SLM of Ti-6Al-4V [93] and b) microcracking during SLM of W [97] both caused by residual stress

Much of the investigation into residual stress has been done using simulations of laser processes, due to the difficulty of measurement of type III strains and the specialized equipment necessary to measure type II strains. However, type III strains are components of type II and type I strains which result in deformation and loss of mechanical life, and their calculation is necessary if the reduction or manipulation of residual stress as a whole is to be optimized during laser processes. Due to the dependence of residual stress and strain on the thermal environment during laser processing, these properties are as anisotropic as other microstructural features, and the magnitude and distribution of strain varies throughout a build. The full characterization of laser processed metals should include type III stresses and strains if AM component properties are to be reliably engineered. Chapter 3 of this thesis details and optimized a technique to calculate type III residual strains in laser processed metals in order to arrive at a full characterization of the microstructure of these components.

Dislocation Cells in Laser Processed Alloys

The presence of dislocation cells in laser processed alloys is due to cellular solidification during rapid solidification of the alloy, depending on the thermal gradient, *G,* and the cooling rate, *R* [99]. The rate of solidification can be calculated based on cell spacing, and these cells usually grow in the direction of fastest solidification (for fcc materials such as Ni alloys and stainless steels, this is in the <100> directions) [100].

Murr et al. [101] demonstrated the different microstructures inherent in EBM vs. SLM alloys including steels and Inconel. IN625 fabricated by SLM exhibited dislocation cell structures similar to those found in 316L and accompanied by γ" nano-precipitates (Figure 1-8).

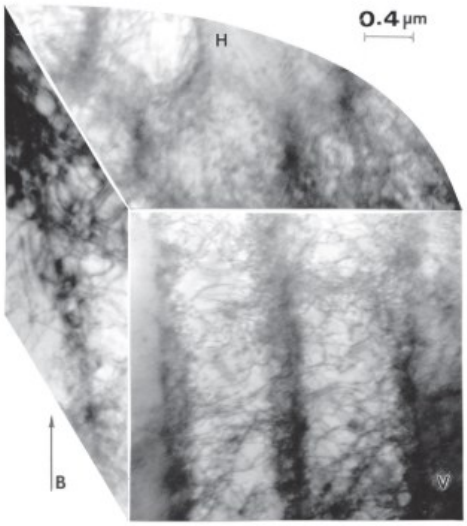

Figure 1-8 Microstructure of SLM fabricated IN625 showing dislocation cells aligned perpendicular to (110) orientation. [101]

Bertsch et al. [34] shows SLM 316L dislocation cells and uses 1D, 2D and 3D builds to isolate thermal strain as the mechanism of evolution. The dislocation cells became more

organized and increased in size with additional constraints (i.e. in the 3D build), suggesting that the trapped strain induced cell growth. Misorientations were not present at all dislocation cell walls, therefore it is not considered necessary for misorientations to accommodate a high density of dislocations (Figure 1-9).

Dislocation cells have been reported to impact bulk level mechanical properties of AM metals. Li et al. [102] investigated the role of dislocation cell sizes on the mechanical properties of L-PBF 316L. Micropillars were subjected to compression testing and it was found that the yield strengths of micro-pillars were independent on cell size. Instead, it is suggested that the dislocation density of the cell walls is the greatest influence on yield strength.

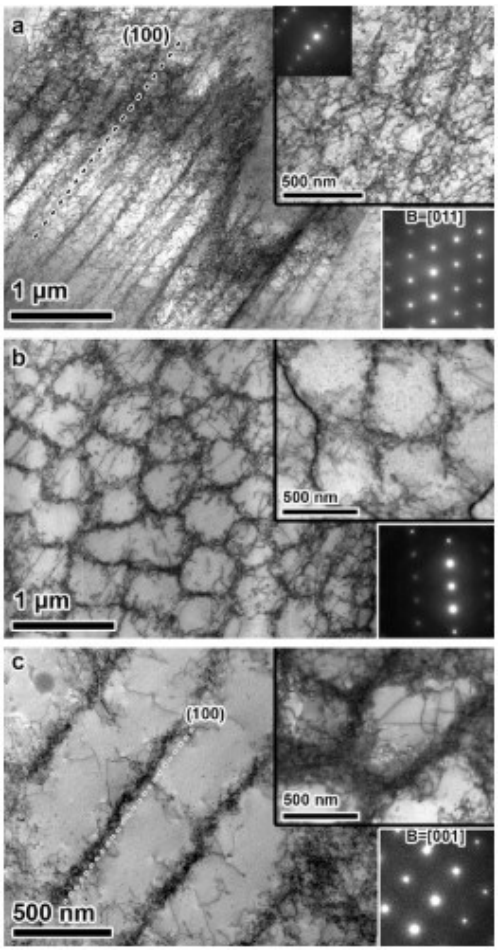

Figure 1-9. Increased dislocation density and cell size with increased dimensionality of SLM SS 316L build. Adapted from [34].

Krakhmalev et al. [103] performed hardness testing on as-build and heat treated SLM 316L and cell structures began to disappear around 900C. The hardness gradually decreased with increased recovery, suggesting that the presence of dislocation structures increases the hardness in this alloy. Cellular solidification is accompanied by microsegregation of alloying elements at cell boundaries [104]. The dislocation cells reported in AM fabricated metals are consistent with this, with increased Nb and Mo present at cell boundaries in Ni alloys, and increased Cr and Mo at cell walls in stainless steel 316L [49,58]. However, computational models have suggested that in homogeneous solidification dislocation cells can still form,

meaning that segregation may not be necessary for the formation of cell structures [99]. The cell structures observed in Ni alloys and steels formed by cellular solidification have been generally reported as growing along the [001] orientation (as shown in Figure 1-9). Voisin, et al demonstrated that when looking down the [001] direction, these dendrites/cells appear equiaxed with an average diameter of 650nm, but when intercepted with a {111} plane their diameter increases to 1133nm, a more than 50% increase. Our findings in Chapter 5 add to the results showing that these cells grow along the [001] orientation in IN625, and that there is Nb microsegregation in the cell boundaries.

The effect of AM microstructures on mechanical properties is an active area of research, however the characterization of microscale elastic strain has so far not been perfected. Optimizing the characterization and analysis of microstrain and its relationship to dislocation density and other microstructural features is integral to defining processing maps which can be used for fabrication of desired structures using AM techniques. So far, elastic strain in AM has been characterized on the bulk and grain scales (types I and II, respectively) while subgrain strain is less understood. However, it is known that premature microstructural yielding can be caused by type III strains, therefore it is necessary to quantify this feature and its impact on structure and properties. Likewise, dislocation cells are an area of interest with known effects on bulk level mechanical properties. However, the non-equilibrium nature of these structures means that they can be processed away in certain conditions. The characterization of the spatiotemporal variations in cell morphology will improve understanding and the ability to manipulate this feature for optimum mechanical properties.

Characterization Methods

Calculation of residual stresses, whether by destructive or non-destructive methods, is achieved indirectly by the measurement of strain and the use of elastic constants in the stress-strain relationship described by Hooke's Law [92,105]. In the past few decades, diffraction based techniques have gained popularity in the calculation of residual stress due to their reliability and, in some cases, their non-destructive nature [106]. Destructive, non-diffraction based methods such as hole drilling rely on the relaxation of residual strain in a component during the removal of material and the measurement of the change in geometry [107]. Non-destructive, diffraction based techniques include neutron and X-ray diffraction, both of which rely on Bragg's law of diffraction to determine the lattice strain in crystals from a shift in the scattering angle [108], while elastic strain measurement of electron backscatter diffraction (EBSD) data is a destructive, diffractive technique with the spatial resolution required to measure type III strains [109–111]. The elastic strains present in crystalline materials are usually small, on the order of 10^{-3}-10^{-4}, so extremely good strain resolution is required to accurately measure them; additionally, the spatial resolution of the method determines what type of elastic strain (I, II, or III) is measurable. Each diffractive technique has different limits in spatial resolution and depth resolution, and therefore the use of one or the other depends on the desired spatial scale. Neutron diffraction is often used for engineering applications in which the bulk scale strains and stresses are under investigation for changes in mechanical properties of components because it has the lowest spatial resolution of the diffractive techniques and is used to measure Type I stresses [60,89,108,112,113]. XRD and EBSD cross-correlation, however, can resolve type II and III strains, respectively, with the spatial resolution of XRD improving

toward the measurement of intragranular features [114,115]. The recent development of cross-correlation of electron backscatter diffraction (EBSD) data in crystalline material has resulted in the ability to calculate Type III elastic strains [109–111]. Transmission electron microscopy (TEM) can also characterize dislocation density and Type III strains, with improved spatial resolution when compared with SEM methods. Using precession electron diffraction (PED) in the TEM enables characterization of strain fields associated with single dislocations, however using this method we lose the statistical power that large sets of data from EBSD enable. PED is used in this thesis as a validation of the elastic strain results and to allow a more accurate dislocation density calculation.

Electron Backscatter Diffraction

In electron backscatter diffraction (EBSD), a highly polished sample is mounted in a scanning electron microscope (SEM) at approximately a 70° angle from horizontal. A highly sensitive phosphor screen inserted into the SEM near the sample is hit by the backscattered electrons, producing a pattern which depends upon the crystallography of the atomic planes in the sample (Figure 1-10). The resulting Kikuchi pattern contains orientation data which can be used to analyze the microstructure of the crystalline material, including GB character, phase, and level of plastic or elastic strain [116]. Spatial resolution of the EBSD technique depends on parameters including material, voltage, probe diameter and angle of incidence, however the limiting resolution of this technique with high probe current and small beam diameter can reach 10nm, and a resolution of 30nm can be achieved by reducing binning during data collection in most materials [117,118].

Plastic and elastic strains each affect the Kikuchi pattern in different ways; plastic strains, including dislocations, result in a change in orientation of the crystal lattice and therefore a change in the orientation of the Kikuchi pattern (Figure 1-11). Elastic strain may not alter the orientation of the crystal lattice, but they will change the length of the lattice parameter or the curvature of the crystal, thereby altering the thickness and/or the sharpness of the Kikuchi bands, or a shift in the bands relative to each other [109] (Figure 1-11b).

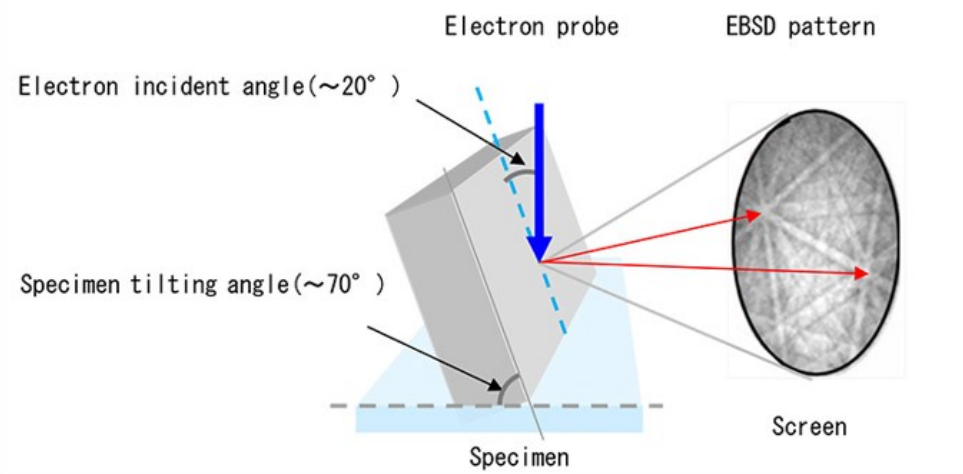

Figure 1-10. Schematic of EBSD data collection

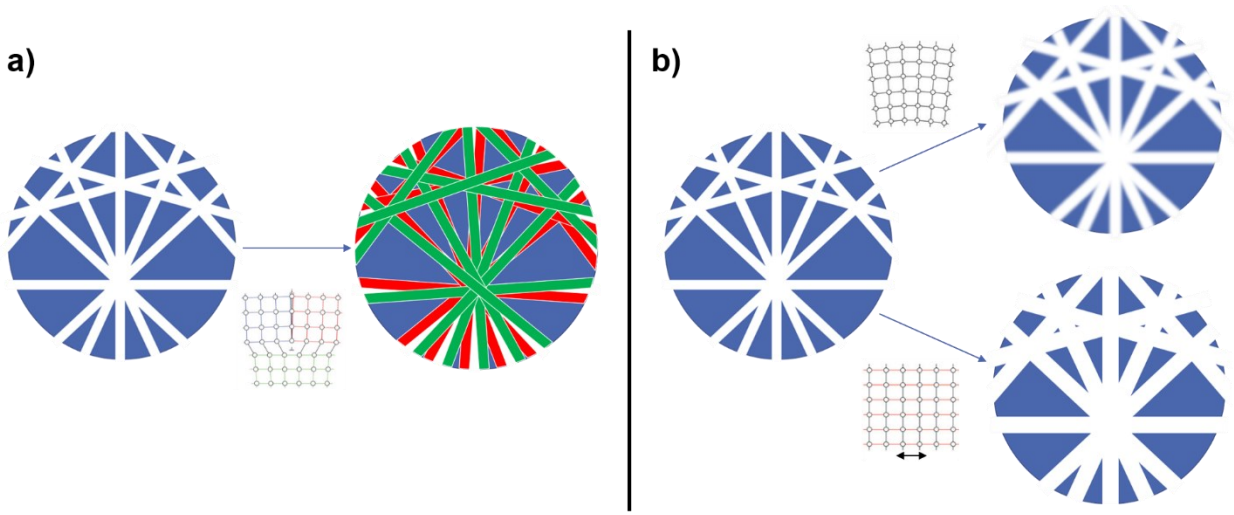

Figure 1-11. Change in Kikuchi bands resulting from plastic (a) and elastic (b) strains. Adapted from [116]

The precise measurement of these changes in Kikuchi pattern gives rise to the orientation and enables calculation of curvature and dislocation density characterization using the lower bound Nye tensor. Measurement of dislocation density in the SEM cannot account for statistically stored dislocations (SSDs) due to its relatively poor spatial resolution compared to a technique such as precession electron diffraction (PED) in the transmission electron microscope (TEM). Therefore, when dislocation density is calculated from EBSD results in this thesis, it is a measurement of only the geometrically necessary dislocation (GND) density [119]. In this thesis, GND density will be calculated from EBSD data for comparison with other microstructural features including elastic strain and, in Chapter 2 phase distribution after surface laser engraving. As demonstrated in Figure 1-11, measurement of dislocation density using the Nye tensor does not consider lattice curvature brought about by residual elastic strain due to the differences in Kikuchi pattern deformation resulting from these two mechanisms. However, cross-correlation calculation of the full deviatoric strain tensor has been developed based on comparing neighboring Kikuchi patterns to one another [110].

Kikuchi Pattern Cross-Correlation

The first elastic strain measurement using EBSD was described by Troost et al. in 1993 [109] on epitaxially grown $Si_{1-x}Ge_x$. In this measurement, a cross-correlation function was applied to a region of interest (ROI) in each Kikuchi pattern where the maximum of the resulting cross-correlation function was assumed to correspond to the shift in one Kikuchi pattern compared to the other (Figure 1-12). This measured lateral shift was converted into an angular shift and compared to known crystallographic angles between planes to result in the elastic strain. The formula for calculating elastic strain using cross-correlation of Kikuchi patterns has been further improved to use fast Fourier transforms (FFTs) of the ROIs in Kikuchi patterns for the cross-correlation function between a reference and a test pattern, which is computationally faster than direct calculation of the cross-correlation function [120]. First, the 2D FFT of each ROI is calculated, followed by cross-correlation of the two FFTs to result in a cross-correlation function where the location of the peak corresponds to the 2D shift in the test pattern compared to the reference pattern.

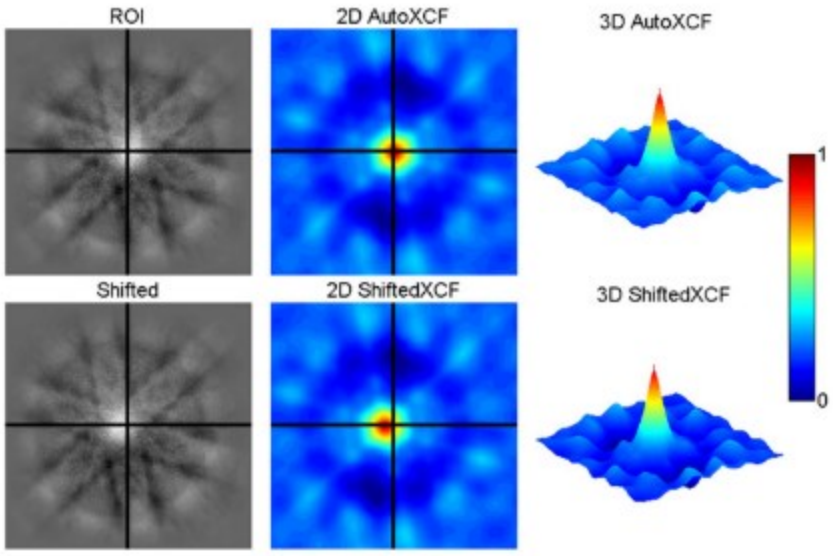

Figure 1-12. Two ROIs from a Kikuchi pattern, where the shifted ROI (bottom) is five pixels horizontally removed from the reference ROI (top), and the corresponding cross-correlation functions [118].

This shift is taken to be the shift at the point at the center of the ROI and the x and y components can be related to components of the displacement gradient tensor **a** where **u** = (u_1, u_2, u_3) is the displacement at position **x** = (x_1, x_2, x_3) in the sample.

$$\boldsymbol{a} = \begin{pmatrix} \frac{\partial u_1}{\partial x_1} & \frac{\partial u_1}{\partial x_2} & \frac{\partial u_1}{\partial x_3} \\ \frac{\partial u_2}{\partial x_1} & \frac{\partial u_2}{\partial x_2} & \frac{\partial u_2}{\partial x_3} \\ \frac{\partial u_3}{\partial x_1} & \frac{\partial u_3}{\partial x_2} & \frac{\partial u_3}{\partial x_3} \end{pmatrix} \tag{1}$$

Eq (1) can be split into symmetric and asymmetric parts representing strains (e_{ij}) and rotations (w_{ij}), respectively so that [110]

$$e_{ij} = \frac{1}{2}\left(\frac{\partial u_i}{\partial x_j} + \frac{\partial u_j}{\partial x_i}\right) \tag{2}$$

$$w_{ij} = \frac{1}{2}\left(\frac{\partial u_i}{\partial x_j} - \frac{\partial u_j}{\partial x_i}\right) \tag{3}$$

The 2D shifts in at least four ROIs are sufficient to calculate an exact solution for eight of the nine components in the deviatoric strain tensor, with the ninth component being measurable using matrix methods if more than four ROIs are used [110]. The ninth component is due to hydrostatic dilatation which alone does not produce a shift in features of the Kikuchi pattern and therefore cannot be directly measured using cross-correlation of FFTs. In addition to high spatial resolution, the angular resolution of the EBSD technique impacts the strain resolution of the cross-correlation analysis. Typical EBSD angular resolution (the lowest misorientation measured by general EBSD analysis) has been reported to be between .5-1°; however, by eschewing binning during data collection, this angular resolution can decrease to 0-1°, which results in a reported strain resolution of 10^{-4} [110,121].

This method has been tested on single crystal samples and on samples to which known strain was applied [122–124] as well as being expanded to use simulated reference patterns in place of real reference patterns [121]. A benefit to using simulated reference patterns is that absolute strain can be calculated, while in using real reference patterns the calculated strain is always a *relative* strain between reference and test pattern. Wilkinson and Britton reported in 2012 that increased misorientation between reference and test pattern resulted in error in the strain measurement; locations of ROIs are specified within the image frame, meaning that the ROI of a highly misoriented pattern may result in varied zone axis and band orientation to its reference pattern. The proposed solution to this was to perform an initial cross-correlation analysis between reference and test pattern to estimate the lattice rotation, using this result to remap the test pattern to make it more similar to the reference pattern, followed by another cross-correlation analysis to ensure the elastic strain measurement was not impact by the

misorientation between two points [125]. Although the remapping technique was shown to be able to recover elastic strain values up to an 11° misorientation between reference and test patterns, intragranular misorientation between points in AM materials can often reach 15° or greater. The HR-EBSD cross-correlation technique to measure elastic strains has therefore been little used in AM materials. Our solution to this problem is presented in detail in Chapter 2, where a maximum misorientation between points, or a misorientation tolerance, can be specified prior to cross-correlation analysis [126].

Transmission Electron Diffraction

TEM is an electron microscopy technique which enables higher spatial resolution than the SEM, enabling the analysis of elemental segregation on a scale that is useful in laser AM materials. In TEM, the electron transparent sample is held perpendicular to the electron beam and the resulting forward and backscattered electrons can be recorded as an image. The TEM has many capabilities, in this thesis it will be used to obtain high resolution images of dislocation cells in L-PBF IN625 as well as the elemental segregation present at the cell walls (Chapter 5). Energy dispersive X-ray spectroscopy (EDS) in the TEM enables high resolution on the order of nanometers, while the same technique in the SEM enables resolution on the order of tens of nanometers. Previous attempts at SEM-EDS of laser processed samples has demonstrated homogeneous elemental distribution, but this is because of the lack of spatial resolution when compared to TEM. Here, TEM-EDS is able to resolve elemental segregation and the presence of inclusions at the cell walls resulting from cellular solidification.

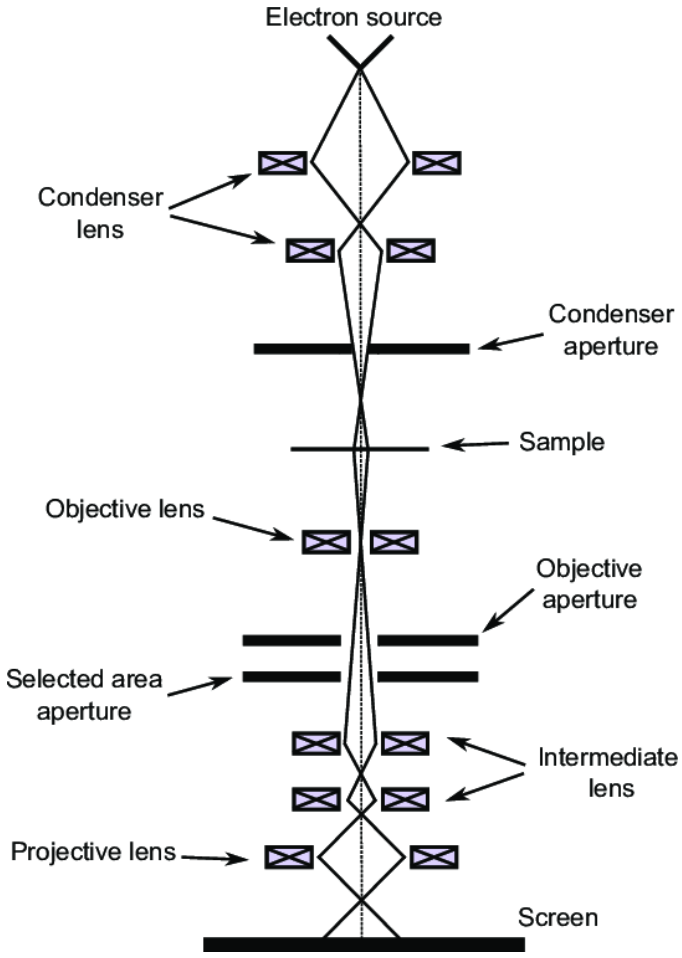

Figure 1-13. Schematic of TEM

Statistical Analysis

The ability to quantitatively analyze microstructural features is important for the improved simulation and prediction of AM properties. Using statistical methods to compare dislocation density and elastic strain between AM methods and within single builds will allow further understanding of the impact of thermal history on microstructural evolution. Additionally, the analysis of the spatial correlation between different microstructural features will enable quantifiable descriptors to be used in AM simulations and in predictions of microstructure in specific thermal environments. Currently, convolutional neural networks

(CNNs) and 2-point spatial correlations have been used to represent structure-property linkages in simulated microstructures. Xu et al. developed a novel PCA-based microstructural descriptor which directly enables primary reconstruction of microstructures without expensive computational cost [129], while Gupta et al. used data science methods to develop relationships between microstructural features and effective bulk material properties [130].

The spatial relationship between subgrain elastic strain and dislocation density in AM components is unknown, particularly the evolution of that relationship during processing. However, since recent reports suggest that subgrain elastic strain may be integral to the formation of dislocation cells, this relationship has become increasingly important to understand [34]. In this thesis an image analysis technique, MosaicIA [131], is used to determine the strength of spatial relationships between high levels of elastic strain and dislocation density. In the MosaicIA algorithm, two binary distributions are compared to each other, in this case high elastic strain and high dislocation density (figure 1-12). The strength of the spatial relationship between the two depends on the probability density function (PDF) which results from this analysis; when the probability of finding an increased elastic strain 'object' close to an increased dislocation density 'object' is relatively high, the spatial relationship between the two is increased. It will be shown in this thesis that the relationship between these two features increased with increased thermal gradient and higher temperature (Chapters 4 and 5). To determine a random relationship between the two features, a reference distribution *X* (dislocation density, in this case) is chosen and overlaid with an evenly spaced grid *x* and the distance between each *x* and the nearest *X* are measured [132]. The spatial distribution of different microstructural features is necessary for the quantification of

microstructural evolution throughout the AM process, and can also result in microstructural descriptors which can be tied to the bulk mechanical properties of a component or used to enable improved prediction of AM microstructures.

Simulation Methods

This thesis includes different modeling methods for the acquisition of thermal data and the observation of microstructure in simulation vs. experiment. The use of experimental and computational approaches in tandem can result in process maps which can be used to design and predict microstructures at the grain scale; for example, Gockel et al. used finite element analysis (FEA) with EBF3 of Ti-6Al-4V to arrive at process variable combinations which yielded constant beta phase grain size and morphology, finding that a constant melt pool cross-sectional area will yield a constant grain size [33]. However, sub-grain scale features, such as dislocation cells and elastic strain distributions, both of which are important to microstructural evolution and final mechanical properties, have not been investigated to this degree due to the difficulty in their characterization. Combinatorial approaches using microstructural characterization as well as microstructural simulation are important in the development of predictive methods in AM, including machine learning (ML). In ML, descriptive data of the microstructure can be used to 'teach' an algorithm the kinds of microstructural features to expect after specific fabrication or modification processes. Future ML frameworks may be able to predict the specific microstructure and the relationship between its features after a processing method or determine the processing parameters to use in order to obtain a desired structure and property set [9].

Computational simulation of additive techniques is a highly active field – the need for reliable prediction of properties and microstructures resulting from AM and laser processes drives the development and innovation of models from the bulk scale to the atomic level [10]. The multiscale nature of the physical processes at play during laser processing increase the complexity of simulating these techniques, already inherently difficult due to the myriad of processing parameters and influence of difficult to characterize microstresses. For example, in the design and engineering realm, the global scale is often of the most interest, so a bulk model may be desirable in order to track large scale thermal gradients and final mechanical and material properties of a components. These global models are popular in research due to their ease of use, lack of computational expense, and generally good predictions of bulk distortions in a component [133,134]. However, these simulations do not improve the knowledge or optimization of microstructure evolution during laser processes, because they rely on macro-scale constants and equations, while on the micro and meso scales random events such as fluid splatter take precedence. A comprehensive 'digital twin' of the AM process would include statistical techniques combined with multiphysics and multiscale modeling methods to mimic the physical process at different length and time scales to accurately predict structures and properties with minimum computational cost [10]. Before digital twins of the AM process can be fully relied upon to mimic and correct physical AM processes, microscale modeling techniques need descriptors and statistics from experimental methods. The definition of microstructural descriptors is an important part of the development of simulations and ML frameworks for AM techniques [135]. In Chapter 3, HR-EBSD is used to measure both elastic strain and GND density in IN625 from three difference AM techniques, in order to determine a

link between thermal environment and microstructural features. This chapter also includes the use of a statistical method using Fiji/ImageJ software to quantify the spatial relationship between microstructural feature. This statistical technique is also included in chapters 5 and 6 to determine the evolution of the spatial relationship in a single track IN625 sample and to define a microstructural descriptor in laser processed alloys for use in ML.

The modeling technique used here is a type of computational fluid dynamics (CFD) in which the temperature profiles and the melting of solid can be observed during laser processing. Using the thermal profiles determined from this simulation technique the evolution and kinetics of microstructure may be determined. For example, the comparison of microstructure at two different locations of a laser processed material is improved by the knowledge of the relative thermal gradients at those locations during laser processing; the evolution of strain concentrations and dislocation cell wall thickness may be linked to the thermal information. In Chapter 4, the thermal profiles of two varying laser processing parameters are used in tandem with the resultant microstructure to determine the level of martensite evolution during laser melting of low carbon steel. In Chapters 5 and 6, this same CFD model is used to link the thermal profiles and cooling rates during L-PBF and laser surface melting to the resulting strain concentrations and dislocation cell wall thickness in Inconel 625 and pure Ni. The fluid dynamics involved in AM melt pools is an area of intense study and is directly responsible for certain transformations during processing.

Discrete dislocation dynamics (DDD) modeling is a simulation technique that can help to gain insight into the mechanisms and kinetics behind microstructural properties and evolution. Recently, 3D-DD simulations were used to investigate the origins of the well-known Hall-Petch

effect, whereby material strength increases as grain size decreases [136]. Voisin et al. used DDD simulations to gain insight into cell formation and precipitate strengthening mechanisms, finding that without elemental segregation, dislocations remain randomly organized at lower density [49]. This result deviates from claims that elemental segregation is not necessary for dislocation arrangement into cell structures [99], demonstrating one of the open questions of surrounding the evolution of these structures. In this thesis, the temperature and stress state of a material system predicted by a finite element model (FEM) are used as inputs in the DDD model to determine dislocation density and the level of organizations in the L-PBF microstructure.

The development of materials simulations with the goal of property prediction and manufacturing optimization is an important area of research. Simulations on different length scales are necessary in order to include the physics at multiple levels; for example, crystal plasticity (CP) models, which simulate macroscale structures and properties, ideally would statistically account for all phenomena that occur in lower scale simulations such as quantum mechanical models [137]. This multiscale framework needs to be validated by experimental observations before the required upscaling can be reliably used for engineering predictions; experiments that are particularly scarce on the mesoscale [10,137].

Thesis Aims

This thesis is primarily motivated by the potential of laser AM to fabricate complex components quickly and efficiently. However, the drawbacks of these manufacturing methods are largely due to the thermal environment of the melt pool during laser processing. Therefore,

laser surface melting and engraving will also be used as model systems for AM techniques. The goal of this thesis is to describe the evolution of non-equilibrium features produced by rapid solidification (RS) inherent in laser processing which result in unreliable component behavior. The main gaps this thesis aims to answer are:

1. The use of lasers for direct part marking (DPM) is common in medicine and transportation, but there is not sufficient research to determine whether these markings effect the microstructure or mechanical properties of a component.
2. Residual stress is a known drawback of AM techniques, and type III strains are important for the material properties of a system. However, the microstructure of AM techniques results in high intragranular misorientation and leads to unreliable measurement of this feature using HR-EBSD cross-correlation.
3. AM techniques vary widely in raw material and in processing parameters, giving rise to microstructures that are unique to each individual method. The relative type III strains and dislocation densities, as well as other microstructural features including misorientation and cell structures, have not been explicitly tied to the relative thermal environments across different techniques. There is currently no statistical description of the relationship between microstructural features resulting from different thermal environments in AM.
4. The thermal environment during laser processing, including AM, varies based on location giving rise to anisotropic microstructures and strain distributions. The evolution of dislocation structures and elastic strain has not been linked to the temperature gradients and cooling rates within the laser melt pool.

Using surface laser engraving to mimic DPM, this thesis demonstrates the decrease in fatigue life caused by phase transformation during laser processing of industry relevant high carbon steel FC-0208. Additionally, different extents of laser engraving are used to determine that this phase transformation can be avoided with fewer laser passes, suggesting that DPM can be used with specific processing parameters that may not affect the material properties of a component. This experiment also suggests that surface laser engraving can be used for precision microstructural modification in cases where local control is necessary. Thermal modeling is used to define the temperature gradients and cooling rates resulting from different levels of laser engraving, suggesting that increased temperature and time above austenitizing temperature leads to phase transformations in this material.

HR-EBSD cross-correlation is a recently developed method of measuring type III strains, but is of little practical use in methods with high intragranular misorientation, such as those resulting from laser processing or AM. In this thesis, an open-source software, OpenXY [138], is used to demonstrate the extraneously high strains present during usual cross-correlation and a rotation tolerance is introduced to ensure that high levels of misorientation between the reference and test patterns do not cause miscalculations of strain. This technique is used throughout the thesis for calculation of type III elastic strains produced by laser processing in Nickel superalloy Inconel 625 (IN625).

Three unique methods of AM with widely varying thermal environments are used in this thesis to demonstrate the influence of thermal history on microstructure during AM. Using statistical analysis, it is observed that laser AM results in significantly higher levels of elastic strain and dislocation density. Additionally, spatial analysis of elastic strain and dislocation

density distributions is used to determine that these features are more closely related, spatially, in laser AM than in less thermally violent AM methods. The spatial relationship between these specific microstructural features is introduced as a possible descriptor for future simulations of microstructural evolution during processing.

In order to untangle the melt pool thermal environment from repetitive thermal cycles and heat affected zone (HAZ) influence, single tracks of L-PBF IN625 are analyzed at several locations along the build. A thermal simulation is used to determine differences at the end of the laser track compared to the center, while microstructural characterization demonstrates the changes in dislocation density and elastic strain due to local thermal environment. Discrete dislocation dynamics (DDD) modeling demonstrates that the temperature and stress levels at the end of the single track result in higher dislocation density and fewer discrete cell structure, supporting the experimental and thermal simulation results. Combined results from experiments and simulations suggest that the temperature gradient and cooling rates are directly related to the distribution of type III elastic strain and the level of dislocation density in cell walls.

Thesis Layout

Chapter 2 looks at possible phase transformations resulting from a laser engraving process. Structural FC-0208 steel is engraved using one laser pass and five laser passes to determine the extent of martensite formation present in this surface laser processing technique. A CFD model is implemented to obtain thermal data from the engraving process,

and it is found that using a higher number of laser passes results in increased formation of martensite.

Chapter 3 provides a detailed introduction to the characterization of microscale elastic strain using high-resolution electron backscatter diffraction (HR-EBSD) and cross-correlation of EBSD patterns, a method used throughout this work to track the evolution of elastic strain in varying thermal environments. Using Inconel 625 fabricated by laser-powder bed fusion (L-PBF), this chapter describes the implementation of a novel misorientation tolerance necessary for obtaining reasonable elastic strain values from metal parts containing high levels of intragranular misorientation, such as those produced using laser processing techniques. Observation of geometrically necessary dislocation (GND) dense intragranular low angle grain boundaries (LAGBs) and their possible relation to elastic strain concentrations are also discussed in this chapter.

In Chapter 4, the elastic strain calculation described in the introduction and in Chapter 3 is implemented in Inconel 625 parts fabricated by three AM technique with widely varying thermal environments: binder jet 3D printing (BJ3DP), electron beam freeform fabrication (EBF3), and L-PBF. A novel spatial analysis method is performed on the resulting elastic strain and GND density maps to determine statistical differences in the correlation of these microstructural features resulting from differences in thermal environments during processing. It is shown that more complex, violent thermal histories such as those in L-PBF result in a significantly closer spatial relationship between elastic strain and GND density than that seen in what may be termed as ‘gentle’ AM techniques like BJ3DP.

Chapter 5 is concerned with the local thermal environments occurring in L-PBF and demonstrates the evolution of dislocation structures and elastic strain in a 1D track of Inconel 625 built by L-PBF. A computational fluid dynamics (CFD) simulation is used to quantify the thermal gradients and cooling rates present at different location along the single track in order to correlate these variables to the microstructural evolution. A DDD simulation is used to simulate cells walls resulting from the processing parameters of the L-PBF track, corroborating the effect of thermal environment on dislocation density.

To conclude this thesis, Chapter 6 discusses the impact of results presented in this thesis and future work in the field of melt pool thermal analysis, specifically the effect of solute microsegregation on the evolution of cell walls. The cells in AM are typical of those found elsewhere in metallurgy, usually including both microsegregation and dislocation dense walls, however it is an open question in the AM community whether these cells are formed first by solute segregation or by dislocations. Preliminary microstructural comparisons between Inconel 625 and pure Nickel produced via L-PBF suggest that solute is necessary for the formation of dislocation cells. Applications of the methodologies described in Chapters 3 and 4 and the future of data driven predictive technologies in AM are discussed and the contributions of the results in this thesis are summarized.

References

[1] T. Wohlers, T. Gornet, History of Additive Manufacturing, 2014.

[2] T. McCue, Additive Manufacturing Industry Grows To Almost $12 Billion In 2019, Forbes. (2020). https://www.forbes.com/sites/tjmccue/2020/05/08/additive-manufacturing-industry-grows-to-almost-12-billion-in-2019/#e9151d85678d.

[3] A. Hehr, M. Norfolk, A comprehensive review of ultrasonic additive manufacturing, Rapid Prototyp. J. 26 (2019) 445–458. https://doi.org/10.1108/RPJ-03-2019-0056.

[4] T. Debroy, H.L. Wei, J.S. Zuback, T. Mukherjee, J.W. Elmer, J.O. Milewski, A.M. Beese, A. Wilson-Heid, A. De, W. Zhang, Additive manufacturing of metallic components-Process, structure and properties, (2017). https://doi.org/10.1016/j.pmatsci.2017.10.001.

[5] Y.-L. Hao, S.-J. Li, R. Yang, Biomedical titanium alloys and their additive manufacturing, Rare Met. 35 (2016) 661–671. https://doi.org/10.1007/s12598-016-0793-5.

[6] D. Manfredi, F. Calignano, M. Krishnan, R. Canali, E.P. Ambrosio, S. Biamino, D. Ugues, M. Pavese, P. Fino, Additive Manufacturing of Al Alloys and Aluminium Matrix Composites (AMCs), (n.d.) 3–34. https://doi.org/10.5772/58534.

[7] R. Jiang, A. Mostafaei, Z. Wu, A. Choi, P.-W. Guan, M. Chmielus, A.D. Rollett, Effect of heat treatment on microstructural evolution and hardness homogeneity in laser powder bed fusion of alloy 718, Addit. Manuf. 35 (2020) 101282. https://doi.org/10.1016/j.addma.2020.101282.

[8] C. Herriott, X. Li, N. Kouraytem, V. Tari, W. Tan, B. Anglin, A.D. Rollett, A.D. Spear, A multi-scale, multi-physics modeling framework to predict spatial variation of properties in additive-manufactured metals, Model. Simul. Mater. Sci. Eng. 27 (2019) 025009. https://doi.org/10.1088/1361-651X/aaf753.

[9] S. Di Cataldo, S. Vinco, G. Urgese, F. Calignano, E. Ficarra, A. Macii, E. Macii, Optimizing Quality Inspection and Control in Powder Bed Metal Additive Manufacturing: Challenges and Research Directions, Proc. IEEE. (2021) 1–21. https://doi.org/10.1109/JPROC.2021.3054628.

[10] T.W. Heo, S.A. Khairallah, R. Shi, J. Berry, A. Perron, N.P. Calta, A.A. Martin, N.R. Barton, J.D. Roehling, T. Roehling, J.-L. Fattebert, A. Anderson, A.L. Nichols, S. Wopschall, W.E. King, J.T. McKeown, M. Matthews, A mesoscopic digital twin that bridges length and time scales for control of additively manufactured metal microstructures, J. Phys. Mater. (2021) 11–14. https://doi.org/10.1088/2515-7639/abeef8.

[11] R. Liu, Z. Wang, T. Sparks, F. Liou, J. Newkirk, Aerospace applications of laser additive manufacturing, in: Laser Addit. Manuf. Mater. Des. Technol. Appl., Elsevier Inc., 2017: pp. 351–371. https://doi.org/10.1016/B978-0-08-100433-3.00013-0.

[12] S. Anandan, R.M. Hussein, M. Spratt, J. Newkirk, K. Chandrashekhara, H. Misak, M. Walker, Failure In metal honeycombs manufactured by selective laser melting of 304 L stainless steel under compression, Virtual Phys. Prototyp. 14 (2019) 114–122. https://doi.org/10.1080/17452759.2018.1531336.

[13] S. Singh, S. Ramakrishna, Biomedical applications of additive manufacturing: Present and future, Curr. Opin. Biomed. Eng. 2 (2017) 105–115. https://doi.org/10.1016/j.cobme.2017.05.006.

[14] N. Eschner, L. Weiser, B. Häfner, G. Lanza, Development of an Acoustic Process Monitoring System for the Selective Laser Melting (SLM), in: Solid Free Fabr Symp Proc, 2018: pp. 2097–3017.

[15] F. Liu, X. Lin, C. Huang, M. Song, G. Yang, J. Chen, W. Huang, The effect of laser scanning path on microstructures and mechanical properties of laser solid formed nickel-base superalloy Inconel 718, J. Alloys Compd. 509 (2011) 4505–4509. https://doi.org/10.1016/j.jallcom.2010.11.176.

[16] Z. Wang, T.A. Palmer, A.M. Beese, Effect of processing parameters on microstructure and tensile properties of austenitic stainless steel 304L made by directed energy deposition additive manufacturing, Acta Mater. 110 (2016) 226–235. https://doi.org/10.1016/j.actamat.2016.03.019.

[17] K.N. Amato, J. Hernandez, L.E. Murr, E. Martinez, S.M. Gaytan, P.W. Shindo, S. Collins, Comparison of Microstructures and Properties for a Ni-Base Superalloy (Alloy 625) Fabricated by Electron and Laser Beam Melting, J. Mater. Sci. Res. 1 (2012). https://doi.org/10.5539/jmsr.v1n2p3.

[18] H. Pohl, A. Simchi, M. Issa, H.C. Dias, Thermal stresses in direct metal laser sintering, Proc. SFF Symp. (2001) 366–372. http://edge.rit.edu/edge/P10551/public/SFF/SFF 2001 Proceedings/2001 SFF Papers/41-Pohl.pdf.

[19] R. Shi, S.A. Khairallah, T.T. Roehling, T.W. Heo, J.T. McKeown, M.J. Matthews, Microstructural control in metal laser powder bed fusion additive manufacturing using laser beam shaping strategy, Acta Mater. 184 (2020) 284–305. https://doi.org/10.1016/j.actamat.2019.11.053.

[20] A.K. Agrawal, G. Meric de Bellefon, D. Thoma, High-throughput experimentation for microstructural design in additively manufactured 316L stainless steel, Mater. Sci. Eng. A. 793 (2020). https://doi.org/10.1016/j.msea.2020.139841.

[21] L.M. Sochalski-Kolbus, E.A. Payzant, P.A. Cornwell, T.R. Watkins, S.S. Babu, R.R. Dehoff, M. Lorenz, O. Ovchinnikova, C. Duty, Comparison of Residual Stresses in Inconel 718 Simple Parts Made by Electron Beam Melting and Direct Laser Metal Sintering, Metall. Mater. Trans. A Phys. Metall. Mater. Sci. 46 (2015) 1419–1432. https://doi.org/10.1007/s11661-014-2722-2.

[22] A.E. Patterson, S.L. Messimer, P.A. Farrington, Overhanging Features and the SLM/DMLS Residual Stresses Problem: Review and Future Research Need, Technologies. 5 (2017) 15. https://doi.org/10.3390/technologies5020015.

[23] Y. Tian, D. McAllister, H. Colijn, M. Mills, D. Farson, M. Nordin, S. Babu, Rationalization of microstructure heterogeneity in INCONEL 718 builds made by the direct laser additive manufacturing process, Metall. Mater. Trans. A Phys. Metall. Mater. Sci. 45A (2014) 4470–4483. https://doi.org/10.1007/s11661-014-2370-6.

[24] P. Nandwana, A.M. Elliott, D. Siddel, A. Merriman, W.H. Peter, S.S. Babu, Powder bed binder jet 3D printing of Inconel 718 : Densification , microstructural evolution and challenges q, Curr. Opin. Solid State Mater. Sci. (2017) 1–12. https://doi.org/10.1016/j.cossms.2016.12.002.

[25] K. Kimes, K. Myers, A. Klein, M. Ahlfors, E. Stevens, M. Chmielus, Binder Jet 3D Printing of 316L Stainless Steel: Effects of HIP on Fatigue, Microsc. Microanal. 25 (2019) 2600–2601. https://doi.org/10.1017/s1431927619013734.

[26] A. Mostafaei, E.L. Stevens, E.T. Hughes, S.D. Biery, C. Hilla, M. Chmielus, Powder bed binder jet printed alloy 625: Densification, microstructure and mechanical properties, Mater. Des. 108 (2016) 126–135. https://doi.org/10.1016/j.matdes.2016.06.067.

[27] L.E. Murr, Metallurgy of additive manufacturing: Examples from electron beam melting, Addit. Manuf. 5 (2015) 40–53. https://doi.org/10.1016/j.addma.2014.12.002.

[28] H. Galarraga, D.A. Lados, R.R. Dehoff, M.M. Kirka, P. Nandwana, Effects of the microstructure and porosity on properties of Ti-6Al-4V ELI alloy fabricated by electron beam melting (EBM), Addit. Manuf. 10 (2016) 47–57. https://doi.org/10.1016/j.addma.2016.02.003.

[29] A.R. Balachandramurthi, J. Olsson, J. Ålgårdh, A. Snis, J. Moverare, R. Pederson, Microstructure tailoring in Electron Beam Powder Bed Fusion additive manufacturing and its potential consequences, Results Mater. 1 (2019) 100017. https://doi.org/10.1016/j.rinma.2019.100017.

[30] S.C. Joshi, A.A. Sheikh, 3D printing in aerospace and its long-term sustainability, Virtual Phys. Prototyp. 10 (2015) 111–175. https://doi.org/10.1080/17452759.2015.1111519.

[31] X. Shu, G. Chen, J. Liu, B. Zhang, J. Feng, Microstructure evolution of copper/steel gradient deposition prepared using electron beam freeform fabrication, Mater. Lett. 213 (2018) 374–377. https://doi.org/10.1016/j.matlet.2017.11.016.

[32] K.M. Taminger, R.A. Hafley, Electron beam freeform fabrication for cost effective near-net shape manufacturing, Nato Avt. 139 (2006).

[33] J. Gockel, J. Beuth, K. Taminger, Integrated control of solidification microstructure and melt pool dimensions in electron beam wire feed additive manufacturing of Ti-6Al-4V, Addit. Manuf. (2014) 119–126. https://doi.org/10.1016/j.addma.2014.09.004.

[34] K.M. Bertsch, G. Meric de Bellefon, B. Kuehl, D.J. Thoma, Origin of dislocation structures in an additively manufactured austenitic stainless steel 316L, Acta Mater. 199 (2020) 19–33. https://doi.org/10.1016/j.actamat.2020.07.063.

[35] Y. Hu, X. Lin, Y. Li, Y. Ou, X. Gao, Q. Zhang, W. Li, W. Huang, Microstructural evolution and anisotropic mechanical properties of Inconel 625 superalloy fabricated by directed energy deposition, J. Alloys Compd. 870 (2021) 159426. https://doi.org/10.1016/j.jallcom.2021.159426.

[36] X. Lu, M. Chiumenti, M. Cervera, J. Li, X. Lin, L. Ma, G. Zhang, E. Liang, Substrate design to minimize residual stresses in Directed Energy Deposition AM processes, Mater. Des. 202 (2021) 109525. https://doi.org/10.1016/j.matdes.2021.109525.

[37] A. Mostafaei, P. Rodriguez De Vecchis, I. Nettleship, M. Chmielus, Effect of powder size distribution on densification and microstructural evolution of binder-jet 3D-printed alloy 625, Mater. Des. 162 (2019) 375–383. https://doi.org/10.1016/j.matdes.2018.11.051.

[38] A. Lal, R.G. Iacocca, R.M. German, Microstructural evolution during the supersolidus liquid phase sintering of nickel-based prealloyed powder mixtures, J. Mater. Sci. 35 (2000) 4507–4518.

[39] R.M. German, Supersolidus liquid-phase sintering of prealloyed powders, Metall. Mater. Trans. A Phys. Metall. Mater. Sci. 28 (1997) 1553–1567. https://doi.org/10.1007/s11661-997-0217-0.

[40] A. Mostafaei, J. Toman, E.L. Stevens, E.T. Hughes, Y.L. Krimer, M. Chmielus, Microstructural evolution and mechanical properties of differently heat-treated binder jet printed samples from gas- and water-atomized alloy 625 powders, Acta Mater. 124 (2017) 280–289. https://doi.org/10.1016/j.actamat.2016.11.021.

[41] K. Taminger, R. Hafley, Electron beam freeform fabrication: a rapid metal deposition process, Proc. 3rd Annu. Automot. Compos. Conf. (2003) 9–10. http://www.ntrs.nasa.gov/archive/nasa/casi.ntrs.nasa.gov/20040042496_2004036110.pdf.

[42] R. Hafley, K.M.B. Taminger, R. Bird, Electron Beam Freeform Fabrication in the Space Environment, AIAA Pap. (2007) 1–9. https://doi.org/10.2514/6.2007-1154.

[43] J. Xu, J. Zhu, J. Fan, Q. Zhou, Y. Peng, S. Guo, Microstructure and mechanical properties of Ti–6Al–4V alloy fabricated using electron beam freeform fabrication, Vacuum. 167 (2019) 364–373. https://doi.org/10.1016/j.vacuum.2019.06.030.

[44] B.E. Carroll, T.A. Palmer, A.M. Beese, Anisotropic tensile behavior of Ti–6Al–4V components

fabricated with directed energy deposition additive manufacturing, Acta Mater. 87 (2015) 309–320. https://doi.org/10.1016/j.actamat.2014.12.054.

[45] Z. Chen, S. Chen, Z. Wei, L. Zhang, P. Wei, B. Lu, S. Zhang, Y. Xiang, Anisotropy of nickel-based superalloy K418 fabricated by selective laser melting, Prog. Nat. Sci. Mater. Int. 28 (2018) 496–504. https://doi.org/10.1016/j.pnsc.2018.07.001.

[46] V.A. Popovich, E. Borisov, A. Popovich, Vs. Sufiiarov, D. Masaylo, L. Alzina, Functionally graded Inconel 718 processed by additive manufacturing: Crystallographic texture, anisotropy of microstructure and mechanical properties, Mater. Des. 114 (2017) 441–449. https://doi.org/10.1016/j.matdes.2016.10.075.

[47] K. Kunze, T. Etter, J. Grässlin, V. Shklover, Texture, anisotropy in microstructure and mechanical properties of IN738LC alloy processed by selective laser melting (SLM), Mater. Sci. Eng. A. 620 (2015) 213–222. https://doi.org/10.1016/j.msea.2014.10.003.

[48] G. Nicoletto, R. Konečná, M. Frkáň, E. Riva, Surface roughness and directional fatigue behavior of as-built EBM and DMLS Ti6Al4V, Int. J. Fatigue. 116 (2018) 140–148. https://doi.org/10.1016/j.ijfatigue.2018.06.011.

[49] T. Voisin, J.-B. Forien, A. Perron, S. Aubry, N. Bertin, A. Samanta, A. Baker, Y.M. Wang, New insights on cellular structures strengthening mechanisms and thermal stability of an austenitic stainless steel fabricated by laser powder-bed-fusion, Acta Mater. 203 (2021) 116476. https://doi.org/10.1016/j.actamat.2020.11.018.

[50] V. Gunenthiram, P. Peyre, M. Schneider, M. Dal, F. Coste, R. Fabbro, Analysis of laser–melt pool–powder bed interaction during the selective laser melting of a stainless steel, J. Laser Appl. 29 (2017) 022303. https://doi.org/10.2351/1.4983259.

[51] W. Chen, T. Voisin, Y. Zhang, J.-B. Florien, C.M. Spadaccini, D.L. McDowell, T. Zhu, Y.M. Wang, Microscale residual stresses in additively manufactured stainless steel, Nat. Commun. 10 (2019) 4338. https://doi.org/10.1038/s41467-019-12265-8.

[52] A.M. Beese, B.E. Carroll, Review of Mechanical Properties of Ti-6Al-4V Made by Laser-Based Additive Manufacturing Using Powder Feedstock, JOM. 68 (2016) 724–734. https://doi.org/10.1007/s11837-015-1759-z.

[53] P. Edwards, M. Ramulu, Fatigue performance evaluation of selective laser melted Ti–6Al–4V, Mater. Sci. Eng. A. 598 (2014) 327–337. https://doi.org/10.1016/j.msea.2014.01.041.

[54] N.C. Levkulich, S.L. Semiatin, J.E. Gockel, J.R. Middendorf, A.T. DeWald, N.W. Klingbeil, The effect of process parameters on residual stress evolution and distortion in the laser powder bed fusion of Ti-6Al-4V, Addit. Manuf. 28 (2019) 475–484. https://doi.org/10.1016/j.addma.2019.05.015.

[55] L.E. Criales, T. Özel, Temperature profile and melt depth in laser powder bed fusion of Ti-6Al-4V titanium alloy, Prog. Addit. Manuf. 2 (2017) 169–177. https://doi.org/10.1007/s40964-017-0029-8.

[56] M.J. Benoit, M. Mazur, M.A. Easton, M. Brandt, Effect of alloy composition and laser powder bed fusion parameters on the defect formation and mechanical properties of Inconel 625, Int. J. Adv. Manuf. Technol. 114 (2021) 915–927. https://doi.org/10.1007/s00170-021-06957-z.

[57] F. Zhang, L.E. Levine, A.J. Allen, M.R. Stoudt, G. Lindwall, E.A. Lass, M.E. Williams, Y. Idell, C.E.

Campbell, Effect of heat treatment on the microstructural evolution of a nickel-based superalloy additive-manufactured by laser powder bed fusion, Acta Mater. 152 (2018) 200–214. https://doi.org/10.1016/j.actamat.2018.03.017.

[58] F. Zhang, L.E. Levine, A.J. Allen, C.E. Campbell, E.A. Lass, S. Cheruvathur, M.R. Stoudt, M.E. Williams, Y. Idell, Homogenization kinetics of a nickel-based superalloy produced by powder bed fusion laser sintering, Scr. Mater. 131 (2017) 98–102. https://doi.org/10.1016/j.scriptamat.2016.12.037.

[59] S.K. Nayak, S.K. Mishra, A.N. Jinoop, C.P. Paul, K.S. Bindra, Experimental Studies on Laser Additive Manufacturing of Inconel-625 Structures Using Powder Bed Fusion at 100 µm Layer Thickness, J. Mater. Eng. Perform. 29 (2020) 7636–7647. https://doi.org/10.1007/s11665-020-05215-9.

[60] H.G. Li, T.L. Lee, W. Zheng, Y.Z. Lu, H.B.C. Yin, J.X. Yang, Y.J. Huang, J.F. Sun, Characterization of residual stress in laser melting deposited CoCrFeMnNi high entropy alloy by neutron diffraction, Mater. Lett. 263 (2020) 127247. https://doi.org/10.1016/j.matlet.2019.127247.

[61] H. Wang, Z.G. Zhu, H. Chen, A.G. Wang, J.Q. Liu, H.W. Liu, R.K. Zheng, S.M.L. Nai, S. Primig, S.S. Babu, S.P. Ringer, X.Z. Liao, Effect of cyclic rapid thermal loadings on the microstructural evolution of a CrMnFeCoNi high-entropy alloy manufactured by selective laser melting, Acta Mater. 196 (2020) 609–625. https://doi.org/10.1016/j.actamat.2020.07.006.

[62] A. Ladewig, G. Schlick, M. Fisser, V. Schulze, U. Glatzel, Influence of the shielding gas flow on the removal of process by-products in the selective laser melting process, Addit. Manuf. 10 (2016) 1–9. https://doi.org/10.1016/j.addma.2016.01.004.

[63] E.J. Lavernia, T.S. Srivatsan, The rapid solidification processing of materials: science, principles, technology, advances, and applications, J. Mater. Sci. 45 (2010) 287–325. https://doi.org/10.1007/s10853-009-3995-5.

[64] D. Gu, L. Du, D. Dai, K. Lin, M. Xia, S. Li, J. He, Influence of thermal behavior along deposition direction on microstructure and microhardness of laser melting deposited metallic parts, Appl. Phys. A. 125 (2019) 455. https://doi.org/10.1007/s00339-019-2745-z.

[65] P.K. Gokuldoss, S. Kolla, J. Eckert, Additive Manufacturing Processes: Selective Laser Melting, Electron Beam Melting and Binder Jetting-Selection Guidelines, Materials (Basel). 10 (2017). https://doi.org/10.3390/ma10060672.

[66] P.A. Hooper, Melt pool temperature and cooling rates in laser powder bed fusion, Addit. Manuf. 22 (2018) 548–559. https://doi.org/10.1016/j.addma.2018.05.032.

[67] P. Mercelis, J.-P. Kruth, Residual stresses in selective laser sintering and selective laser melting, Rapid Prototyp. J. 12 (2006) 254–265. https://doi.org/10.1108/13552540610707013.

[68] R.J. Moat, A.J. Pinkerton, L. Li, P.J. Withers, M. Preuss, Residual stresses in laser direct metal deposited Waspaloy, Mater. Sci. Eng. A. (2011). https://doi.org/10.1016/j.msea.2010.12.010.

[69] Y.S.J. Yoo, T.A. Book, M.D. Sangid, J. Kacher, Identifying strain localization and dislocation processes in fatigued Inconel 718 manufactured from selective laser melting, Mater. Sci. Eng. A. 724 (2018) 444–451. https://doi.org/10.1016/j.msea.2018.03.127.

[70] K.G. Prashanth, J. Eckert, Formation of metastable cellular microstructures in selective laser melted alloys, J. Alloys Compd. 707 (2017) 27–34. https://doi.org/10.1016/j.jallcom.2016.12.209.

[71] A.J. Birnbaum, J.C. Steuben, E.J. Barrick, A.P. Iliopoulos, J.G. Michopoulos, Intrinsic strain aging, Σ3 boundaries, and origins of cellular substructure in additively manufactured 316L, Addit. Manuf. 29 (2019). https://doi.org/10.1016/j.addma.2019.100784.

[72] T. Vilaro, C. Colin, J.D. Bartout, L. Nazé, M. Sennour, Microstructural and mechanical approaches of the selective laser melting process applied to a nickel-base superalloy, Mater. Sci. Eng. A. 534 (2012) 446–451. https://doi.org/10.1016/j.msea.2011.11.092.

[73] K. Saeidi, X. Gao, Y. Zhong, Z.J. Shen, Hardened austenite steel with columnar sub-grain structure formed by laser melting, Mater. Sci. Eng. A. 625 (2015) 221–229. https://doi.org/10.1016/j.msea.2014.12.018.

[74] M.H. Farshidianfar, A. Khajepour, A.P. Gerlich, Effect of real-time cooling rate on microstructure in Laser Additive Manufacturing, J. Mater. Process. Technol. 231 (2016) 468–478. https://doi.org/10.1016/j.jmatprotec.2016.01.017.

[75] J.C. Ion, H.R. Shercliff, M.F. Ashby, Diagrams for laser materials processing, Acta Metall. Mater. 40 (1992) 1539–1551. https://doi.org/10.1016/0956-7151(92)90097-X.

[76] C. Ma, G. Peng, L. Nie, H. Liu, Y. Guan, Laser surface modification of Mg-Gd-Ca alloy for corrosion resistance and biocompatibility enhancement, Appl. Surf. Sci. 445 (2018) 211–216. https://doi.org/10.1016/j.apsusc.2018.03.174.

[77] A. Hemmasian Ettefagh, H. Wen, A. Chaichi, M.I. Islam, F. Lu, M. Gartia, S. Guo, Laser surface modifications of Fe-14Cr ferritic alloy for improved corrosion performance, Surf. Coatings Technol. 381 (2020) 125194. https://doi.org/10.1016/j.surfcoat.2019.125194.

[78] T.M. Yue, J.K. Yu, Z. Mei, H.C. Man, Excimer laser surface treatment of Ti-6Al-4V alloy for corrosion resistance enhancement, Mater. Lett. 52 (2002) 206–212. https://doi.org/10.1016/S0167-577X(01)00395-0.

[79] Z. Qin, D.-H. Xia, Y. Zhang, Z. Wu, L. Liu, Y. Lv, Y. Liu, W. Hu, Microstructure modification and improving corrosion resistance of laser surface quenched nickel–aluminum bronze alloy, Corros. Sci. 174 (2020) 108744. https://doi.org/10.1016/j.corsci.2020.108744.

[80] M. Kumagai, M.E. Curd, H. Soyama, T. Ungár, G. Ribárik, P.J. Withers, Depth-profiling of residual stress and microstructure for austenitic stainless steel surface treated by cavitation, shot and laser peening, Mater. Sci. Eng. A. 813 (2021) 141037. https://doi.org/10.1016/j.msea.2021.141037.

[81] E.R. Gordon, A. Shokrani, J.M. Flynn, S. Goguelin, J. Barclay, V. Dhokia, A surface modification decision tree to influence design in additive manufacturing, in: Smart Innov. Syst. Technol., Springer Science and Business Media Deutschland GmbH, 2016: pp. 423–434. https://doi.org/10.1007/978-3-319-32098-4_36.

[82] L. Chen, B. Richter, X. Zhang, K.B. Bertsch, D.J. Thoma, F.E. Pfefferkorn, Effect of laser polishing on the microstructure and mechanical properties of stainless steel 316L fabricated by laser powder bed fusion, Mater. Sci. Eng. A. 802 (2021). https://doi.org/10.1016/j.msea.2020.140579.

[83] T. DebRoy, H.L. Wei, J.S. Zuback, T. Mukherjee, J.W. Elmer, J.O. Milewski, A.M. Beese, A. Wilson-Heid, A. De, W. Zhang, Additive manufacturing of metallic components – Process, structure and properties, Prog. Mater. Sci. 92 (2018) 112–224. https://doi.org/10.1016/j.pmatsci.2017.10.001.

[84] S. Afkhami, M. Dabiri, S.H. Alavi, T. Björk, A. Salminen, Fatigue characteristics of steels manufactured by selective laser melting, Int. J. Fatigue. 122 (2019) 72–83. https://doi.org/10.1016/j.ijfatigue.2018.12.029.

[85] W.E. King, A.T. Anderson, R.M. Ferencz, N.E. Hodge, C. Kamath, S.A. Khairallah, A.M. Rubenchik, Laser powder bed fusion additive manufacturing of metals; physics, computational, and materials challenges, Appl. Phys. Rev. 2 (2015). https://doi.org/10.1063/1.4937809.

[86] V. Thampy, A.Y. Fong, N.P. Calta, J. Wang, A.A. Martin, P.J. Depond, A.M. Kiss, G. Guss, Q. Xing, R.T. Ott, A. van Buuren, M.F. Toney, J.N. Weker, M.J. Kramer, M.J. Matthews, C.J. Tassone, K.H. Stone, Subsurface Cooling Rates and Microstructural Response during Laser Based Metal Additive Manufacturing, Sci. Rep. 10 (2020) 1981. https://doi.org/10.1038/s41598-020-58598-z.

[87] I. Serrano-Munoz, T. Fritsch, T. Mishurova, A. Trofimov, D. Apel, A. Ulbricht, A. Kromm, R. Hesse, A. Evans, G. Bruno, On the interplay of microstructure and residual stress in LPBF IN718, J. Mater. Sci. (2020). https://doi.org/10.1007/s10853-020-05553-y.

[88] C. Li, Z.Y. Liu, X.Y. Fang, Y.B. Guo, Residual Stress in Metal Additive Manufacturing, Procedia CIRP. 71 (2018) 348–353. https://doi.org/10.1016/j.procir.2018.05.039.

[89] M.T. Hutchings, Withers.P.J, T.M. Holden, T. Lorentzen, Introduction to characterization of residual stress by neutron diffraction, CRC press, Boca Raton, FL, 2005. https://doi.org/10.1016/S1369-7021(05)00849-7.

[90] P.J. Withers, H.K.D.H. Bhadeshia, Residual stress. Part 1 – Measurement techniques, Mater. Sci. Technol. 17 (2001) 355–365. https://doi.org/10.1179/026708301101509980.

[91] E. Macherauch, Introduction to Residual Stress, in: A. Niku-Lari (Ed.), Adv. Surf. Treat. Vol. 4, Pergamon Press, New York, 1987: pp. 1–36.

[92] L. Pintschovius, Macrostresses, Microstresses and Stress Tensors, in: Meas. Residual Appl. Stress Using Neutron Diffr., Springer Netherlands, 1992: pp. 115–130. https://doi.org/10.1007/978-94-011-2797-4_7.

[93] L. Parry, I.A. Ashcroft, R.D. Wildman, Understanding the effect of laser scan strategy on residual stress in selective laser melting through thermo-mechanical simulation, Addit. Manuf. 12 (2016) 1–15. https://doi.org/10.1016/j.addma.2016.05.014.

[94] M.F. Zaeh, G. Branner, Investigations on residual stresses and deformations in selective laser melting, Prod. Eng. 4 (2010) 35–45. https://doi.org/10.1007/s11740-009-0192-y.

[95] I. van Zyl, I. Yadroitsava, I. Yadroitsev, RESIDUAL STRESS IN TI6AL4V OBJECTS PRODUCED BY DIRECT METAL LASER SINTERING, South African J. Ind. Eng. 27 (2016) 134–141. https://doi.org/10.7166/27-4-1468.

[96] A. Salmi, E. Atzeni, L. Iuliano, M. Galati, Experimental Analysis of Residual Stresses on AlSi10Mg Parts Produced by Means of Selective Laser Melting (SLM), Procedia CIRP. 62 (2017) 458–463. https://doi.org/10.1016/j.procir.2016.06.030.

[97] B. Vrancken, R.K. Ganeriwala, M.J. Matthews, Analysis of laser-induced microcracking in tungsten under additive manufacturing conditions: Experiment and simulation, Acta Mater. 194 (2020) 464–472. https://doi.org/10.1016/j.actamat.2020.04.060.

[98] A. Dutta, T.M. Park, J.-H. Nam, S.-I. Lee, B. Hwang, W.S. Choi, S. Sandlöbes, D. Ponge, J. Han, Enhancement of the tensile properties and impact toughness of a medium-Mn steel through the homogeneous microstrain distribution, Mater. Charact. 174 (2021) 110992. https://doi.org/10.1016/j.matchar.2021.110992.

[99] T. Pinomaa, M. Lindroos, M. Walbrühl, N. Provatas, A. Laukkanen, The significance of spatial length scales and solute segregation in strengthening rapid solidification microstructures of 316L stainless steel, Acta Mater. 184 (2020) 1–16. https://doi.org/10.1016/j.actamat.2019.10.044.

[100] T. De Terris, O. Castelnau, Z. Hadjem-Hamouche, H. Haddadi, V. Michel, P. Peyre, Analysis of As-Built Microstructures and Recrystallization Phenomena on Inconel 625 Alloy Obtained via Laser Powder Bed Fusion (L-PBF), Metals (Basel). 11 (2021) 619. https://doi.org/10.3390/met11040619.

[101] L.E. Murr, E. Martinez, K.N. Amato, S.M. Gaytan, J. Hernandez, D.A. Ramirez, P.W. Shindo, F. Medina, R.B. Wicker, W.M. Keck, Fabrication of Metal and Alloy Components by Additive Manufacturing: Examples of 3D Materials Science, (2012). https://doi.org/10.1016/S2238-7854(12)70009-1.

[102] Z. Li, B. He, Q. Guo, Strengthening and hardening mechanisms of additively manufactured stainless steels: The role of cell sizes, Scr. Mater. 177 (2020) 17–21. https://doi.org/10.1016/j.scriptamat.2019.10.005.

[103] P. Krakhmalev, I. Yadroitsava, G. Fredriksson, I. Yadroitsev, MICROSTRUCTURAL AND THERMAL STABILITY OF SELECTIVE LASER MELTED 316L STAINLESS STEEL SINGLE TRACKS, South African J. Ind. Eng. 28 (2017) 12–19. https://doi.org/10.7166/28-1-1466.

[104] D.A. Porter, K.E. Easterling, Phase Transformations in Metals and Alloys, CRC Press, 2009.

[105] R.A. Winholtz, Separation of Microstresses and Macrostresses, in: Meas. Residual Appl. Stress Using Neutron Diffr., Springer Netherlands, 1992: pp. 131–145. https://doi.org/10.1007/978-94-011-2797-4_8.

[106] A. Deal, I. Spinelli, A. Chuang, Y. Gao, T. Broderick, Measuring residual stress in Ti-6Al-4V with HR-EBSD, using reference patterns from annealed material, Mater. Charact. 175 (2021) 111027. https://doi.org/10.1016/j.matchar.2021.111027.

[107] N.J. Rendler, I. Vigness, Hole-drilling strain-gage method of measuring residual stresses, Exp. Mech. 6 (1966) 577–586. https://doi.org/10.1007/BF02326825.

[108] A.J. Allen, M.T. Hutchings, C.G. Windsor, Neutron diffraction methods for the study of residual stress fields, Adv. Phys. 34 (1985) 445–473.

[109] K.Z. Troost, P. Van Der Sluis, D.J. Gravesteijn, Microscale elastic-strain in the scanning electron determination microscope by backscatter Kikuchi diffraction, Cit. Appl. Phys. Lett. Appl. Phys. Lett. J. Appl. Phys. Phys. Lett. Kikuchi Bands Low-Energy Electron Diffr. J. Appl. Phys. 62 (1993) 1110–1112. https://doi.org/10.1063/1.1708642.

[110] A.J. Wilkinson, G. Meaden, D.J. Dingley, High resolution mapping of strains and rotations using electron backscatter diffraction, Mater. Sci. Technol. 22 (2006) 1271–1278. https://doi.org/10.1179/174328406X130966.

[111] A.J. Wilkinson, G. Meaden, D.J. Dingley, Mapping strains at the nanoscale using electron back

scatter diffraction, Superlattices Microstruct. 45 (2009) 285–294. https://doi.org/10.1016/j.spmi.2008.10.046.

[112] Z. Wang, A.D. Stoica, D. Ma, A.M. Beese, Diffraction and single-crystal elastic constants of Inconel 625 at room and elevated temperatures determined by neutron diffraction, Mater. Sci. Eng. A. 674 (2016) 406–412. https://doi.org/10.1016/j.msea.2016.08.010.

[113] A. Paradowska, J.W.H. Price, R. Ibrahim, T. Finlayson, A neutron diffraction study of residual stress due to welding, J. Mater. Process. Technol. 164 (2005) 1099–1105. https://doi.org/10.1016/j.jmatprotec.2005.02.092.

[114] T. Machirori, F.Q. Liu, Q.Y. Yin, H.L. Wei, Spatiotemporal variations of residual stresses during multi-track and multi-layer deposition for laser powder bed fusion of Ti-6Al-4V, Comput. Mater. Sci. 195 (2021) 110462. https://doi.org/10.1016/j.commatsci.2021.110462.

[115] N. Tamura, R.S. Celestre, A.A. MacDowell, H.A. Padmore, R. Spolenak, B.C. Valek, N. Meier Chang, A. Manceau, J.R. Patel, Submicron x-ray diffraction and its applications to problems in materials and environmental science, Rev. Sci. Instrum. 73 (2002) 1369–1372. https://doi.org/10.1063/1.1436539.

[116] S.I. Wright, M.M. Nowell, D.P. Field, A review of strain analysis using electron backscatter diffraction., Microsc. Microanal. 17 (2011) 316–329. https://doi.org/10.1017/S1431927611000055.

[117] D.P. Field, Improving the Spatial Resolution of EBSD, Microsc. Microanal. 11 (2005). https://doi.org/10.1017/S1431927605506445.

[118] T.B. Britton, A.J. Wilkinson, Measurement of residual elastic strain and lattice rotations with high resolution electron backscatter diffraction, Ultramicroscopy. 111 (2011) 1395–1404. https://doi.org/10.1016/j.ultramic.2011.05.007.

[119] A.C. Leff, C.R. Weinberger, M.L. Taheri, Estimation of dislocation density from precession electron diffraction data using the Nye tensor, Ultramicroscopy. 153 (2015) 9–21. https://doi.org/10.1016/j.ultramic.2015.02.002.

[120] A.J. Wilkinson, G. Meaden, D.J. Dingley, High-resolution elastic strain measurement from electron backscatter diffraction patterns: New levels of sensitivity, Ultramicroscopy. 106 (2006) 307–313. https://doi.org/10.1016/j.ultramic.2005.10.001.

[121] D. Fullwood, M. Vaudin, C. Daniels, T. Ruggles, S.I. Wright, Validation of kinematically simulated pattern HR-EBSD for measuring absolute strains and lattice tetragonality, Mater. Charact. 107 (2015) 270–277. https://doi.org/10.1016/j.matchar.2015.07.017.

[122] M. Kamaya, Assessment of local deformation using EBSD: Quantification of accuracy of measurement and definition of local gradient, Ultramicroscopy. 111 (2011) 1189–1199. https://doi.org/10.1016/j.ultramic.2011.02.004.

[123] M.J. McLean, W.A. Osborn, In-situ elastic strain mapping during micromechanical testing using EBSD, Ultramicroscopy. 185 (2018) 21–26. https://doi.org/10.1016/j.ultramic.2017.11.007.

[124] M.D. Vaudin, W.A. Osborn, L.H. Friedman, J.M. Gorham, V. Vartanian, R.F. Cook, Designing a standard for strain mapping: HR-EBSD analysis of SiGe thin film structures on Si, (2014). https://doi.org/10.1016/j.ultramic.2014.09.007.

[125] T.B. Britton, A.J. Wilkinson, High resolution electron backscatter diffraction measurements of elastic strain variations in the presence of larger lattice rotations, Ultramicroscopy. 114 (2012) 82–95. https://doi.org/10.1016/j.ultramic.2012.01.004.

[126] K.A. Small, Z. Clayburn, R. DeMott, S. Primig, D. Fullwood, M.L. Taheri, Interplay of dislocation substructure and elastic strain evolution in additively manufactured Inconel 625, Mater. Sci. Eng. A. 785 (2020) 139380. https://doi.org/10.1016/j.msea.2020.139380.

[127] E.F. Rauch, M. Veron, Coupled microstructural observations and local texture measurements with an automated crystallographic orientation mapping tool attached to a tem, Materwiss. Werksttech. 36 (2005) 552–556. https://doi.org/10.1002/mawe.200500923.

[128] E.F. Rauch, J. Portillo, S. Nicolopoulos, D. Bultreys, S. Rouvimov, P. Moeck, Automated nanocrystal orientation and phase mapping in the transmission electron microscope on the basis of precession electron diffraction, Zeitschrift Für Krist. 225 (2010) 103–109. https://doi.org/10.1524/zkri.2010.1205.

[129] C. Xu, S. Gao, M. Li, A novel PCA-based microstructure descriptor for heterogeneous material design, Comput. Mater. Sci. 130 (2017) 39–49. https://doi.org/10.1016/j.commatsci.2016.12.031.

[130] A. Gupta, A. Cecen, S. Goyal, A.K. Singh, S.R. Kalidindi, Structure–property linkages using a data science approach: Application to a non-metallic inclusion/steel composite system, Acta Mater. 91 (2015) 239–254. https://doi.org/10.1016/j.actamat.2015.02.045.

[131] A. Shivanandan, A. Radenovic, I.F. Sbalzarini, MosaicIA: an ImageJ/Fiji plugin for spatial pattern and interaction analysis, BMC Bioinformatics. 14 (2013) 349. https://doi.org/10.1186/1471-2105-14-349.

[132] J.A. Helmuth, G. Paul, I.F. Sbalzarini, Beyond co-localization: inferring spatial interactions between sub-cellular structures from microscopy images, BMC Bioinformatics. 11 (2010) 372. https://doi.org/10.1186/1471-2105-11-372.

[133] X. Song, S. Feih, W. Zhai, C.-N. Sun, F. Li, R. Maiti, J. Wei, Y. Yang, V. Oancea, L. Romano Brandt, A.M. Korsunsky, Advances in additive manufacturing process simulation: Residual stresses and distortion predictions in complex metallic components, Mater. Des. 193 (2020) 108779. https://doi.org/10.1016/j.matdes.2020.108779.

[134] J. Cao, M.A. Gharghouri, P. Nash, Finite-element analysis and experimental validation of thermal residual stress and distortion in electron beam additive manufactured Ti-6Al-4V build plates, J. Mater. Process. Technol. 237 (2016) 409–419. https://doi.org/10.1016/j.jmatprotec.2016.06.032.

[135] H. Xu, R. Liu, A. Choudhary, W. Chen, A Machine Learning-Based Design Representation Method for Designing Heterogeneous Microstructures, in: Vol. 2B 40th Des. Autom. Conf., American Society of Mechanical Engineers, 2014. https://doi.org/10.1115/DETC2014-34570.

[136] M. Jiang, G. Monnet, B. Devincre, On the origin of the Hall–Petch law: A 3D-dislocation dynamics simulation investigation, Acta Mater. 209 (2021) 116783. https://doi.org/10.1016/j.actamat.2021.116783.

[137] N. Bertin, R.B. Sills, W. Cai, Frontiers in the Simulation of Dislocations, Annu. Rev. Mater. Res. 50 (2020) 437–464. https://doi.org/10.1146/annurev-matsci-091819-015500.

[138] BYU - OpenXY, (2018). https://github.com/BYU-MicrostructureOfMaterials/OpenXY.

Chapter 2. Precision Modification of Microstructure and Properties through Laser Engraving

Introduction

Processing of metallic parts by lasers is an active area of research due to the desire for local functionality and the capability of laser processing for microstructural modification [1–3]. Surface laser processes include heating, melting, and vaporization, each dependent on the peak surface temperature as well as the laser's thermal dwell time. Different laser surface processes can be applied for various desired results; for instance, vaporization of component surfaces with a laser enables welding and cutting, while surface melting may result in transformation hardening [3,4]. Laser surface modification (LSM) has been widely used in tool steels in an effort to increase their performance by altering the surface structure through laser treatment; techniques including laser alloying and laser cladding have been used to alter the surface properties of various metal alloys [5–7]. Methods of laser processing including laser polishing have emerged as structure and property tailoring methods as well. Laser surface treatment was found to significantly improve corrosion resistance in Ti-6Al-4V as well as producing a smooth, crack free surface [8] while laser surface quenching was used to eliminate selective phase corrosion in Nickel-Aluminum Bronze by transforming the surface layer to a single phase, fine grained structure [9].

Lasers are also being intensely investigated for component fabrication through additive manufacturing (AM) processes including selective laser melting and direct laser deposition due to the variable microstructures and mechanical properties resulting from high cooling rates and wide thermal gradients [10–12]. While AM is promising in many industries for complex part

manufacturing and repair, AM built components and surfaces often require post-processing either for enhanced mechanical properties or due to surface roughness [13]. The surface of AM parts usually exhibits a high degree of surface roughness with features such as unmelted particles and the staircase effect due to layer-by-layer fabrication. Several post-processing techniques, including mechanical, chemical and laser methods, have been used in the attempt to improve the surface of AM components [14]. Laser polishing is a promising method in which the surface layer is remelted to result in a smooth surface and modified microstructure, without chemical contamination or mechanical polishing media [15,16]. In addition to resulting in a substantially reduced surface roughness, Chen et al. observed increased tensile strength and dislocation density, including cellular substructures, on the surface of stainless steel 316L fabricated by laser AM after laser polishing [15].

Laser engraving of metallic surfaces has been popularized as a method of direct part marking (DPM) in aerospace and biomedical industries, replacing barcode technology for part identification and tracking [17]; an example of a 2D data matrix used for part marking can be seen in Figure 1. This has resulted in changes to the properties of components, leading to several experimental investigations in an effort to put forward process maps for laser parameters based on specific alloys to optimize marking readability and component properties [18–22]. High temperatures and fast cooling rates imparted by the engraving laser result in a fine grained and defect-dense microstructure that resists wear, improves biocompatibility and increases corrosion resistance [23,24]. The microstructural effects of laser melting and the properties conferred by specialized surface modifications have been well documented in tool steels [25–29], however the microstructural tailoring which is possible with such modification is

less understood in other alloys. In addition to controlling global surface properties, laser modification provides a path toward precision tailoring of local microstructures.

During the engraving process, relatively low amounts of energy are imparted to the material as compared to the thermal mass of the part, meaning heating and cooling rates are very high. As a result, laser processing can cause phase transformations far from equilibrium, such as the martensite transformation in steels [30]. Laser processing of structural components can result in stress concentrators, including notches; Donaldson concluded that powder metallurgy (PM) materials are sensitive to notches, which can result in decreased fatigue performance due to increased stress [31]. In this study we use laser engraving as a model system of the effect of localized microstructural modification through laser processing by demonstrating the change in mechanical fatigue after laser engraving and microstructural characterization of intact components. A thermal simulation of the laser engraving process is used to inform microstructural observations including phase transformations.

We use electron backscatter diffraction (EBSD) and optical microscopy to determine changes to these microstructural features resulting from two laser engraving schemes: light engraved (LE), in which the laser passes over the sample in a 2D data matrix pattern one time, and deep engraved (DE), in which the laser passes over the sample in the identifying pattern five times. It is expected that these two schemes will result in noticeable microstructural differences due to the difference in thermal profiles. The DE sample is exposed to repeated laser passes and, therefore, a comparatively long time at elevated temperature while the LE sample returns to ambient temperature after a single laser pass and with a fast cooling rate (within the regime for rapid solidification (RS) [32]). The thermal profiles of the two laser

schemes are simulated using high-fidelity computational fluid dynamics (CFD) simulations with a commercial software, FLOW-3D.

We demonstrate that Geometrically Necessary Dislocation (GND) density and intragranular misorientation are higher in the LE sample, while the presence of martensite is observed only in the DE specimen. A thermal simulation is used in tandem with microstructural observations to identify optimal (or sub-optimal) thermal environments for phase evolution and dislocation arrangement. It is found that a thin martensite surface layer results and fatigue strength decreases in DE laser engraved sample. Our analysis sheds light on the thermal profile necessary to cause martensitic transformations in laser engraved ferritic steels, working toward local microstructure tailoring. Our results suggest that in order to prevent substantial martensite from forming the amount of time above the ferrite-austenite transition temperature should be minimized.

Methods

Material

FC-0208 is the MPIF Standard 35 designation for a powder metallurgy high-carbon content steel comprised of Fe, 2wt% Cu and 0.8wt.% C [33] and was used for the experiments in the as-sintered condition. Prior to engraving, the sample exhibits a fine pearlite microstructure (**Error! Reference source not found.**2). FC-0208 is widely used in the P/M industry and has well-d efined mechanical properties [34].

The powder mix was compacted into transverse rupture strength (TRS) test specimens using a hydraulic press and sintered using an Abbott Belt Furnace at GKN Hoeganaes

Corporation to a target density of 6.9 g/cm^3. The TRS specimens comply with the geometry defined by MPIF Standard 41. Final chemistry was determined using a LECO Carbon analyzer and PANalytical XRF system at GKN Hoeganaes to ensure that the material complies with MPIF Standard 35 (Table 2-2).

Figure 2-14. Schematic of line engraved and an example of a 2D data matrix achieved by laser engraving.

Table 2-2. Composition of FC-0208 Steel

wt. % Fe	**wt. % C**	**wt. % Cu**
97.68	0.84	2.03

FC-0208 as-sintered samples were engraved using a Ytterbium fiber laser according to part marking standards defined by Fiat Chrysler Automobiles (FCA) [35]. Line and 2D matrix samples were engraved using light or deep laser parameters (described in

Type	Power (W)	Mark Speed (mm/s)	Laser Frequency (KHz)	Measured Spot Size (mm)	No. of Passes
Light Engraved (LE)	60	635	10	.127	1
Deep Engraved (DE)	60	508	10	.127	5

). Line engraved DE samples were used for fatigue testing while 2D matrix engraved samples were used for microstructural characterization (Figure 1).

Table 2-3. Sintering Conditions of PM FC-0208

Temperature (°C)	Belt Speed (mm/s)	Atmosphere [$\%H_2/\%N_2$]
1121	1.16	10/90

Table 2-4. Laser Engraving Parameters of PM FC-0208

Type	Power (W)	Mark Speed (mm/s)	Laser Frequency (KHz)	Measured Spot Size (mm)	No. of Passes
Light Engraved (LE)	60	635	10	.127	1
Deep Engraved (DE)	60	508	10	.127	5

Mechanical Testing

Fatigue testing was performed using CPMT standard cyclical 3-point-bend tests until sample failure. Low (LCF) and high (HCF) cycle fatigue tests were performed at maximum stresses of 525 and 208 MPa, respectively. The target number of cycles in LCF tests was 20,000 while a target of 200,000 cycles was set for the HCF tests. Fatigue testing was performed only on DE line engraved and as-sintered samples.

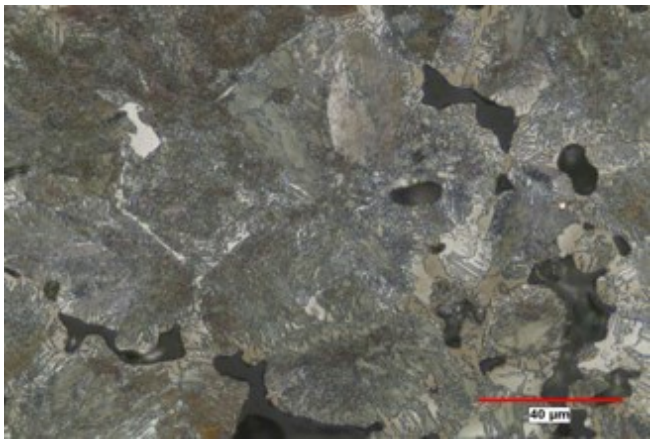

Figure 2-15. Microstructure of as-sintered FC-0208 before laser engraving.

Characterization

Optical microscopy was used to characterize the pre-engraving microstructure and measure the depth of the engraving. Electron backscatter diffraction (EBSD) was performed on a FEI XL30 ESEM using an EDAX collection system to characterize the orientation and phase of each sample. GND density was calculated using a method described by Leff, Weinberger, and Taheri [36] which uses the Nye tensor lower bound.

Simulation

High-fidelity computational fluid dynamics (CFD) simulations were implemented using FLOW-3D. This model numerically solves coupled mass, energy and momentum conservation equations, and tracks the fluid surface (void/liquid interface) via Volume of Fluid Advection with the split Lagrangian method; a more comprehensive overview can be found in [37–39]. Thermo-physical properties were based on a 1% C steel of similar composition, and can be found in Table 4, with all properties (e.g. density, thermal diffusivity, surface tension, vapor pressure) as temperature-dependent when applicable. The heat input from the laser was imposed on the top free surface, assuming a Gaussian distribution, and modeled as vertical rays that undergo partial absorption (depending on the material's absorption coefficient) and reflect until the ray flux is <5% of its initial value [40,41].

In this study, two engraving simulations were carried out "light" and "deep" engraving passes, 450 µm in length. The 3D computational domain had the following dimensions: 2472 µm (length, or the x-direction), 720 µm (width, or the y-direction), and 804 µm (height, or the z-direction). A coarse mesh (12 µm grid spacing) was used for the simulation volume to capture heat transfer, and a finer mesh (6 µm grid spacing) was used in the region exposed to the laser and where the material underwent a phase transformation from solid-to-liquid. The laser geometry and parameters mirrored those included in Table 3. The light and deep engraving simulations took ~2 and ~6 hours of CPU clock time, respectively, using a workstation with an Intel(R) Core(TM) i9-7940x CPU @3.10 GHz and 64 GB RAM.

Table 2-5. Thermo-physical properties of FC-0208.

Property	Value	Temperature Range [K]
Melting Point [K]	Solidus	1643
	Liquidus	1743
Enthalpy of Fusion [J/g]	277	-
Enthalpy of Vaporization [J/g]	7880	-
Density [g/cm^3]	$4.42 - 1.6 \times 10^{-4}$ *(Tempature-298K)	298-1643
	$4.21 - 5 \times 10^{-5}$ *(Tempature-1643K)	1643-1743
	$4.205 - 2.5 \times 10^{-4}$ *(Tempature-298K)	1743-3533
Specific heat [J/g/K]	$0.546 + 4.9 \times 10^{-4}$ *(Tempature-298K)	298-1643
	$.72 + 1.2 \times 10^{-4}$ *(Tempature-1743K)	1643-1743
	8.31	1743-3533
Thermal conductivity [W/cm/K]	$0.07 + 1.3 \times 10^{-4}$ *(Tempature-298K)	298-1643
	$0.246 + 0.9 \times 10^{-4}$ *(Tempature-1743K)	1643-1743
	0.346	1743-3533

Surface tension [g/s^2]	1800-0.25 *(Tempature-1743.15K)	1743-3533
Viscosity [g/cm/s]	0.0325-4x10^{-4} *(Temperature-1743K)	1743-3533
Saturation Pressure [Pa]	1.013x10^5	-
Absorption coefficient	0.4	298-3533

Results

High cycle (HCF) and low cycle (LCF) fatigue tests were performed on both as-sintered and DE line engraved TRS bars, with a maximum load of 208 and 525 MPa, respectively. Figure 3 demonstrates that the DE laser parameters decrease the fatigue strength in both mechanical tests, with the average number of cycles before failure in the HCF tests decreasing by 50% after engraving. Interestingly, the standard deviation decreased in the engraved samples in both HCF and LCF tests.

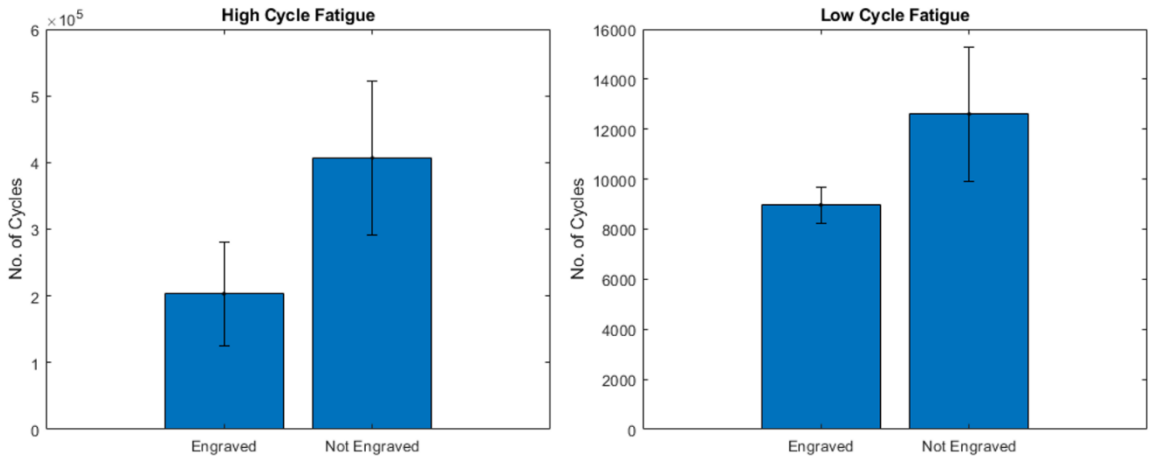

Figure 2-16. Average number of cycles before failure in as-sintered and DE line engraved TRS samples.

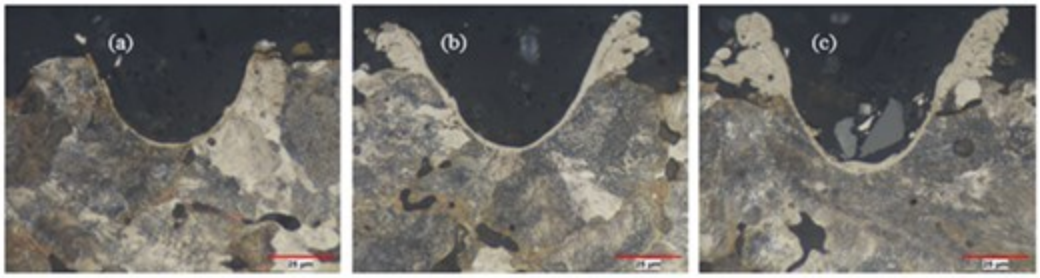

Figure 2-17. Optical micrographs of DE laser engraved FC-0208 at 3, 6, and 9mm along the length of line engraving showing increased depth of HAZ near the end of the engraving.

Due to the current interest in LST and laser polishing for improvement of mechanical properties and surface roughness, this decrease in fatigue strength warrants an inspection of the microstructure in laser engraved metal. Other laser processing techniques have found martensitic transformations in various alloys due to rapid solidification which affected mechanical and electrochemical properties. To investigate the initiation of martensite, our microstructural characterization was carried out on two levels of laser treatment. Optical and electron microscopy were used to characterize the different microstructures in as-sintered and laser engraved samples, including both LE and DE parameters. Optical microscopy of DE line engraved samples was performed to determine any change in the HAZ as the laser travels across the sample (**Error! Reference source not found.**). There is a phase difference at the s urface of the engraving that increases in depth with length along the engraving. This phase (light gray in **Error! Reference source not found.**) is thought to be martensite due to the known e ffect of case hardening steels where a laser beam causing the surface to transform to austenite is followed by self-quenching by conduction, transforming the surface to martensite [4]. Optical micrographs exhibit increasing depths of HAZ with increased distance along the length

of engraving, with the HAZ penetrating to 1.2µm at 3mm from the beginning of the track to 4µm at 9mm from the beginning of the track.

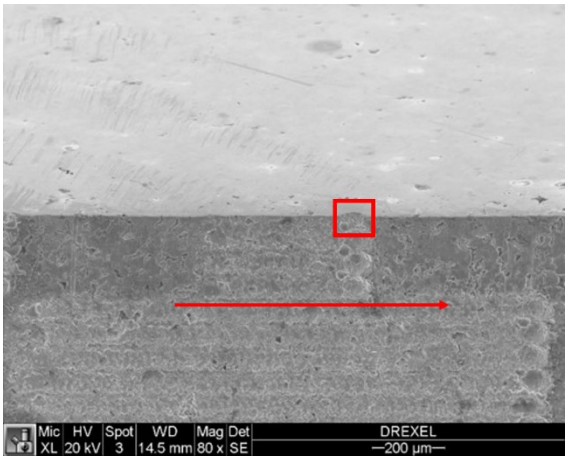

Figure 2-18. SE image of laser engravings in 2D matrix pattern. Red box shows location of EBSD scans in both light and deep engraved samples.

Electron microscopy of 2D matrix LE and DE engraved samples was performed in the location shown in **Error! Reference source not found.**, where the laser direction is denoted by a r ed arrow. Several laser tracks make up the overall matrix pattern engraved on the surface, and at the end of each individual track there is a depression left by the melting of material. Our characterization was carried out at the bottom of this depression, in an effort to characterize the metal which reaches the highest temperatures. The cross-section of the sample was analyzed at the end of a laser track to examine changes in microstructure versus depth. The same location was observed in both light and deep engraved samples.

EBSD maps in **Error! Reference source not found.** give more information about the m icrostructure at the end of laser engraving in 2D matrices. **Error! Reference source not found.** shows the inverse pole figure (IPF) for orientation analysis and the grain relative orientation

distribution (GROD) for relative misorientation within grains. There are larger grains with more intragranular rotation on the surface of the LE sample, while smaller grains of uniform orientation are seen in the GROD maps of the DE sample. Additionally, using TSL OIM analysis software it is found that the light engraving sample has a higher fraction of low angle grain boundaries (LAGBs, <15deg) than the deep engraved sample (18.6% and 13.2%, respectively) due to the decreased time at elevated temperature in the LE sample. It can be seen in the DE sample that grain size increases as distance from the HAZ of the laser increases; the red horizontal line in **Error! Reference source not found.**d is at 15um depth and separates small g rains of consistent orientation at shallower depths from larger grains with substantial misorientation at increasing depths. This may be the extent of the HAZ in the deep engraved sample.

GND density is shown in Figure 7 for the LE and DE engraved samples. The average GND density in each sample is 1.8e15 m^{-2} (LE) and 1.5e15 m^{-2} (DE). The slight decrease in GND density in the dark engraved sample suggests that some dislocation movement or annihilation may occur during repeated laser passes at sustained elevated temperatures. We have previously shown decreased dislocation density at increased depths from the surface in laser AM IN625, which is due to the cyclic thermal process of the AM method exposing deeper layers to increased temperatures and enabling a degree of recovery and dislocation movement [42].

Phase maps shown in **Error! Reference source not found.** demonstrate that the DE laser s cheme results in an increased presence of martensite in P/M FC-0208. Additionally, ferrite was not seen at all in the DE sample while cementite and ferrite phases are both present in the LE sample. The increased presence of martensite in the DE sample is a result of fast solidification

rates within the range of rapid solidification (RS) and increased time above austenitizing temperature. Although the LE sample has a peak cooling rate also within the RS regime, it is an order of magnitude slower than the maximum rate of the DE sample. This, combined with the increased temperature and time above transition temperature of the DE sample, could explain the relative absence of martensite in the LE FC-0208.

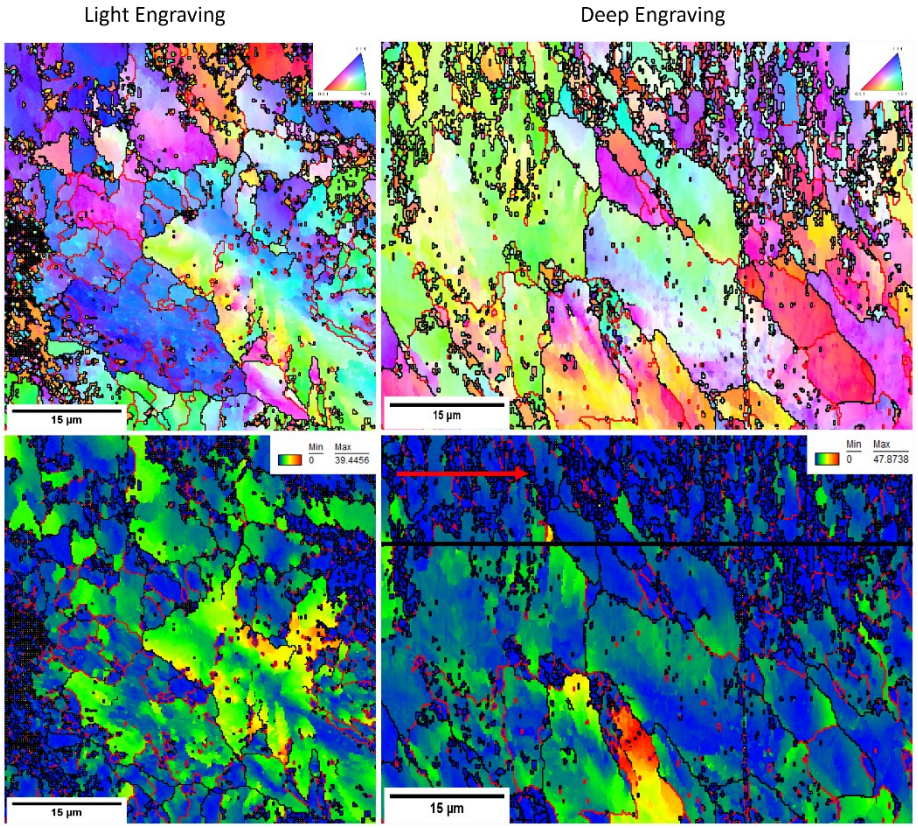

Figure 2-19. Inverse pole figure (IPF, top) and grain relative orientation distribution (GROD, bottom) of light and deep engraved samples. Red arrow shows laser scan direction.

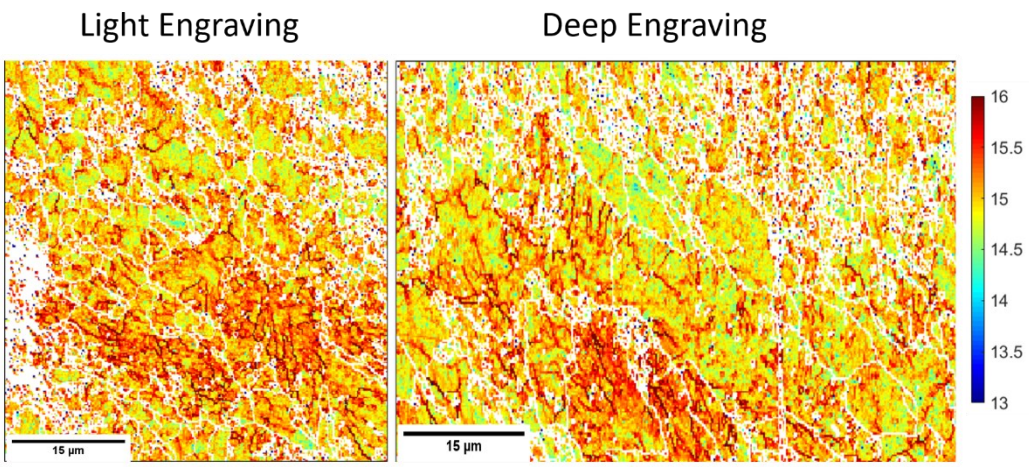

Figure2- 20. GND density of light and deep engraved P/M FC-0208. Scale bar is in 10x/m. White lines are high angle grain boundaries.

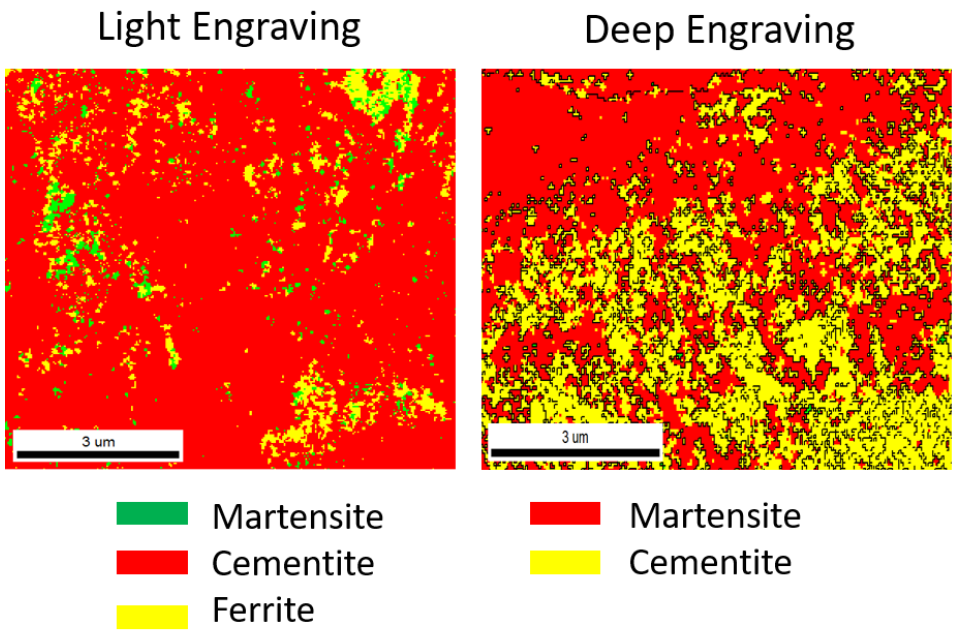

Figure 2-21. Phase maps of LE and DE samples showing increased martensite presence in deep engraved sample

Thermal simulation of repeated laser line engravings was done using FLOW-3D. In an approximation of the 2D matrix pattern, several line engravings parallel to each other were simulated. The thermal gradients in this simulation show that a higher temperature is reached

in the deep engraving compared to the light engraving (Table 4). The light engraving, **Error! R eference source not found.**, where only one laser pass is used, has a peak surface temperature of 2194.9K, while in the deep engraving, **Error! Reference source not found.**, the peak surface temperature reaches 2512.6K on the fifth laser pass, both well above the ferrite-austenite transition temperature for .8% C steel. In fact, the surface of the DE sample exceeds the melting temperature of the alloy, this results in fluid flow and a sharp decrease in the surface temperature because the simulation window remains at a fixed coordinate location (Figure 10). Cooling rates for both light engraving and deep engraving resulted in speeds in the rapid solidification (RS) regime, with cooling rates reaching 10^7 K/s on the surface of both light and deep engraving methods.

Table 2-6. Peak Temperatures and Cooling Rates in Light and Deep engraved P/M FC-0208

Depth (μm)	**Peak Temperature (K) Light engraving**	**Peak Temperature (K) Deep engraving**	**Peak Cooling Rate (K/s) Light engraving**	**Peak Cooling Rate (K/s) Deep engraving**
Surface	2194.9	2512.6	-1.03×10^7	-1.40×10^8
10	1853.7	2222.7	-7.52×10^6	-1.29×10^7
20	1492.2	1851.2	-3.99×10^6	-6.71×10^6
30	1222.4	1584.2	-2.01×10^6	-4.31×10^6

40	1016.2	1378.2	-1.11×10^6	-2.35×10^6

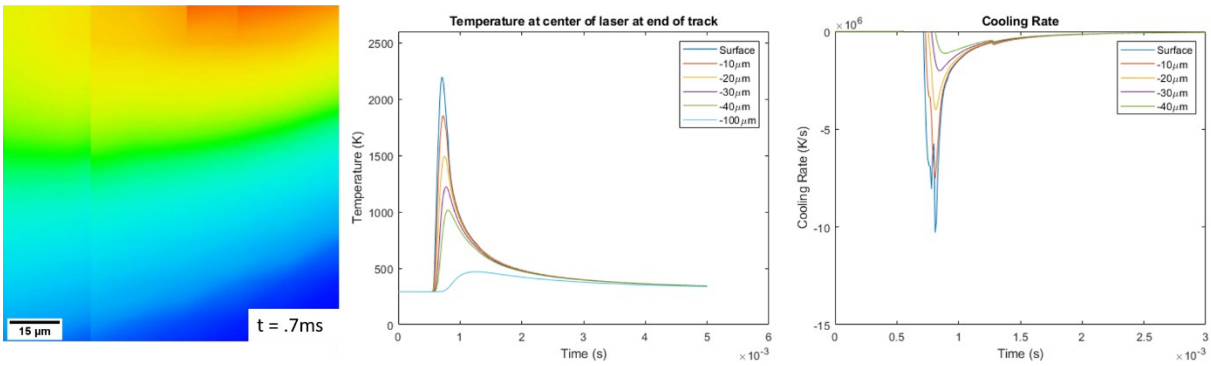

Figure 2-22. Thermal simulation of light engraving

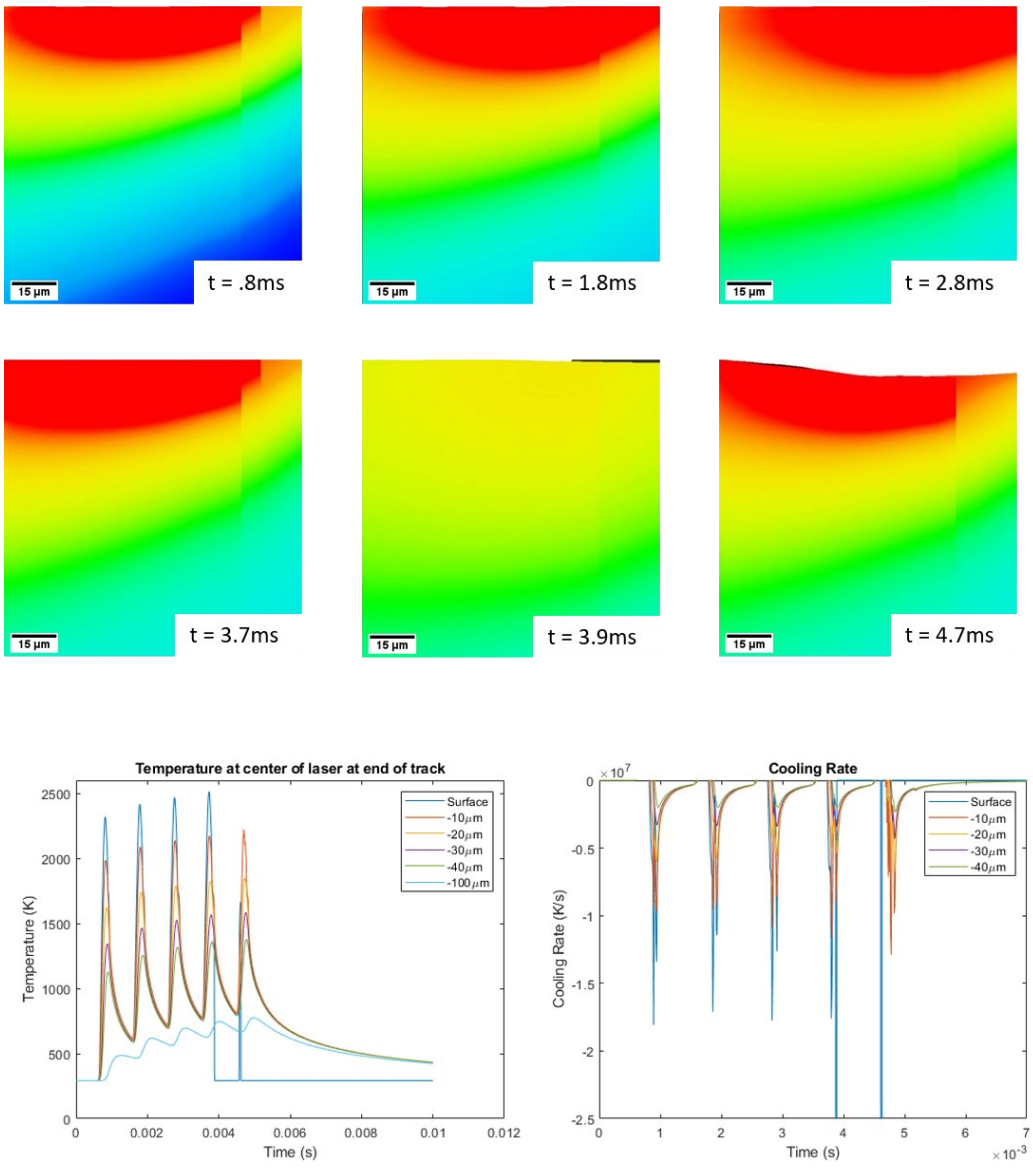

Figure 2-23. Thermal simulation of deep engraving.

Discussion

A 50% decrease in fatigue life in FC-0208 after DE laser processing suggests a severely altered microstructure, specifically that martensite may have formed during solidification. Due to fast solidification rates, the elemental distribution and phases present in laser processed materials vary greatly from those fabricated by conventional means. Martensite has been seen in laser processed alloys and has increased hardness and surface properties of these

components [4,43,44]. Pantsar found that a lower surface temperature in laser hardened steel results in only minor hardening, indicating the lack of martensite near the surface [45]. Similarly, in this study the lack of martensite in the LE sample is attributed to the limited time spent above austenitic temperature compared to the DE sample, which reached melting temperature and spent more time at increased temperatures.

Results of fatigue testing in laser processed metals have seen mixed results. Branza, et al. investigated the effect of laser weld repair on the low-cycle fatigue of a cast, heat resistant stainless steel and found that laser welded specimens always resulted in decreased fatigue life. In addition to the imposed mis-match between additional welding material and base material, the study found that the main detrimental effect was increased stiffness of welded samples, resulting in increased stress when exposed to an applied strain [46]. Laser clad repair also significantly reduced the fatigue life of AISI 4340 ultra-high strength steel when the clad material was AISI 4340, but improved the fatigue life if AerMet 100 steel was used [47]. Laser engraving of steel parts has resulted in increased corrosion and fatigue resistance in biomedical implants, and selective laser melted steels have demonstrated decreased fatigue life compared with wrought parts [22,48]. It is clear that when it comes to laser treatment, the resulting mechanical properties depends on the method of laser treatment as well as the parameters used (laser speed and power, atmospheric gas). Our fatigue results demonstrate decreased fatigue life of laser engraved steel and highlight that the extent of laser processing is an important factor in the resulting microstructural evolution.

Local control of microstructure and properties may be possible using laser processing techniques. Karimi, et al. found increased corrosion resistance in stainless steel 316L fabricated

by L-PBF when compared to the wrought alloy because of decreased elemental segregation; similarly, Yue et al. found significantly reduced pitting corrosion in Ti-6Al-4V after excimer laser treatment due to limited alloy partitioning [8,49]. Both of these instances of improved electrochemical properties are believed to be due to the rapid solidification rates during laser processing, which prevent elemental segregation and formation of harmful phases that would occur in relatively slower cooled samples. Knowledge of the thermal environments that give rise to unique microstructures is necessary if local control is to be successful. For instance, laser engraving a specific region of a component to enhance that areas corrosion resistance may be possible while still keeping the bulk scale mechanical properties at the necessary levels. Here, the extent of laser engraving was seen to influence the microstructural change of FC-0208. The top 15um in the LE sample shows larger grains with higher misorientation than the DE sample. Figure 8 shows that the maximum temperature at 20um in the LE sample is about 1500K, while the maximum temperature at 20um in the DE sample is 1850K. Melting temperature of FC-0208 is around 2500K, which is exceeded only at the surface of the DE sample where martensite was found.

Dislocations and dislocation structures are known to inform mechanical properties on the bulk scale. Dislocation density is typically higher in laser processed components, which has resulted in improved mechanical properties [50]. Here, increased dislocation density in the DE samples compared to the as-sintered samples appears to have contributed to a 50% decrease in fatigue life. However, the increase in dislocation density does not occur until a 20um depth, suggesting that fatigue cracks may initiate in the martensite at the surface of the sample due to increased residual stresses which are known to occur during laser processing, and then travel

through the bulk of the sample leading to a quick fatigue failure compared to the pearlitic microstructure first seen in the as-sintered FC-0208. The phase transformation from ferrite to martensite in the DE condition is due to the combination of time at austenitizing temperature and fast quenching rates. The austenization of plain carbon steel takes place above 1000K, a temperature largely surpassed by both the LE and DE methods. However, homogenization of austenite requires diffusion of carbon from high to low concentration regions to an extent that is dictated by time and temperature. Then, during quenching, the material with a carbon content above .05wt% is transformed to martensite, while the rest transforms to ferrite [4]. The decreased dislocation density in the DE condition supports this, demonstrating increased dislocation movement due to longer times at high temperature. This explains the relative absence of martensite in the LE condition – carbon did not have adequate time to diffuse from high to low concentrations, resulting in transformation of austenite to ferrite.

These results provide guidance for the use of lasers in DPM and in precision modification of microstructures. We have shown here that the extent, i.e. number of laser passes, of engraving affects the surface microstructure in FC-0208, a high carbon, industry relevant steel. Our results demonstrate that a single laser pass is enough to result in an observable marking on the part for DPM, while still preventing martensitic transformation on the surface and preserving the pre-marked fatigue properties. On the other hand, if lasers are to be used for precision modification of microstructures, a number of laser passes, for instance five, used here, is best for the transformation of the surface to martensite. Laser treated surfaces of single phase martensite have been seen previously to result in increased corrosion resistance due to

decreased elemental segregation [50]. Therefore, the number of laser passes is a process parameter to be manipulated for desired properties and surface microstructure.

Conclusions

- Fatigue life of P/M FC-0208 steel was significantly decreased by DE laser engraving of line in TRS sample bars due to the formation of a martensitic surface layer.
- LE and DE laser engraving conditions were simulated using a CFD model which demonstrated markedly increased temperatures and cooling rates in DE samples.
- Extent of laser engraving in 2D data matrix pattern results in varying levels of martensite transformation dependent on time sent above austenitizing temperature and cooling rate.
- Fewer laser passes may be best suited for DPM to preserve mechanical properties while still creating a visible mark, while a greater number of laser passes is necessary for modification of local microstructures for property modification

References

[1] M.H. Farshidianfar, A. Khajepour, A.P. Gerlich, Effect of real-time cooling rate on microstructure in Laser Additive Manufacturing, J. Mater. Process. Technol. 231 (2016) 468–478. https://doi.org/10.1016/j.jmatprotec.2016.01.017.

[2] R. Shi, S.A. Khairallah, T.T. Roehling, T.W. Heo, J.T. McKeown, M.J. Matthews, Microstructural control in metal laser powder bed fusion additive manufacturing using laser beam shaping strategy, Acta Mater. 184 (2020) 284–305. https://doi.org/10.1016/j.actamat.2019.11.053.

[3] J.C. Ion, H.R. Shercliff, M.F. Ashby, Diagrams for laser materials processing, Acta Metall. Mater. 40 (1992) 1539–1551. https://doi.org/10.1016/0956-7151(92)90097-X.

[4] M.F. Ashby, K.E. Easterling, The transformation hardening of steel surfaces by laser beams—I. Hypo-eutectoid steels, Acta Metall. 32 (1984) 1935–1948.

https://doi.org/10.1016/0001-6160(84)90175-5.

[5] C. Ma, G. Peng, L. Nie, H. Liu, Y. Guan, Laser surface modification of Mg-Gd-Ca alloy for corrosion resistance and biocompatibility enhancement, Appl. Surf. Sci. 445 (2018) 211–216. https://doi.org/10.1016/j.apsusc.2018.03.174.

[6] P. Volovitch, J.E. Masse, A. Fabre, L. Barrallier, W. Saikaly, Microstructure and corrosion resistance of magnesium alloy ZE41 with laser surface cladding by Al-Si powder, Surf. Coatings Technol. 202 (2008) 4901–4914. https://doi.org/10.1016/j.surfcoat.2008.04.052.

[7] J. Dutta Majumdar, I. Manna, Mechanical properties of a laser-surface-alloyed magnesium-based alloy (AZ91) with nickel, Scr. Mater. 62 (2010) 579–581. https://doi.org/10.1016/j.scriptamat.2009.12.047.

[8] T.M. Yue, J.K. Yu, Z. Mei, H.C. Man, Excimer laser surface treatment of Ti-6Al-4V alloy for corrosion resistance enhancement, Mater. Lett. 52 (2002) 206–212. https://doi.org/10.1016/S0167-577X(01)00395-0.

[9] Z. Qin, D.-H. Xia, Y. Zhang, Z. Wu, L. Liu, Y. Lv, Y. Liu, W. Hu, Microstructure modification and improving corrosion resistance of laser surface quenched nickel–aluminum bronze alloy, Corros. Sci. 174 (2020) 108744. https://doi.org/10.1016/j.corsci.2020.108744.

[10] P. Köhnen, M. Létang, M. Voshage, J.H. Schleifenbaum, C. Haase, Understanding the process-microstructure correlations for tailoring the mechanical properties of L-PBF produced austenitic advanced high strength steel, Addit. Manuf. 30 (2019) 100914. https://doi.org/10.1016/j.addma.2019.100914.

[11] K. Kunze, T. Etter, J. Grässlin, V. Shklover, Texture, anisotropy in microstructure and mechanical properties of IN738LC alloy processed by selective laser melting (SLM), Mater. Sci. Eng. A. 620 (2015) 213–222. https://doi.org/10.1016/j.msea.2014.10.003.

[12] A. Yadollahi, N. Shamsaei, Additive manufacturing of fatigue resistant materials: Challenges and opportunities, Int. J. Fatigue. 98 (2017) 14–31. https://doi.org/10.1016/j.ijfatigue.2017.01.001.

[13] E.R. Gordon, A. Shokrani, J.M. Flynn, S. Goguelin, J. Barclay, V. Dhokia, A surface modification decision tree to influence design in additive manufacturing, in: Smart Innov. Syst. Technol., Springer Science and Business Media Deutschland GmbH, 2016: pp. 423–434. https://doi.org/10.1007/978-3-319-32098-4_36.

[14] E. Maleki, S. Bagherifard, M. Bandini, M. Guagliano, Surface post-treatments for metal additive manufacturing: Progress, challenges, and opportunities, Addit. Manuf. 37 (2020) 101619. https://doi.org/10.1016/j.addma.2020.101619.

[15] L. Chen, B. Richter, X. Zhang, K.B. Bertsch, D.J. Thoma, F.E. Pfefferkorn, Effect of laser polishing on the microstructure and mechanical properties of stainless steel 316L fabricated by laser powder bed fusion, Mater. Sci. Eng. A. 802 (2021). https://doi.org/10.1016/j.msea.2020.140579.

[16] A.M.K. Hafiz, E. V. Bordatchev, R.O. Tutunea-Fatan, Influence of overlap between the laser beam tracks on surface quality in laser polishing of AISI H13 tool steel, in: J. Manuf. Process., Elsevier, 2012: pp. 425–434. https://doi.org/10.1016/j.jmapro.2012.09.004.

[17] C. Moss, S. Chakrabarti, D.W. Scott, Parts quality management: Direct part marking of data matrix symbol for mission assurance, in: 2013 IEEE Aerosp. Conf., IEEE, 2013: pp. 1–12. https://doi.org/10.1109/AERO.2013.6497372.

[18] E. Ahearne, Engineering the surface for direct part marking (DPM), CIRP J. Manuf. Sci. Technol. 29 (2020) 1–10. https://doi.org/10.1016/j.cirpj.2020.01.003.

[19] D.P. Davies, S.L. Jenkins, Characterisation of automated part marking methods for use in helicopter component identification, Int. J. Fatigue. 110 (2018) 71–80. https://doi.org/10.1016/j.ijfatigue.2018.01.004.

[20] L. Costa, K. Lansford, D. Rajput, W. Hofmeister, Unique corrosion and wear resistant identification tags via LISI^{TM} laser marking, Surf. Coatings Technol. 203 (2009) 1984–1990. https://doi.org/10.1016/j.surfcoat.2009.01.028.

[21] W. Jangsombatsiri, J.D. Porter, Laser Direct-Part Marking of Data Matrix Symbols on Carbon Steel Substrates, J. Manuf. Sci. Eng. 129 (2007) 583–591. https://doi.org/10.1115/1.2716704.

[22] P.J. Ogrodnik, C.I. Moorcroft, P. Wardle, The Effects of Laser Marking and Symbol Etching on the Fatigue Life of Medical Devices, J. Med. Eng. 2013 (2013). https://doi.org/10.1155/2013/570354.

[23] A. Hemmasian Ettefagh, H. Wen, A. Chaichi, M.I. Islam, F. Lu, M. Gartia, S. Guo, Laser surface modifications of Fe-14Cr ferritic alloy for improved corrosion performance, Surf. Coatings Technol. 381 (2020) 125194. https://doi.org/10.1016/j.surfcoat.2019.125194.

[24] S. Mohammadzadeh Asl, M. Ganjali, M. Karimi, Surface modification of 316L stainless steel by laser-treated HA-PLA nanocomposite films toward enhanced biocompatibility and corrosion-resistance in vitro, Surf. Coatings Technol. 363 (2019) 236–243. https://doi.org/10.1016/j.surfcoat.2019.02.052.

[25] P.R. Strutt, H. Nowotny, M. Tuli, B.H. Kear, Laser surface melting of high speed tool steels, Mater. Sci. Eng. 36 (1978) 217–222. https://doi.org/10.1016/0025-5416(78)90074-5.

[26] R. Vilar, R. Colaço, A. Almeida, Laser surface treatment of tool steels, Opt. Quantum Electron. 27 (1995) 1273–1289. https://doi.org/10.1007/BF00326481.

[27] P.A. Molian, H.S. Rajasekhara, Analysis of microstructures of laser surface-melted tool steels, J. Mater. Sci. Lett. 5 (1986) 1292–1294. https://doi.org/10.1007/BF01729397.

[28] S. Kąc, J. Kusiński, SEM and TEM microstructural investigation of high-speed tool steel after laser melting, Mater. Chem. Phys. 81 (2003) 510–512. https://doi.org/10.1016/S0254-0584(03)00062-2.

[29] Y.-W. Kim, P.R. Strutt, H. Nowotny, Laser melting and heat treatment of m2 tool steel: A microstructural characterization, Metall. Trans. A. 10 (1979) 881–886. https://doi.org/10.1007/BF02658307.

[30] J.C. Ion, Laser processing of engineering materials : principles, procedure and industrial application, Boston, 2005.

[31] I.W. Donaldson, Fatigue performance of powder metallurgy materials, 2019.

[32] E. Chlebus, K. Gruber, B. Kuznicka, J. Kurzac, T. Kurzynowski, Effect of heat treatment on the microstructure and mechanical properties of Inconel 718 processed by selective laser melting, Mater. Sci. Eng. A. 639 (2015) 647–655. https://doi.org/10.1016/j.msea.2015.05.035.

[33] MPIF, Standard 35 for PM Structural Parts, 2018 Edition, Metal Powder Industries Federation, Princeton, NJ, 2018.

[34] SSI Sintered Specialties, Carbon, Copper, and Nickel Steels, (n.d.). https://www.ssisintered.com/materials/carbon-copper-and-nickel-steels (accessed February 15, 2021).

[35] Fiat-Chrysler Automobiles, Powertrain Control Standards Section 17, 2011.

[36] A.C. Leff, C.R. Weinberger, M.L. Taheri, Estimation of dislocation density from precession electron diffraction data using the Nye tensor, Ultramicroscopy. 153 (2015) 9–21. https://doi.org/10.1016/j.ultramic.2015.02.002.

[37] M. Bayat, A. Thanki, S. Mohanty, A. Witvrouw, S. Yang, J. Thorborg, N.S. Tiedje, J.H. Hattel, Keyhole-induced porosities in Laser-based Powder Bed Fusion (L-PBF) of Ti6Al4V: High-fidelity modelling and experimental validation, Addit. Manuf. 30 (2019) 100835. https://doi.org/10.1016/j.addma.2019.100835.

[38] Y.S. Lee, W. Zhang, Modeling of heat transfer, fluid flow and solidification microstructure of nickel-base superalloy fabricated by laser powder bed fusion, Addit. Manuf. 12 (2016) 178–188. https://doi.org/10.1016/j.addma.2016.05.003.

[39] Y.C. Wu, C.H. San, C.H. Chang, H.J. Lin, R. Marwan, S. Baba, W.S. Hwang, Numerical modeling of melt-pool behavior in selective laser melting with random powder distribution and experimental validation, J. Mater. Process. Technol. 254 (2018) 72–78. https://doi.org/10.1016/j.jmatprotec.2017.11.032.

[40] S.A. Khairallah, A.T. Anderson, A. Rubenchik, W.E. King, Laser powder-bed fusion additive manufacturing: Physics of complex melt flow and formation mechanisms of pores, spatter, and denudation zones, Acta Mater. 108 (2016) 36–45. https://doi.org/10.1016/j.actamat.2016.02.014.

[41] W.E. King, H.D. Barth, V.M. Castillo, G.F. Gallegos, J.W. Gibbs, D.E. Hahn, C. Kamath, A.M. Rubenchik, Observation of keyhole-mode laser melting in laser powder-bed fusion additive manufacturing, J. Mater. Process. Technol. 214 (2014) 2915–2925.

https://doi.org/10.1016/j.jmatprotec.2014.06.005.

[42] K.A. Small, Z. Clayburn, R. DeMott, S. Primig, D. Fullwood, M.L. Taheri, Interplay of dislocation substructure and elastic strain evolution in additively manufactured Inconel 625, Mater. Sci. Eng. A. 785 (2020) 139380. https://doi.org/10.1016/j.msea.2020.139380.

[43] J. Yang, H. Yu, J. Yin, M. Gao, Z. Wang, X. Zeng, Formation and control of martensite in Ti-6Al-4V alloy produced by selective laser melting, Mater. Des. 108 (2016) 308–318. https://doi.org/10.1016/j.matdes.2016.06.117.

[44] M.H. Farshidianfar, A. Khajepouhor, A. Gerlich, Real-time monitoring and prediction of martensite formation and hardening depth during laser heat treatment, Surf. Coatings Technol. 315 (2017) 326–334. https://doi.org/10.1016/j.surfcoat.2017.02.055.

[45] H. Pantsar, Relationship between processing parameters, alloy atom diffusion distance and surface hardness in laser hardening of tool steel, J. Mater. Process. Technol. 189 (2007) 435–440. https://doi.org/10.1016/j.jmatprotec.2006.08.033.

[46] T. Branza, F. Deschaux-Beaume, V. Velay, P. Lours, A microstructural and low-cycle fatigue investigation of weld-repaired heat-resistant cast steels, J. Mater. Process. Technol. 209 (2009) 944–953. https://doi.org/10.1016/j.jmatprotec.2008.03.002.

[47] S. Da Sun, Q. Liu, M. Brandt, V. Luzin, R. Cottam, M. Janardhana, G. Clark, Effect of laser clad repair on the fatigue behaviour of ultra-high strength AISI 4340 steel, Mater. Sci. Eng. A. 606 (2014) 46–57. https://doi.org/10.1016/j.msea.2014.03.077.

[48] S. Afkhami, M. Dabiri, S.H. Alavi, T. Björk, A. Salminen, Fatigue characteristics of steels manufactured by selective laser melting, Int. J. Fatigue. 122 (2019) 72–83. https://doi.org/10.1016/j.ijfatigue.2018.12.029.

[49] M.H. Shaeri Karimi, M. Yeganeh, S.R. Alavi Zaree, M. Eskandari, Corrosion behavior of 316L stainless steel manufactured by laser powder bed fusion (L-PBF) in an alkaline solution, Opt. Laser Technol. 138 (2021) 106918. https://doi.org/10.1016/j.optlastec.2021.106918.

[50] S. Bahl, S. Mishra, K.U. Yazar, I.R. Kola, K. Chatterjee, S. Suwas, Non-equilibrium microstructure, crystallographic texture and morphological texture synergistically result in unusual mechanical properties of 3D printed 316L stainless steel, Addit. Manuf. 28 (2019) 65–77. https://doi.org/10.1016/j.addma.2019.04.016.

Chapter 3. Interplay of dislocation substructure and elastic strain evolution in additively manufactured Inconel 625

Introduction

Additive manufacturing (AM) techniques have garnered much interest in the manufacturing and metallurgy community due to their potential for decreased cost and time of fabrication of complex metal parts [1]. However, the parameters of these processes have not been fully optimized for reliable material properties of complex metal parts and this is an intense area of investigation for establishment of AM techniques in industries as varied as aerospace and medicine [2–5]. AM methods utilize a CAD model to print a 3D part layer by layer from raw materials in the form of powder or wire, thereby enabling fabrication of complex geometries using a single manufacturing process with minimal waste. There is a plethora of different AM techniques, each with unique processing parameters which result in varying microstructures and mechanical properties. In this study, we characterize samples fabricated by the additive technique direct metal laser sintering (DMLS), a powder bed technique in which layers of metal powder are rolled across a build plate in a defined thickness and melted by a high-powered laser to produce a 2D cross-section of the component. This process is iterated layer by layer to build the final 3D part. Additive techniques like DMLS results in material properties that differ from those of cast or wrought alloys; parameters including build direction, laser power, laser beam shape, scan speed and others can have a significant effect on various properties [6–10]. Large residual stresses imparted by complex thermal histories can result in distortion and cracking of DMLS built alloys during fabrication, making these components beyond the reach of mechanical recovery via post-processing heat

treatments [11–14]. Re-melting the first layer of powder and the inclusion of support structures have been suggested to mitigate residual stresses during manufacture, however, re-melting of the first layer was shown to have little effect on thermally induced stresses, while removal of support structures may destroy the final component [11,15]. Recently, laser diodes were used as an in-situ annealing strategy during laser AM of 316L stainless steel to largely reduce the macroscale residual stress during building [14]. The effect of these strategies on the microscale elastic strain is, however, uncharacterized. Therefore, the question of the influence of microscale elastic strain on microstructural evolution remains unanswered.

Despite the level of interest in additive manufacturing, the mechanisms of solidification and dislocation substructure formation at extreme temperatures and solidification rates are little understood. The cooling rate during DMLS fabrication has been found to be between 10^4-10^6 K/s, well above the necessary cooling rate for rapid solidification (RS), which has been defined as at least 10^3 K/s, and a microstructure typical of RS has been observed previously in DMLS fabricated IN625 [16–18]. The thermal environment of DMLS also includes steep thermal gradients and repetitive heating by the tracking laser, each of which contributes to complex, non-equilibrium microstructures and diverse material properties [16,17,19,20]. The microstructure induced by DMLS in several alloys has been observed to include metastable cellular structures within grains [21–23]. These cellular boundaries have a high density of dislocations and solute elements ejected during solidification and the structures have been shown to decompose with annealing. There is no suitable explanation for the mechanism of evolution of these metastable subgrain structures, which have been theorized to be a result of both chemical supersaturation at solidification fronts and thermally induced residual elastic

stresses [22–24]. Additionally, the effects of re-melting and the heat affected zone (HAZ) of subsequent laser tracking increases the complexity of the solidification environment and the extent of microstructural evolution during these laser passes is unknown.

The presence of intragranular cellular structures and their corresponding chemical and microstructural inhomogeneity suggests that the residual strain likely also has microscale, intragranular inhomogeneity. Characterizing these microscale inhomogeneities in strain could lead to deeper understanding of the origins of dislocation substructures as well as macroscale deterioration of material properties as dislocation motion and stress relaxation are inherent results of deformation in polycrystals [25]. Analysis of elastic strain on the microscale has been generally lacking until the developments of HR-EBSD cross-correlation in the scanning electron microscope (SEM) and nanobeam diffraction in the transmission electron microscope (TEM) made it possible to calculate intragranular elastic strain in polycrystalline metals [26,27]. While bulk and grain level residual stresses in DMLS have been studied using neutron and X-ray diffraction [28–34], the characterization of microstrains and their relation to dislocation substructures and additive building methods have not been investigated in detail until now. Here we use the HR-EBSD cross-correlation software OpenXY [35] and a Nye tensor dislocation density calculation [36] to observe relative distributions of elastic strain in relation to unique microstructural features induced by the DMLS process. We observe that intragranular metastable cellular structures contain decreased elastic strain variations while grains and intragranular regions without cell structures have highly varied elastic strain distributions. These results suggest that elastic strain content during manufacturing drives substructure evolution during rapid solidification in AM processing. By separating analysis of elastic and

plastic strains and observing their relative distributions, useful data about the solidification processes occurring during DMLS fabrication can be gained and fed into microscale simulations of DMLS and other nonequilibrium processes [37,38].

Table 3-7. Processing parameters for DMLS fabrication of IN625

Powder diameter (µm)	Ave.: 33.8
Joining Method	Yb-fibre laser
Laser Power (W)	195
Laser Speed (mm/s)	700
Layer Thickness (µm)	20
Post AM Processing	Stress Relieved: 870˚C/1hr
DMLS System	EOS M270

Methods

Fabrication and Sample Prep

An EOS M270 DMLS system was used to fabricate cubes (10x10x10 mm^3) of IN625 using the processing parameters in Table 1. These unique parameters have different effects on the final microstructures, and the residual strain at a certain point will depend upon its thermal history [32]. Printing was performed at Army ARDEC in Picatinny Arsenal, N.J. and followed by a

stress relieving step of 870°C/1hr. These processing parameters as well as the post-processing anneal were chosen in order to align with typical processing of IN625 on the EOS system.

IN625 samples were cut in half perpendicular to the build direction to expose the transverse face at a build depth of 5mm before being polished to 1200 grit using SiC paper and up to 1µm using diamond suspension. A Buehler VibroMet 2 vibropolisher was used with 0.04µm colloidal silica for 24 hours to arrive at an EBSD ready surface. Two scans were performed using 25kV and 1x1 binning:

1) 111,556 data points were collected using a 1.5µm step size showing multiple grains for observation of general microstructure and strain distribution using an EDAX TSL-OIM system on a FEI XL30 E-SEM.

2) 61,488 points data points were collected using a 50nm step size to observe local strain and GND density contained in intragranular cell structures using the EDAX system on a JEOL 7001F FE-SEM.

Scans were analyzed for orientation mapping using EDAX TSL-OIM Analysis software. The Kikuchi pattern from each location was stored for use in the OpenXY cross-correlation software.

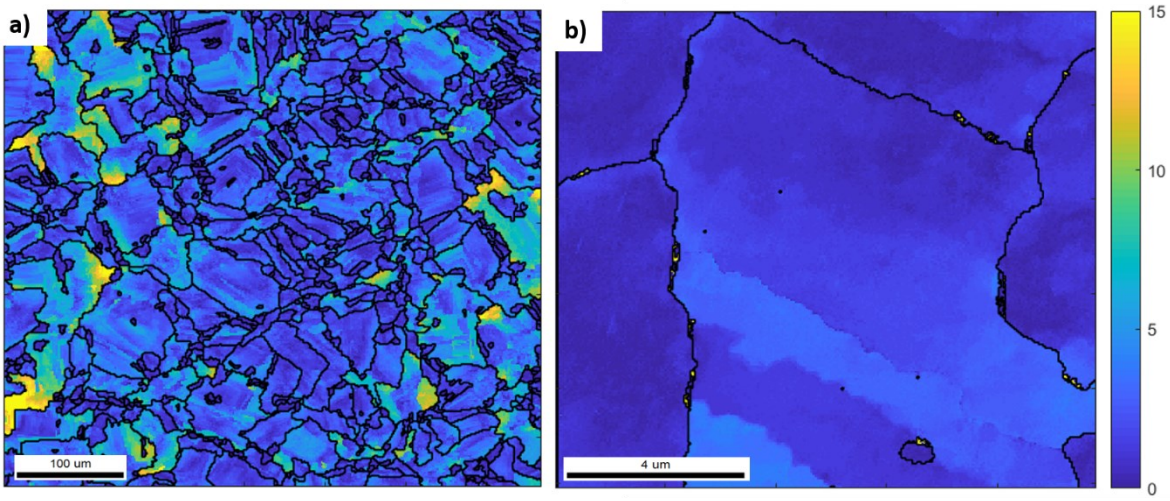

Figure 3-24. Misorientation from reference point in each grain (degrees) in a) scan 1 and b) scan 2.

Strain and GND Analysis

The open source cross-correlation code OpenXY computes the relative strain between a selected reference point in a grain and all other points by detecting differences between their Kikuchi patterns. Cross-correlation is used to detect shifts between the reference and current pattern for several regions of interest (ROIs) in a method first outlined by Wilkinson, Meaden and Dingley [26].

If significant misorientation exists between the reference and experimental pattern, the features in a given ROI within a reference pattern may be in a different location or even absent on experimental patterns and cross-correlation analysis will fail, resulting in phantom strain error and strain overestimation [39].

An improvement to the cross-correlation method outlined by Britton and Wilkinson, called remapping, ensures the reference and experimental pattern are in a similar orientation to minimize the strain error brought about by misorientation between patterns [39]. However,

this method was shown to be effective only up to misorientations of 10°, while misorientations within grains of up to 20° are observed here (Fig. 1a). To minimize the influence of intragranular orientation gradients on the calculation of elastic strain, a modification was implemented in which a rotation tolerance limits the misorientation between reference and experimental patterns. The rotational tolerance should be chosen to be as large as possible to maximize the area being compared to one reference pattern within a grain [40]. With this in mind, we use rotational tolerances of 10° and 4° in scans 1 and 2, respectively. This discrepancy is due to the lower maximum misorientation (4.3°) across scan 2 (figure 1b). We then reduce the allowed angle between reference and test patterns in OpenXY to 2° to examine relative strain contained in metastable cell structures bound by dislocation dense low angle grain boundaries (LAGBs). This allows more than one reference point per TSL OIM defined grain.

There is also a danger of a 'bad' reference point, which is highly misoriented from most patterns in a grain, being chosen by the algorithm in OpenXY. To minimize the chance of choosing a bad reference point, we have modified the selection algorithm to require that the reference pattern is close to the average orientation of the grain or subregion specified by the rotational tolerance.

An estimation of the GND density is performed using the Nye tensor dislocation method described by Leff, Weinberger, and Taheri [36]. The dislocation density values are then mapped across the sample, allowing direct comparison of local elastic strain values with local dislocation density and dislocation substructures.

Results

Microstructure

GND density of both scans is shown in Figure 3-2, where the maximum of scan 1 ($1.5x10^{15}$) is lower by an order of magnitude than that of scan 2 ($1.6x10^{16}$). Likewise, the average density of scan 1 is lower than that of scan 2 ($1.2x10^{14}$ and $7.0x10^{14}$, respectively). This can be attributed to the decreased step size in scan 2 and is a result of a higher fraction of dislocations being interpreted as GNDs at smaller step sizes [36]. A noticeable organization of dislocations into linear LAGBs (1-2°) is observed in many grains (notated in Fig. 3-2b).

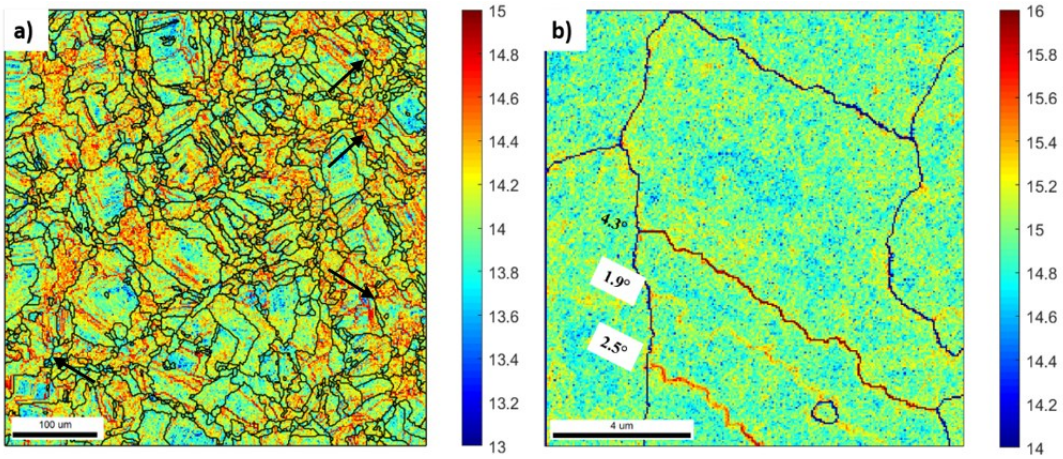

Figure 3-25. Dislocation density in scan 1 (a) and scan 2 (b) of DMLS IN625. Linear dislocation structures are noticeable in both scans. Color scale is in 10x. Note the difference in scale.

These dislocation dense structures often accompany regions of misorientation in the inverted pole figure (IPF) and grain relative orientation deviation (GROD) maps, shown in figure 3-3. GROD tracks intragranular misorientation relative to the average orientation within the grain – in this case similar to the misorientation from reference pattern in figure 1.

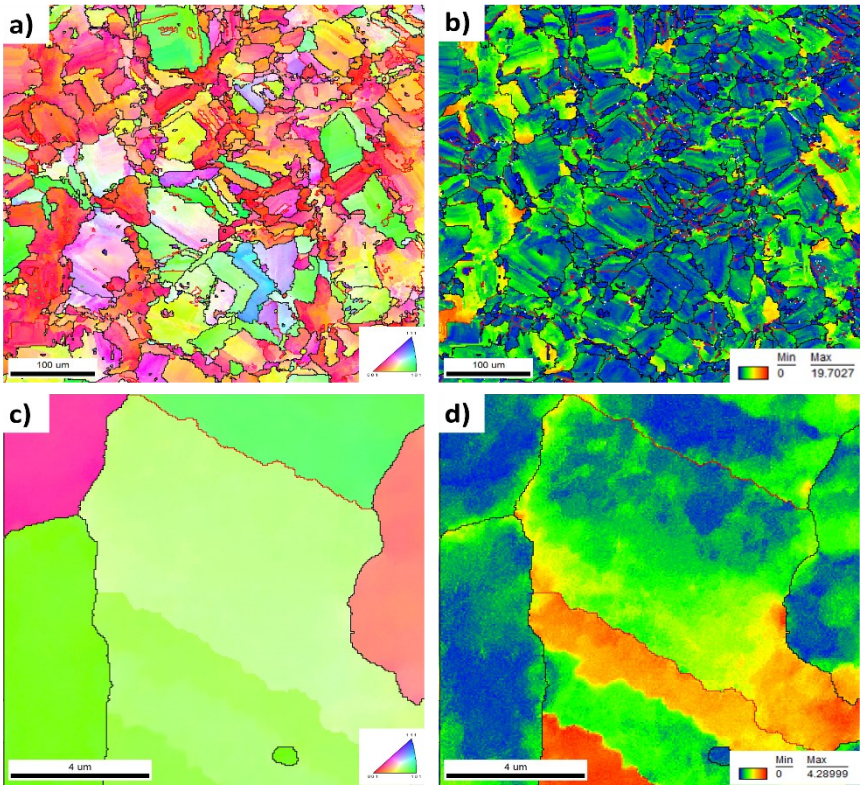

Figure 3-26. IPF (left) and GROD (right) maps of scans 1 (a and b) and 2 (c and d). Linear dislocation structures are noticeable in both scans and shown in detail in scan 2, where the maximum misorientation from grain average orientation is 4°.

The GROD map shows regions of relative misorientation separated by the organized dislocation dense LAGBs for each scan. The linear dislocation structures are observed in all three representations of the microstructure, and often separate cells of 1-2° misorientation.

The parallel, GND depleted cells contained by dislocation rich boundaries seen in figure 2 are characteristic of rapid thermal processes that lead to non-equilibrium microstructures and have been theorized to be a mechanism to minimize stored strain energy [41].

Elastic Strain and Dislocation Substructures

The elastic strain results from scan 1 are shown in figure 3-4. The implementation of remapping with a 10° rotation tolerance shows strain values ranging from 0-60% with a mean

± standard deviation of .009±.024, indicative of the distribution shown in the histogram in fig 5a which demonstrates that the majority of values are below 4%. Using a 2° tolerance without remapping results in the same range of calculated elastic strain (.011±.025), but with a slightly lower fraction below 4%. The increased fraction of higher strain values in figure 5b is due to the up to 2° misorientation between reference pattern and experimental pattern, which was not remapped in this data set.

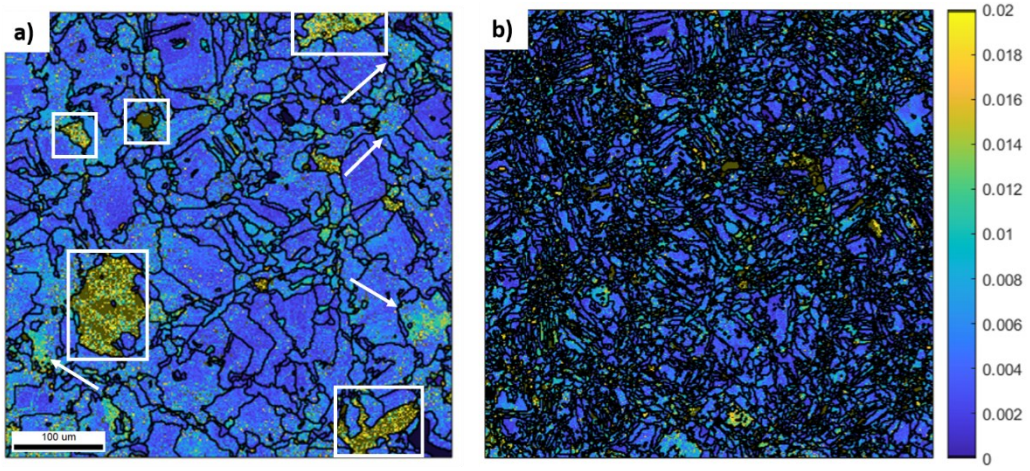

Figure 3-27. Equivalent elastic strain of scan 1 implementing remapping and a rotation tolerance of 10° (a; black boundaries show 10° grain boundaries) and using a 2° rotation tolerance in the absence of remapping (b; black boundaries show 2° subregion

The regions containing dislocation bound cells exhibit low strains in both analyses. Figure 3-4a shows grains with increased relative strain variations (white arrows) which correlate with intragranular regions showing few linear dislocation structures in figure 3-2 (black arrows). While the stochasticity of mechanical properties in crystalline materials at the small scale is an intense area of research, it is still difficult to specify a plasticity limit at the microscale due to effects of various microstructural features [42]. A sub-grain crystal plasticity finite element model and single crystal experiments of Ni based superalloys found that plastic yield begins

around 1% strain [43,44], while a recent unsupervised learning experiment found a yield point of .003 macroscopic strain in DMLS processed IN625 [34]. Here, some grains resulted in particularly high elastic strain (boxes in figure 3-4a), the average values of which exceed 1%. These high values are thought to be due to selection of poor-quality reference patterns and the strain variations in these grains are not, at this point, reliable.

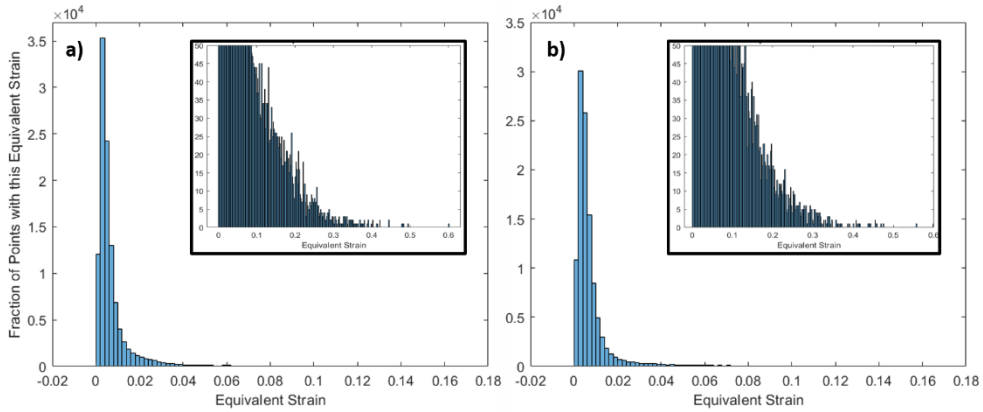

Figure 3-28. Distribution of calculated strain in scan 1 using remapping and a 10° rotation tolerance (a) and a 2° rotation tolerance with no remapping (b)

Figures 6 and 7 show the elastic strain distribution of scan 2, which resulted in overall decreased strain values (.007±.008 with remapping and .008±.005 without remapping). Many of these strain values still exceed the plasticity limit and therefore are considered to be overestimations. Misorientations as small as 2° between reference and experimental pattern have been shown to result in overestimation of elastic strain [39], as can be seen in figure 6b where the cells bound by dislocation dense LAGBs show higher strain without remapping than they do when remapping is implemented. Figure 7a demonstrates that remapping patterns results in decreased calculated equivalent elastic strain and a smaller portion of strain values exceeding the slip limit of dislocation pile-ups. Additionally, use of remapping allows calculation

of relative strain over a larger subsection, in the case of scan 2 an entire grain, and allows observation of strain gradients between dislocation structures.

The grain observed in scan 2 contains a dislocation cell structure previously discussed and it is observed using remapping that the interior of this cell contains low elastic strain values. However, the cell boundaries which were shown in figure 2 to be around 2° show higher elastic strain values. This result makes sense as we would expect a region dense in dislocations to have more highly distorted diffraction patterns than the interior of the cell with a lower dislocation density.

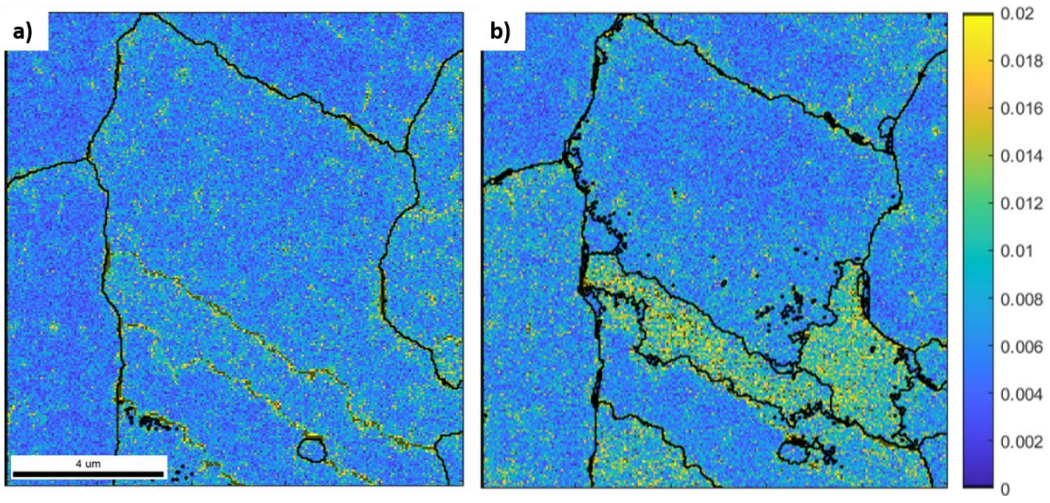

Figure 3-29. Calculated elastic strain in scan 2 using remapping and a 4° rotation tolerance (a; black boundaries are 4°) and a 2° rotation tolerance with no remapping (b; black boundaries are 2°). Color scale values are in equivalent strain measured.

Using a rotation tolerance alone may result in accurately characterized elastic strain, but the implementation of remapping increases the fraction of elastic strain below the slip transfer limit (figures 5 and 7). Additionally, the need to use a small rotation tolerance in the absence of remapping decreases the area of investigation and does not allow relative strain calculations between cell structures.

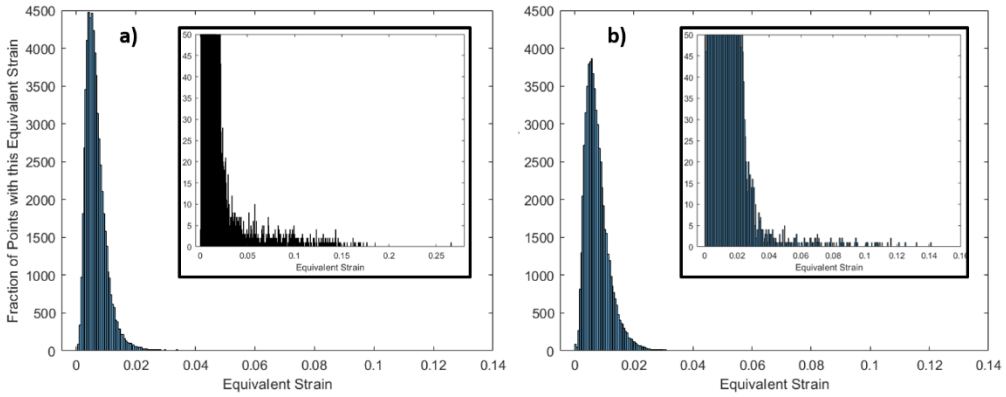

Figure 3-30. Distribution of calculated elastic strain in scan 2 with implementation of remapping and a 4° rotation tolerance (a) and with a 2° rotation tolerance without remapping (b)

Discussion

GND Density and Dislocation Substructures

The microstructure of DMLS fabricated IN625 discussed here exhibits cell structures separated by linear boundaries of high dislocation density, some of which run the entire width of the grain in which they are contained. The high density of dislocations is known to originate from the thermal processing occurring during DMLS [45,46]. Intragranular cell structures have been previously observed in laser AM processed alloys in uniform geometry and as a product of chemical segregation during the fabrication process [22,23,47]. These metastable structures are separated by ~200nm wide LAGBs and have been shown to decompose with annealing. Additionally, cell structures similar to the ones shown here have been observed in DMLS processed Inconel alloys [21,45]. High dislocation densities have been observed in laser AM fabricated Ni superalloys forming dendritic subgrains due to the thermal stress production during melt solidification processing[21,45].

The repetitive thermal cycles of DMLS are known to complicate the already complex thermal history of the process [48]; however, the movement of dislocations and formation of subgrains throughout a DMLS component are still little understood. The depth of the analyzed area in many previous microstructural studies on Inconel alloys produced by laser additive techniques is unreported; however, the direction changing dendritic microstructure found near the top surface by Zhao et al. demonstrates that the microstructure in these alloys is indeed depth dependent [49–51]. While more specific thermal gradient data is necessary to fully understand the dislocation structure evolution with processing, we demonstrate in this study that at a build depth of 5mm, the typical RS microstructure present after laser additive processing has evolved into a more equiaxed grain structure containing organized dislocation cell structures similar to dendritic subgrains found previously. Our results suggest microstructural evolution of previously deposited layers during laser processing due to repetitive laser exposure and the presence of the HAZ.

Laser tracking over a virgin powder layer re-melts previously melted layer(s), reintroducing high thermal gradients and fast cooling rates in the molten pool and HAZ, the depths of which are highly dependent on laser parameters [50]. Previous simulations have estimated the depth of the molten pool itself to be ~750µm, thicker than the typical powder layers used in DMLS manufacturing (~20-80µm), meaning a single layer may be re-melted ~10 times before moving into the range of the HAZ and finally out of reach of extreme thermal gradients induced by the laser [17,50]. The temperatures introduced by the laser on previously melted layers are generally still above the liquidus temperature and the HAZ induces temperatures high enough to cause grain growth [50]. It is these phenomena that introduce thermal stresses which are

responsible for the static recrystallization undergone by DMLS fabricated Ni superalloys during post processing [51]. The correlation between dislocation motion and stress release in AM metals has been studied on the grain level during mechanical deformation with HEDM and unsupervised learning [34]. However, microstructural evolution *during* DMLS processing is little understood. The dislocation structures shown in this study are similar to those seen in Yoo, et al.[21] and are thought to be mechanisms of strain minimization; figure 6a supports this theory, showing low relative strain between cell structure separated by high GND density boundaries. Thus, the thermal strains induced during a single laser pass may drive dislocation motion in subsequent laser and HAZ passes, resulting in unique recrystallization mechanisms forming subgrain and grain boundaries during fabrication.

Elastic Strain

Thermally induced strains are produced on the bulk and microscales in many fabrication techniques with sufficiently high thermal gradients; quenching of a component will result in tensile strain on the surface and a layer of compressive strain in the interior due to the outer surface cooling and contracting while the bulk of the material is still warm and expansive. [52,53] Elastic strains on the intragranular scale such as those measured here are normally a result of the stress fields of dislocations or coherency at interfaces. [53] It has been found previously that these dislocation substructures have associated long-range internal stresses in the presence and absence of dislocation pile-ups.[41] Due to the highly localized thermal gradients induced by the laser in DMLS, microscale elastic strains may be affected by a combination of temperature, dislocation substructure, and interfaces during solidification. These parameters may also affect the subsequent microstructural evolution during post-

processing which DMLS components often undergo, resulting in altered mechanical and material properties. [54,55] Here we outline a method by which the little understood nature of the relationship between dislocation substructure evolution and intragranular elastic strain distribution can be investigated in order to understand the evolution of residual stresses and their effects on final components. [41,56]

While the introduction of residual strain during DMLS is known to be caused by the thermal environment, there is a lack of understanding surrounding its role in microstructural evolution [32,57–61]. The elastic strain results shown here demonstrate low strain variation between cell structures bound by dislocation dense LAGBs, while some grains without cell structures exhibit higher variations of elastic strain. The extent to which thermal elastic strain drives formation of cell structures or boundary migration during AM process is little understood; finite element simulations have demonstrated that the level of residual strain in AM parts varies with depth and distance from the melt pool [62–64]. High stresses are found at the top of the build and nearer to the center of the laser track, locations where the highest thermal gradients and fastest solidification occurs. Additionally, cellular automata simulations have predicted the development of cell structures such as those seen here [65,66]. We show elastic strain variations on the microscale which correlate to the presence of dislocation bound subgrains; low elastic strain within the subgrains, and higher strain values (and variations) in regions and grains without subgrains, suggesting the formation of subgrains is indeed driven by elastic strain energy. The high values of elastic strain shown at dislocation dense boundaries are effects of lower quality diffraction patterns at these points and are not evidence of high elastic strain at cell boundaries. Rather, these poor-quality patterns support the high dislocation

densities found using the Nye tensor analysis at these locations, as plastically deformed lattices containing high dislocation densities result in low quality diffraction patterns.

The cross-correlation process for elastic strain calculation using EBSD patterns has been described elsewhere, as has the remapping method used here [26,39]. However, further subdivision in this analysis is necessary to result in strain values below the plasticity limit across sub-regions of similar misorientation. When dividing the grains into sub-regions to reduce the strain to reasonable levels, a new reference pattern must be selected for each new division. The OpenXY algorithm used here has two methods of choosing reference patterns: it can attempt to pick the point with an orientation closest to the mean orientation of the entire sub-region, or it can attempt to pick the pattern with the highest image quality. Here, we used the former method which generally produces better results; however, it may also result in selecting a pattern with poor image quality. Because of this, some entire sub-divisions will have disproportionately high strains relative to those around them, as mentioned in the results section and can be seen clearly in figure 4. A more robust method of selecting reference points that attempts to compromise between the two could possibly resolve this. Additionally, a more robust method of assessing the quality of the cross-correlation could allow us to flag points that have an erroneous strain due to poor reference pattern selection. While figure 7 shows the occurrence of elastic strain values higher than the 1% yield mentioned previously, these outliers may be explained by experimental patterns of poor quality. However, in scan 2 it is not considered that the reference pattern itself is of poor quality, as most strain values are less than 1%. Here, we have demonstrated that the remapping method is necessary to observe

strain localization in the presence of substructures, because the use of a low rotation tolerance results in the loss of continual relative strain maps across substructure boundaries.

We are unable to fully account for the changes in the stress state of the material brought about by grinding and polishing in preparation for EBSD. Little is known about the effect of these techniques on the microscale elastic strain state of the material; Everaerts, Salvati, and Korsunsky [67] used a focused ion beam – digital image correlation (FIB-DIC) technique in Ti-6Al-4V to measure plastic deformation induced by different polishing slurries and found that colloidal silica resulted in no appreciable deformation. However, in our polishing technique silica was used after other diamond polishing slurries and therefore it is possible that some plastic deformation remains on the surface of our material.

Future experiments using known thermal gradient data in conjunction with microstructural simulations will result in deeper understanding of the extent to which strain minimization mechanisms are effective at shallower build depths where the material is not exposed to as many repeated laser tracks. Serial sectioning of single tracks of additively manufactured metals will provide a unique study on microstructural evolution, enabling researchers to travel through the thermal history of the additive process while observing the effect of elastic strain on the evolution of dislocation structures.

Conclusions

- The microstructure of DMLS fabricated IN625 contains intragranular dislocation structures with low elastic strain variation at 5mm build depth. Mechanisms of the evolution of

dislocation structures during repetitive laser tracking and material addition are still largely unknown.

- Dislocation cell structures which had been observed in similar materials were seen here to exhibit decreased elastic strain variations within regions enclosed by dislocation rich boundaries, supporting the claim that these cells are strain minimization mechanisms during solidification processing.
- Grains and intragranular regions without dislocation substructures exhibited higher elastic strain content than shown within linear dislocation substructures, suggesting elastic strain influence on microstructural features during AM solidification.
- The results provide a foundation for future experiments using HR-EBSD in conjunction with thermal models to further the understanding of thermal stress and dislocation substructure interaction during AM fabrication.

Acknowledgements

The BYU team was supported by US Department of Energy (DOE), Office of Science, Basic Energy Sciences (BES), under award No. DE-SC0012587.

S. Primig acknowledges funding by the Australian Research Council DECRA (DE180100440) under UNSW Scientia Fellowship schemes.

The authors would like to acknowledge Ryan Carpenter, Matthew Clemente and Elias Jelis at Army ARDEC for fabrication of DMLS samples under Cooperative Research and Development Agreement CRA1706.

References

[1] D. Manfredi, F. Calignano, M. Krishnan, R. Canali, E.P. Ambrosio, S. Biamino, D. Ugues, M. Pavese, P. Fino, Additive Manufacturing of Al Alloys and Aluminium Matrix Composites (AMCs), (n.d.) 3–34. https://doi.org/10.5772/58534.

[2] R. Liu, Z. Wang, T. Sparks, F. Liou, J. Newkirk, Aerospace applications of laser additive manufacturing, in: Laser Addit. Manuf. Mater. Des. Technol. Appl., Elsevier Inc., 2017: pp. 351–371. https://doi.org/10.1016/B978-0-08-100433-3.00013-0.

[3] S. Anandan, R.M. Hussein, M. Spratt, J. Newkirk, K. Chandrashekhara, H. Misak, M. Walker, Failure In metal honeycombs manufactured by selective laser melting of 304 L stainless steel under compression, Virtual Phys. Prototyp. 14 (2019) 114–122. https://doi.org/10.1080/17452759.2018.1531336.

[4] S. Singh, S. Ramakrishna, Biomedical applications of additive manufacturing: Present and future, Curr. Opin. Biomed. Eng. 2 (2017) 105–115. https://doi.org/10.1016/j.cobme.2017.05.006.

[5] Y.-L. Hao, S.-J. Li, R. Yang, Biomedical titanium alloys and their additive manufacturing, Rare Met. 35 (2016) 661–671. https://doi.org/10.1007/s12598-016-0793-5.

[6] F. Liu, X. Lin, C. Huang, M. Song, G. Yang, J. Chen, W. Huang, The effect of laser scanning path on microstructures and mechanical properties of laser solid formed nickel-base superalloy Inconel 718, J. Alloys Compd. 509 (2011) 4505–4509. https://doi.org/10.1016/j.jallcom.2010.11.176.

[7] Z. Wang, T.A. Palmer, A.M. Beese, Effect of processing parameters on microstructure and tensile properties of austenitic stainless steel 304L made by directed energy deposition additive manufacturing, Acta Mater. 110 (2016) 226–235. https://doi.org/10.1016/j.actamat.2016.03.019.

[8] K.N. Amato, J. Hernandez, L.E. Murr, E. Martinez, S.M. Gaytan, P.W. Shindo, S. Collins, Comparison of Microstructures and Properties for a Ni-Base Superalloy (Alloy 625) Fabricated by Electron and Laser Beam Melting, J. Mater. Sci. Res. 1 (2012). https://doi.org/10.5539/jmsr.v1n2p3.

[9] H. Pohl, A. Simchi, M. Issa, H.C. Dias, Thermal stresses in direct metal laser sintering, Proc. SFF Symp. (2001) 366–372. http://edge.rit.edu/edge/P10551/public/SFF/SFF 2001 Proceedings/2001 SFF Papers/41-Pohl.pdf.

[10] R. Shi, S.A. Khairallah, T.T. Roehling, T.W. Heo, J.T. McKeown, M.J. Matthews, Microstructural control in metal laser powder bed fusion additive manufacturing using laser beam shaping strategy, Acta Mater. 184 (2020) 284–305. https://doi.org/10.1016/j.actamat.2019.11.053.

[11] L. Parry, I.A. Ashcroft, R.D. Wildman, Understanding the effect of laser scan strategy on residual stress in selective laser melting through thermo-mechanical simulation, Addit. Manuf. 12 (2016) 1–15. https://doi.org/10.1016/j.addma.2016.05.014.

[12] P. Edwards, M. Ramulu, Fatigue performance evaluation of selective laser melted Ti–6Al–4V, Mater. Sci. Eng. A. 598 (2014) 327–337. https://doi.org/10.1016/j.msea.2014.01.041.

[13] A. Hussein, L. Hao, C. Yan, R. Everson, P. Young, Advanced lattice support structures for metal additive manufacturing, J. Mater. Process. Technol. 213 (2013) 1019–1026. https://doi.org/10.1016/j.jmatprotec.2013.01.020.

[14] J.D. Roehling, W.L. Smith, T.T. Roehling, B. Vrancken, G.M. Guss, J.T. McKeown, M.R. Hill, M.J. Matthews, Reducing residual stress by selective large-area diode surface heating during laser powder bed fusion additive manufacturing, Addit. Manuf. 28 (2019) 228–235. https://doi.org/10.1016/j.addma.2019.05.009.

[15] E. Yasa, J.P. Kruth, J. Deckers, Manufacturing by combining Selective Laser Melting and Selective Laser Erosion/laser re-melting, CIRP Ann. - Manuf. Technol. 60 (2011) 263–266. https://doi.org/10.1016/j.cirp.2011.03.063.

[16] E.J. Lavernia, T.S. Srivatsan, The rapid solidification processing of materials: science, principles, technology, advances, and applications, J. Mater. Sci. 45 (2010) 287–325. https://doi.org/10.1007/s10853-009-3995-5.

[17] D. Gu, L. Du, D. Dai, K. Lin, M. Xia, S. Li, J. He, Influence of thermal behavior along deposition direction on microstructure and microhardness of laser melting deposited metallic parts, Appl. Phys. A. 125 (2019) 455. https://doi.org/10.1007/s00339-019-2745-z.

[18] P.K. Gokuldoss, S. Kolla, J. Eckert, Additive Manufacturing Processes: Selective Laser Melting, Electron Beam Melting and Binder Jetting-Selection Guidelines, Materials (Basel). 10 (2017). https://doi.org/10.3390/ma10060672.

[19] P. Mercelis, J.-P. Kruth, Residual stresses in selective laser sintering and selective laser melting, Rapid Prototyp. J. 12 (2006) 254–265. https://doi.org/10.1108/13552540610707013.

[20] R.J. Moat, A.J. Pinkerton, L. Li, P.J. Withers, M. Preuss, Residual stresses in laser direct metal deposited Waspaloy, Mater. Sci. Eng. A. (2011). https://doi.org/10.1016/j.msea.2010.12.010.

[21] Y.S.J. Yoo, T.A. Book, M.D. Sangid, J. Kacher, Identifying strain localization and dislocation processes in fatigued Inconel 718 manufactured from selective laser melting, Mater. Sci. Eng. A. 724 (2018) 444–451. https://doi.org/10.1016/j.msea.2018.03.127.

[22] K.G. Prashanth, J. Eckert, Formation of metastable cellular microstructures in selective laser melted alloys, J. Alloys Compd. 707 (2017) 27–34. https://doi.org/10.1016/j.jallcom.2016.12.209.

[23] A.J. Birnbaum, J.C. Steuben, E.J. Barrick, A.P. Iliopoulos, J.G. Michopoulos, Intrinsic strain aging, Σ3 boundaries, and origins of cellular substructure in additively manufactured 316L, Addit. Manuf. 29 (2019). https://doi.org/10.1016/j.addma.2019.100784.

[24] T. Vilaro, C. Colin, J.D. Bartout, L. Nazé, M. Sennour, Microstructural and mechanical approaches of the selective laser melting process applied to a nickel-base superalloy, Mater. Sci. Eng. A. 534 (2012) 446–451. https://doi.org/10.1016/j.msea.2011.11.092.

[25] K. Chatterjee, A.J. Beaudoin, D.C. Pagan, P.A. Shade, H.T. Philipp, M.W. Tate, S.M. Gruner, P. Kenesei, J. Park, Intermittent plasticity in individual grains: A study using high energy x-ray diffraction, Struct. Dyn. 6 (2019) 14501. https://doi.org/10.1063/1.5068756.

[26] A.J. Wilkinson, G. Meaden, D.J. Dingley, High resolution mapping of strains and rotations using electron backscatter diffraction, Mater. Sci. Technol. 22 (2006) 1271–1278. https://doi.org/10.1179/174328406X130966.

[27] P.F. Rottmann, K.J. Hemker, Nanoscale elastic strain mapping of polycrystalline materials, Mater. Res. Lett. 6 (2018) 249–254. https://doi.org/10.1080/21663831.2018.1436609.

[28] E.A. Lass, M.R. Stoudt, M.E. Williams, M.B. Katz, L.E. Levine, T.Q. Phan, T.H. Gnaeupel-Herold, D.S. Ng, Formation of the Ni3Nb δ-Phase in Stress-Relieved Inconel 625 Produced via Laser Powder-Bed Fusion Additive Manufacturing, Metall. Mater. Trans. A Phys. Metall. Mater. Sci. 48 (2017) 5547–5558. https://doi.org/10.1007/s11661-017-4304-6.

[29] D.R. Haeffner, J.D. Almer, U. Lienert, The use of high energy X-rays from the Advanced Photon Source to study stresses in materials, 399 (2005) 120–127. https://doi.org/10.1016/j.msea.2005.02.023.

[30] X. Wang, K. Chou, Residual Stress in Metal Parts Produced by Powder-Bed Additive Manufacturing Processes, Igarss 2014. (2014) 1–5. https://doi.org/10.1007/s13398-014-0173-7.2.

[31] R. Cottam, J. Wang, V. Luzin, Characterization of microstructure and residual stress in a 3D H13 tool steel component produced by additive manufacturing, (n.d.). https://doi.org/10.1557/jmr.2014.190.

[32] Z. Wang, E. Denlinger, P. Michaleris, A.D. Stoica, D. Ma, A.M. Beese, Residual stress mapping in Inconel 625 fabricated through additive manufacturing: Method for neutron diffraction measurements to validate thermomechanical model predictions, Mater. Des. 113 (2017) 169–177. https://doi.org/10.1016/j.matdes.2016.10.003.

[33] K. Chatterjee, A. Venkataraman, T. Garbaciak, J. Rotella, M.D. Sangid, A.J. Beaudoin, P. Kenesei, J.S. Park, A.L. Pilchak, Study of grain-level deformation and residual stresses in Ti-7Al under combined bending and tension using high energy diffraction microscopy (HEDM), Int. J. Solids Struct. 94–95 (2016) 35–49. https://doi.org/10.1016/j.ijsolstr.2016.05.010.

[34] D.C. Pagan, T.Q. Phan, J.S. Weaver, A.R. Benson, A.J. Beaudoin, Unsupervised learning of dislocation motion, Acta Mater. 181 (2019) 510–518. https://doi.org/10.1016/j.actamat.2019.10.011.

[35] BYU - OpenXY, (2018). https://github.com/BYU-MicrostructureOfMaterials/OpenXY.

[36] A.C. Leff, C.R. Weinberger, M.L. Taheri, Estimation of dislocation density from precession electron diffraction data using the Nye tensor, Ultramicroscopy. 153 (2015) 9–21. https://doi.org/10.1016/j.ultramic.2015.02.002.

[37] X.X. Yu, A. Gulec, Q. Sherman, K.L. Cwalina, J.R. Scully, J.H. Perepezko, P.W. Voorhees, L.D. Marks, Nonequilibrium Solute Capture in Passivating Oxide Films, Phys. Rev. Lett. 121 (2018) 145701. https://doi.org/10.1103/PhysRevLett.121.145701.

[38] E.J. Schwalbach, S.P. Donegan, M.G. Chapman, K.J. Chaput, M.A. Groeber, A discrete source model of powder bed fusion additive manufacturing thermal history, Addit. Manuf. 25 (2019) 485–498. https://doi.org/10.1016/j.addma.2018.12.004.

[39] T.B. Britton, A.J. Wilkinson, High resolution electron backscatter diffraction measurements of elastic strain variations in the presence of larger lattice rotations, Ultramicroscopy. 114 (2012) 82–95. https://doi.org/10.1016/j.ultramic.2012.01.004.

[40] T. Ben Britton, S. Birosca, M. Preuss, A.J. Wilkinson, Electron backscatter diffraction study of dislocation content of a macrozone in hot-rolled Ti-6Al-4V alloy, Scr. Mater. 62 (2010) 639–642. https://doi.org/10.1016/j.scriptamat.2010.01.010.

[41] H. Mughrabi, Dislocation wall and cell structures and long-range internal stresses in deformed metal crystals, Acta Metall. 31 (1983) 1367–1379. https://ac-els-cdn-com.ezproxy2.library.drexel.edu/000161608390007X/1-s2.0-000161608390007X-main.pdf?_tid=cfff344b-67bf-488c-8a81-05852b1dda3e&acdnat=1543879427_a5f0644736ba21293d3c39300b70ae4b (accessed December 3, 2018).

[42] H. Askari, M.R. Maughan, N. Abdolrahim, D. Sagapuram, D.F. Bahr, H.M. Zbib, A stochastic crystal plasticity framework for deformation of micro-scale polycrystalline materials, Int. J. Plast. 68 (2015) 21–33. https://doi.org/10.1016/j.ijplas.2014.11.001.

[43] S. Keshavarz, S. Ghosh, Hierarchical crystal plasticity FE model for nickel-based superalloys: Sub-grain microstructures to polycrystalline aggregates, Int. J. Solids Struct. 55 (2015) 17–31. https://doi.org/10.1016/j.ijsolstr.2014.03.037.

[44] G. Fleury, F. Schubert, H. Nickel, Modelling of the thermo-mechanical behaviour of the single crystal superalloy CMSX-4, Comput. Mater. Sci. 7 (1996) 187–193. https://doi.org/10.1016/s0927-0256(96)00079-1.

[45] Y.-L. Kuo, S. Horikawa, K. Kakehi, The effect of interdendritic δ phase on the mechanical properties of Alloy 718 built up by additive manufacturing, (2016). https://doi.org/10.1016/j.matdes.2016.12.026.

[46] L.E. Murr, Metallurgy of additive manufacturing: Examples from electron beam melting, Addit. Manuf. 5 (2015) 40–53. https://doi.org/10.1016/j.addma.2014.12.002.

[47] K.G. Prashanth, S. Scudino, H.J. Klauss, K.B. Surreddi, L. Löber, Z. Wang, A.K. Chaubey, U. Kühn, J. Eckert, Microstructure and mechanical properties of Al-12Si produced by selective laser melting: Effect of heat treatment, (2013).

https://doi.org/10.1016/j.msea.2013.10.023.

[48] R. Shi, S. Khairallah, T. Wook Heo, M. Rolchigo, J.T. Mckeown, M.J. Matthews, Integrated Simulation Framework for Additively Manufactured Ti-6Al-4V: Melt Pool Dynamics, Microstructure, Solid-State Phase Transformation, and Microelastic Response, JOM. 71 (2019) 3640–3655. https://doi.org/10.1007/s11837-019-03618-1.

[49] X. Zhao, J. Chen, X. Lin, W. Huang, Study on microstructure and mechanical properties of laser rapid forming Inconel 718, Mater. Sci. Eng. A. 478 (2008) 119–124. https://doi.org/10.1016/j.msea.2007.05.079.

[50] T.M. Rodgers, J.D. Madison, V. Tikare, Simulation of metal additive manufacturing microstructures using kinetic Monte Carlo, Comput. Mater. Sci. 135 (2017) 78–89. https://doi.org/10.1016/j.commatsci.2017.03.053.

[51] J. Cao, F. Liu, X. Lin, C. Huang, J. Chen, W. Huang, Effect of overlap rate on recrystallization behaviors of Laser Solid Formed Inconel 718 superalloy, Opt. Laser Technol. 45 (2013) 228–235. https://doi.org/10.1016/j.optlastec.2012.06.043.

[52] P.J. Withers, Residual stress and its role in failure, Reports Prog. Phys. 70 (2007) 2211–2264. https://doi.org/10.1088/0034-4885/70/12/R04.

[53] P.J. Withers, H.K.D.H. Bhadeshia, P.J. Withers, H.K.D.H. Bhadeshia, Residual stress . Part 1 – Measurement techniques Residual stress Part 1 – Measurement techniques, 0836 (2016). https://doi.org/10.1179/026708301101509980.

[54] B. Farber, K.A. Small, C. Allen, R.J. Causton, A. Nichols, J. Simbolick, M.L. Taheri, Correlation of mechanical properties to microstructure in Metal Laser Sintering Inconel 718, Mater. Sci. Eng. A. 712 (2018) 539–547. https://doi.org/10.1016/j.msea.2017.11.125.

[55] G.A. Rao, M. Kumar, M. Srinivas, D.S. Sarma, Effect of standard heat treatment on the microstructure and mechanical properties of hot isostatically pressed superalloy inconel 718, Mater. Sci. Eng. A. (2003). https://doi.org/10.1016/S0921-5093(03)00079-0.

[56] W. Chen, T. Voisin, Y. Zhang, J.-B. Florien, C.M. Spadaccini, D.L. McDowell, T. Zhu, Y.M. Wang, Microscale residual stresses in additively manufactured stainless steel, Nat. Commun. 10 (2019) 4338. https://doi.org/10.1038/s41467-019-12265-8.

[57] Z. Wang, A.D. Stoica, D. Ma, A.M. Beese, Diffraction and single-crystal elastic constants of Inconel 625 at room and elevated temperatures determined by neutron diffraction, Mater. Sci. Eng. A. 674 (2016) 406–412. https://doi.org/10.1016/j.msea.2016.08.010.

[58] D.W. Brown, J.D. Bernardin, J.S. Carpenter, B. Clausen, D. Spernjak, J.M. Thompson, Neutron diffraction measurements of residual stress in additively manufactured stainless steel, Mater. Sci. Eng. A. 678 (2016) 291–298. https://doi.org/10.1016/j.msea.2016.09.086.

[59] A.S. Tremsin, Y. Gao, L.C. Dial, F. Grazzi, T. Shinohara, Investigation of microstructure in

additive manufactured Inconel 625 by spatially resolved neutron transmission spectroscopy, Sci. Technol. Adv. Mater. 17 (2016) 324–336. https://doi.org/10.1080/14686996.2016.1190261.

[60] I. Yadroitsev, I. Yadroitsava, Evaluation of residual stress in stainless steel 316L and Ti6Al4V samples produced by selective laser melting, Virtual Phys. Prototyp. 10 (2015) 67–76. https://doi.org/10.1080/17452759.2015.1026045.

[61] T.B. Britton, A.J. Wilkinson, Stress fields and geometrically necessary dislocation density distributions near the head of a blocked slip band, Acta Mater. 60 (2012) 5773–5782. https://doi.org/10.1016/j.actamat.2012.07.004.

[62] A. Hussein, L. Hao, C. Yan, R. Everson, Finite element simulation of the temperature and stress fields in single layers built without-support in selective laser melting, Mater. Des. 52 (2013) 638–647. https://doi.org/10.1016/j.matdes.2013.05.070.

[63] C. Li, Y. Wang, H. Zhan, T. Han, B. Han, W. Zhao, Three-dimensional finite element analysis of temperatures and stresses in wide-band laser surface melting processing, Mater. Des. 31 (2010) 3366–3373. https://doi.org/10.1016/j.matdes.2010.01.054.

[64] T. Keller, G. Lindwall, S. Ghosh, L. Ma, B.M. Lane, F. Zhang, U.R. Kattner, E.A. Lass, J.C. Heigel, Y. Idell, M.E. Williams, A.J. Allen, J.E. Guyer, L.E. Levine, Application of finite element, phase-field, and CALPHAD-based methods to additive manufacturing of Ni-based superalloys, Acta Mater. 139 (2017) 244–253. https://doi.org/10.1016/j.actamat.2017.05.003.

[65] M.R. Rolchigo, R. LeSar, Application of alloy solidification theory to cellular automata modeling of near-rapid constrained solidification, Comput. Mater. Sci. 163 (2019) 148–161. https://doi.org/10.1016/j.commatsci.2019.03.012.

[66] M.R. Rolchigo, M.Y. Mendoza, P. Samimi, D.A. Brice, B. Martin, P.C. Collins, R. LeSar, Modeling of Ti-W Solidification Microstructures Under Additive Manufacturing Conditions, Metall. Mater. Trans. A Phys. Metall. Mater. Sci. 48 (2017) 3606–3622. https://doi.org/10.1007/s11661-017-4120-z.

[67] J. Everaerts, E. Salvati, A.M. Korsunsky, Nanoscale Depth Profiling of Residual Stresses Due to Fine Surface Finishing, Adv. Mater. Interfaces. 6 (2019) 1–5. https://doi.org/10.1002/admi.201900947.

Chapter 4. Role of Processing in Microstructural Evolution in Inconel 625: A Comparison of Three Additive Manufacturing Techniques

Introduction

Additive manufacturing (AM), due to its potential for efficient production of complex components [1–5], has garnered much attention in both basic research and manufacturing in fields as diverse as medicine and aerospace engineering. There is strong motivation to design AM parts at the microscale to achieve targeted material properties. Differences in AM processing parameters, such as heating rate and feed material, lead to drastic differences in resulting microstructure and mechanical properties [6–9]. Moreover, AM processes can even yield spatial differences in microstructures due to unique thermal histories at different locations in a single component [10–12]. Benchmarking these variations within processes as well as across AM techniques is critical in order to fully realize the potential of AM for rapid and reliable insertion into application space; one microstructural descriptor that provides a pathway toward benchmarking is elastic strain. Elastic strain is a known obstacle in the AM community, however there is a lack of understanding surrounding its evolution and influence on microstructural defects, including dislocation substructure, or geometrically necessary dislocation (GND) density. The initial dislocation density of Ni superalloys has been previously reported to impact the microstructural evolution during post-processing treatments, for example γ” was found to precipitate preferentially on subgrain boundaries in IN625 and the segregated microstructure of AM IN65 has been shown to influence the kinetics of δ phase formation [13,14] To improve the prediction of microstructures and material properties from AM metals, the quantification of microstructural data towards machine learning (ML) has

become a driving force within the field of AM[15,16]. This paper provides a quantitative comparison of the differences in microstructure and spatial distribution of microscale elastic strain and GND density in Inconel 625 fabricated by three unique AM methods: binder jet 3D printing (BJ3DP), electron beam freeform fabrication (EBF3), and direct metal laser sintering (DMLS).

BJ3DP is an area of great interest for structural alloys due to the absence of a high energy laser or electron beam [2,10], and thus, lacks steep thermal gradients. In BJ3DP a liquid binder is used to selectively bind metal powder together into a desired geometry; the 'green part' is then cured in an oven at near 200°C to strengthen it [17]. The post-curing 'brown part' is sintered in a vacuum furnace to burn off the remaining liquid binder and to increase the density of the final part. The BJ3DP process has the most even thermal gradients and the slowest cooling rate of all three processes studied in this experiment, and it has been shown to result in equiaxed microstructures with little intragranular misorientation in Ni superalloys [7,8]. However, this AM method is highly dependent on the powder size and binder saturation and is often complicated by porosity in final components which can have a detrimental effect on the mechanical properties of the final part and often requires post-processing steps such as hot isostatic pressing (HIP) [18].

Electron beam freeform fabrication (EBF3) is an additive technique developed by NASA Langley Research Center (LRC) in an effort to design a fabrication process free from powder for use in low gravity environments [9,19]. By using a feed material of metal wire and an electron beam, 3D components can be built quickly in a vacuum and with little waste material when compared to conventional manufacturing processes [20,21]. However, wire also leads to less

accurate geometries and therefore EBF3 has been found to be most suitable for large, simple geometries [22]. During EBF3, a high-power stationary electron beam welds metal wire together on a preheated build plate that is mobile in three dimensions. Variations in microstructure have been accomplished by changing the parameters of the EBF3 process, for instance a slow build plate translation results in large grained dendritic microstructures, expected for processes with slow cooling rates [23]. Process maps have been used previously for single bead Ti-6Al-4V fabricated by EBF3, where beam power and plate velocity are used to control melt pool dimensions toward a predicted grain morphology [24].

Direct metal laser sintering (DMLS) is a more commonly used AM process than EBF3 in which a high-powered mobile laser in an inert environment is used to partially melt metal powder into a desired geometry. DMLS results in higher thermal gradients and faster cooling rates than are typical in EBF3 or BJ3DP, usually resulting in smaller grains and potentially undesirable mechanical properties including residual strains [25]. The microstructure resulting from DMLS is highly dependent on melt pool shape and energy density; Agrawal et al. found that at increased energy densities the grain size and aspect ratio increased, and texture was more random in 316L stainless steel [26]. These experiments result in process maps which can be used to design and predict microstructures; however, the dislocation substructures and elastic strain distributions, both of which are important to microstructural evolution and final mechanical properties, have not been investigated to this degree due to the difficulty in their characterization. The residual strains imposed by the DMLS process can be large enough to induce warping in the component after it is released from the build plate and can cause failed tolerances and mechanical failures in the absence of loading [27]. DMLS is a complex process

with a number of processing parameters which could alter the thermal gradients and cooling rates of the manufacturing method; however, this method is more attractive to some than EBF3 in part because DMLS is more precise and results in parts with better manufacturing tolerances [27,28].

Residual strains in AM produced metal parts have been identified as a potentially problematic property and have been investigated thoroughly on the bulk and more local scales using neutron and X-ray diffraction [25,27,29,30]. However, residual strains on these levels are indicative of more meso and microscale residual strains which are a direct product of the complex solidification occurring in many AM methods [31]. Characterization and understanding of these local elastic strains are necessary if the AM community desires to engineer elastic residual strains, on any scale, into or out of their final components. Microscale residual elastic strain is not unique to AM but the thermal environments of these processes make it a significant obstacle in AM compared to conventional processing. Electron backscatter diffraction (EBSD) has recently emerged as a tool for microscale elastic strain characterization and has been used for calculation of elastic strains in AM [32–34]. The quantification of elastic strain distribution in AM materials could improve theories of rapid solidification (RS) mechanisms and engineering of AM processes to produce desired microstructures. Additionally, dislocation substructures on the microscale were recently shown to be related to the presence of strain during solidification [35], emphasizing the importance of thermally induced microscale strains on the resulting mechanical properties of AM components.

Dislocation substructures have been widely observed in DMLS components of various alloys [36–39] and have been investigated for their effects on mechanical and other material

properties including radiation tolerance [40,41]. Linear dislocation structures were previously observed in DMLS IN625 [34] in tandem with elastic strain, where it was seen that low elastic strain was largely contained by the dislocation substructure network. Dislocation substructures have also been seen in powder bed electron beam melting (EBM) [42], however, they have not been reported to this date in EBF3 or BJ3DP. This disparity in the presence of dislocation substructures is due to the difference in thermal environment between AM techniques. DMLS and EBF3 are both methods of AM with intense thermal gradients and repetitive heating cycles at high temperatures which can lead to RS, while BJ3DP does not include such fast solidification mechanisms or violent heating environments. The presence of dislocation cells in laser AM 316L is sometimes accompanied by solute microsegregation, however the mechanical properties of this alloy have been shown to have increased dependence on cell size, rather than the strength of segregation[40]. Void swelling in an as-built DMLS 316L stainless steel under heavy ion irradiation was seen to be twice as high as in the post-processed alloy, which had fewer solidification dislocation substructures[41]. These results highlight the importance of dislocation substructures on the properties and complex evolution of AM alloys, and perhaps more importantly, the need for predictive design of these structures based on key microstructural descriptors.

In order for reliable, predictable properties to be achieved in a design space as expansive as that of AM, microstructural features must be characterized quantitatively. We show that with increasing thermal gradient and solidification rate the IN625 microstructure exhibits higher values of both elastic strain and GND density, as well as significantly varying spatial distributions of these features. Additionally, we demonstrate a novel image analysis

technique which allows the spatial relationship between certain features to be quantified. We show that DMLS, the technique involving highest thermal gradients and fastest solidification rates (with the parameters used in this study) contains a strong spatial relationship between elastic strain and GND density, while BJ3DP exhibits a significantly weaker relationship between these features. In addition to furthering the understanding of AM solidification mechanisms, this method can be used to facilitate the inclusion of microscale strain and GND density into predictive ML frameworks, which have typically excluded these descriptors due to the difficulty in characterization and quantification[43–45]. Further progress can be made by using the techniques shown here to quantify microstructures resulting from more similar thermal environments, such as spatially and temporally varying thermal gradients in a single AM build.

Materials and Methods

Inconel 625 was chosen as the material of interest due to its importance in aerospace and transportation industries, its ability to be used with all three additive techniques, and the absence of harmful secondary phases, such as Laves phase, seen in other Ni alloys. Process parameters of each manufacturing technique are described below. The analysis in this study is done on longitudinal faces of each printed sample.

Binder Jet 3D Printing

Fabrication of BJ3DP parts was performed at Hoeganaes Corporation in Cinnaminson, NJ on an ExOne Innovent printer using polyethylene glycol binder with 100% saturation of each 50µm thick layer of water atomized particles with an average particle diameter of 12.7µm. Drying time between layers was 25 seconds preceded by a binder set time of 5 seconds. The

recoat speed after the drying time was 110mm/sec with roller traverse and rotation speeds of 5mm/sec and 300rpm, respectively. The process was carried out in atmosphere with a building platform temperature of 48°C. Following the binder jet process, the tensile specimens were sintered in a vacuum furnace using the following sintering schedule: ramp at 300.5°C/h to 700°C for 1.5h + ramp at 282.2°C/h to 1000°C + ramp at 42.2°C/h to 1315.5°C for 1h + furnace cool to 10°C for 5h.

Direct Metal Laser Sintering

DMLS parts were produced using an EOS M 270 system in a protective N_2 environment with EOS NickelAlloy IN625 powder which has been optimized for use with this system [26]. 10mm cubes were manufactured with a 195W powered laser, a laser scan speed of 700mm/s and a layer thickness of 20µm. Hatch spacing of 100um and a rotation of 67 degrees between layers was implemented. After sintering, the parts were annealed for stress relief at 870°C for 1h followed by water quenching [46] . The stress relieving step is a manufacturer-recommended process for DMLS printed IN625 components and has been seen to result in delta phase formation in LPBF IN625, however the level of recrystallization has been reported to be very low [47–49]. The fraction of LAGBs seen here is comparable to that found in literature after this heat treatment, and the high dislocation density is higher than conventionally processed IN625, as expected for the LPBF process [49–52].

Table 4-8. EBF3 processing parameters

Accelerating voltage (kV)	40

Beam Focus (µm)	323
Beam Current (mA)	35
Wire Feed Rate (mm/min)	889
Translation Speed (mm/min)	254
Bead Spacing (mm)	2.54
Layer Height (mm)	2.54

Electron Beam Freeform Fabrication

A sample of electron beam freeform fabricated (EBF3) IN625 was manufactured at NASA LRC, using wire with a diameter of .063" (1.6mm) of standard composition. The parameters used for the EBF3 process are listed in Table 1.

Characterization and Statistical Analysis

Investigation of the same alloy from varying techniques allows observation of differences in elastic strain and dislocation density resulting from differences in solidification. Here, we use SEM electron backscatter diffraction (EBSD) data for orientation, elastic strain, and dislocation density analysis. EBSD was carried out on a FEI XL30 ESEM equipped with an EDAX DigiView camera and a Helios NanoLab DualBeam using an EDAX Velocity camera with 1x1 binning and a step size of 1.5µm Kikuchi patterns of each scan were collected for analysis with OpenXY [53].

Elastic strain calculation was carried out using a method previously described by Small, et al. [34] in which Kikuchi patterns which are misoriented from the reference pattern are rotated to a similar orientation in a method known as remapping [54]. Additionally, a rotation tolerance is implemented when necessary to ensure misorientations of higher than 10° were not affecting

the strain calculation. BJ3DP and EBF3 did not result in high intragranular misorientation, and so a rotation tolerance was not used in these cases; DMLS, however, resulted in a maximum intragranular misorientation of 25.5° and therefore a rotation tolerance of 10° is implemented. Dislocation density analysis was performed using the Nye tensor lower bound calculation described by Leff, Weinberger and Taheri [55] using the lower bound Nye tensor to arrive at GND density. These two analyses were observed in tandem for any dislocation substructures which may be impacted by the elastic strain present due to thermal gradients.

Spatial analysis of the strain and GND density values was performed using a Fiji/ImageJ plugin MosaicIA [56]. The MosaicIA plugin uses two spatial distributions of objects, here binaries of elastic strain and GND density values, to compute probability density functions (PDFs) of the nearest neighbor (NN) distances between an elastic strain 'object' and a GND density 'object', while also computing the PDF of a random distribution where elastic strain is independently distributed in relation to the observed GND density. To focus on increased elastic strain and GND density distribution, binary images were used which include values above the 75^{th} percentile found in the strain and GND density maps (Figure 4-4). Because the MosaicIA plugin requires binary images, only features which can be characterized as 'high' and 'low' are reasonable to include. For example, an analysis of the spatial relationship between GND density and orientation would not be reasonable for this method because orientation is not a binary characteristic. Other methods have been successful in correlating microstructural features and material properties using convolutional neural networks (CNNs) and 2-point spatial correlations, while orientation binning has used generalized spherical harmonics (GSH) to result in efficient representation of structure-property linkages in simulated microstructures

[57–60]Here, we focus exclusively on elastic strain and GND density because of their importance in material properties and the lack of understanding surrounding their evolution. A Kolmogornov-Smirnov test, which tests the equality of two sample probability distributions, was used to determine whether the observed distributions were significantly different to the independent distributions, as well as to compare the distributions between AM techniques.

Results

The microstructures resulting from each of the three AM techniques are shown using inverse pole figure (IPF) maps (Figure 1). Variations in grain structure and size are immediately noticeable, with BJ3DP exhibiting a more equiaxed, random microstructure than either EBF3 or DMLS. A somewhat elongated grain morphology with wavy GBs is shown to result from EBF3, while a more elongated and textured microstructure results from DMLS. BJ3DP results in a grain morphology not unlike that of cast or wrought IN625 in which recrystallization has been allowed to occur slowly during heat treatment. Indeed, binder jet is the only fabrication method investigated here in which FCC recrystallization twins are seen (green boundaries in Fig 1a). Grain morphology in each AM method varies widely, with the EBF3 microstructure displaying wavy boundaries and a wide range of grain sizes and DMLS exhibiting the columnar grain morphology commonly seen in AM components. The average grain diameter of the BJ3DP sample is 32.8µm, more than 150% of the average horizontal grain diameter in the DMLS and EBF3 samples (11.8µm and 19.5µm, respectively). Importantly, each sample proved fully dense with porosity being unobserved. The nonindexed areas in the BJ3DP sample, first thought to be pores, contain increased chromium and oxygen, most likely Cr_2O_3 precipitates which have been previously found to form in IN625 at temperatures below 1300°K in the first 150 minutes of

heating and in BJ3DP produced IN625 [7]. Neither DMLS nor EBF3 fabricated samples show such precipitates, but contain noticeable intragranular misorientation, shown by color changes within single grains. DMLS resulted in the most intragranular misorientation with an average of 4° from average grain orientation, while binder jet resulted in .36° and EBF3 in .72° variation from grain average. Additionally, DMLS was found to have a higher fraction of low angle grain boundaries (LAGBs, 2-15°)(18%) than either BJ3DP (3%) or EBF3 (12%) .

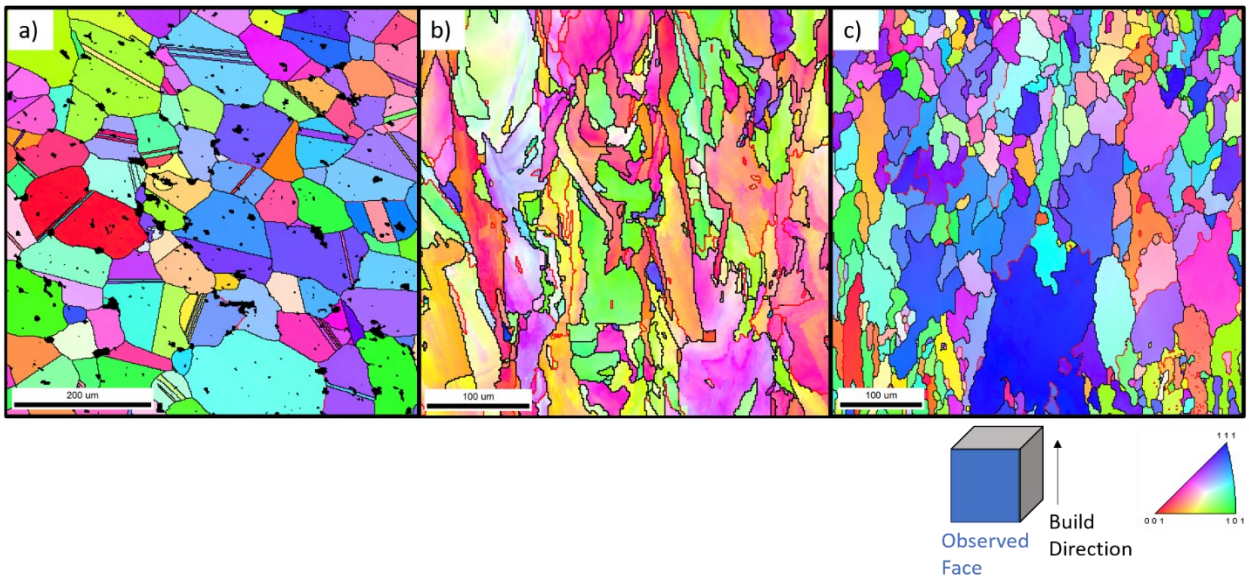

Figure 4-31. IPF maps with respect to build direction of a) BJ3DP, b) EBF3, and c) DMLS fabricated IN625. Differences in grain structure are immediately observable. Twin boundaries are only present after BJ3DP.

Dislocation densities and associated dislocation substructure was explored using the data generated by EBSD. GND density maps and average GND densities were calculated using the lower bound Nye tensor in each sample is shown in Figure 2[55]. BJ3DP results in the lowest GND density while DMLS fabrication results in the highest, nearly an order of magnitude higher than either binder jet or EBF3. With the exception of increased GND density surrounding oxides, BJ3DP resulted in consistently low densities throughout the scan. DMLS and EBF3 each

show varied levels of dislocation organization. The inset in figure 2b indicate areas where high dislocation density is observed to separate differences in orientation, forming very low angle grain boundaries within grains while the inset in figure 2c show regions of intragranular misorientation which are not accompanied by such linear organization of dislocations in DMLS, though still contain high GND density values. This is not unexpected, as Bertsch, et al. showed that dislocation substructures do not always cause intragranular misorientation in laser AM 316L[35].

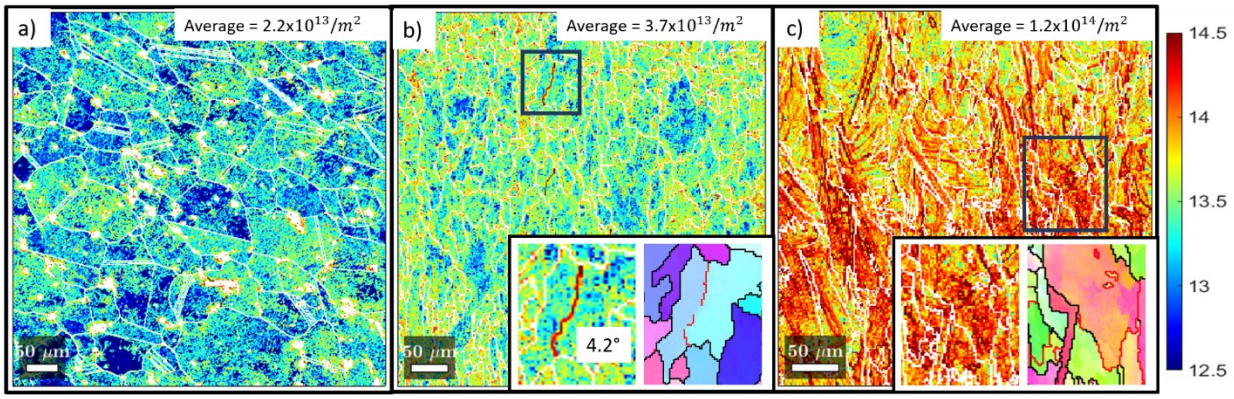

Figure 4-32. GND density of a) BJ3DP, b) EBF3, and c) DMLS fabricated IN625. DMLS has highest GND density, followed by EBF3 and then BJ3DP. Insets show GND density (left) and IPF orientations (right) where regions of intragranular misorientation coincide with regions of high GND density. White lines are grain boundaries 2-65°. Color scale is in $10^x/m^2$.

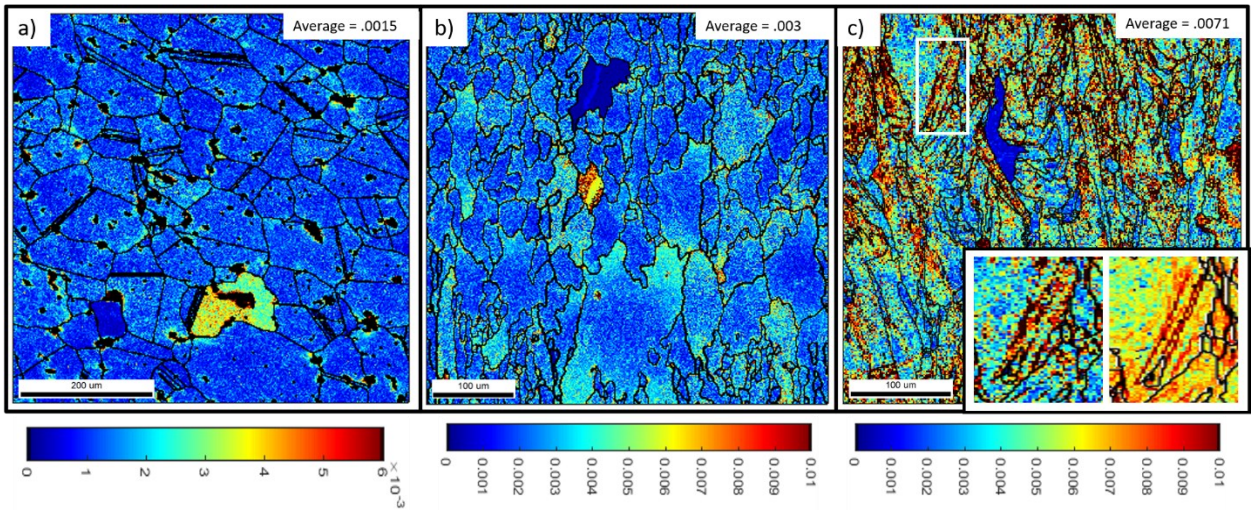

Figure 4-33. Effective elastic strain maps of a) BJ3DP, b) EBF3, and c) DMLS fabricated IN625. DMLS results in highest elastic strain values by far, followed by EBF3 and then BJ3DP. Inset shows strain (left) and GND density (right) in a region where noticeable linear dislocation substructures coincide with high levels of elastic strain. Color scales are in units of strain.

Results of elastic strain analysis, performed using the OpenXY cross-correlation algorithm [53], are shown in figure 3. The nature of the cross-correlation technique may result in overestimation of apparent strain due to misorientation between compared points, however, high misorientation is also an indicator of high GND density. In order to detangle the distortion of EBSD patterns from their misorientation, and therefore elastic strain calculation from GND density estimation, the elastic strain calculation used here implements a rotation tolerance introduced in our previous work in an effort to prohibit misorientation from dominating the strain measurement [34]. The reference point for cross-correlation analysis must be chosen carefully, as a point which is highly misoriented from its grain or one that is of low image quality will give extraneously high strain values which may not be reliable [32]. In this analysis, reference points were chosen to be those closest to the average grain orientation in both DMLS and EBF3, while a reference point based on high image quality (IQ) and confidence index (CI)

was chosen for the BJ3DP scan. This is because the point of reference closest to the average grain misorientation in the BJ3DP scan is of poor quality in many grains and resulted in high apparent strain throughout those regions. Elastic strain in the BJ3DP sample is the lowest, with two grains in the scan showing elevated elastic strain of ~.4%. Though variations in crystal structure on a local scale make it difficult to predict the level of elastic strain accommodation on the microscale, this is within theorized limits for accommodation within the IN625 matrix [61,62]. The two grains with increased elastic strain are separated by the largest oxide (48um by length) and by one of the only LAGBs in the scan area. The average strain in the EBF3 scan was calculated to be twice that of the BJ3DP average, with a minimum elastic strain coinciding with one intragranular dislocation dense boundary and maximum elastic strain occurring at the other (figure 3b). This discrepancy may be due to the selection of a poor reference pattern in one or both of these grains, however an intragranular GND dense LAGB may also be a cause for accumulated elastic strain. EBF3, like BJ3DP, does not show a great amount of organized strain concentrations, however, there are noticeable preferences for high elastic strain values in each case. Elastic strain in BJ3DP is seen to cluster around oxides, particularly oxides which formed on grain boundaries, while in EBF3 the elevated strain values are more likely to occur in clouds at the tops and bottoms of grains near the boundaries.

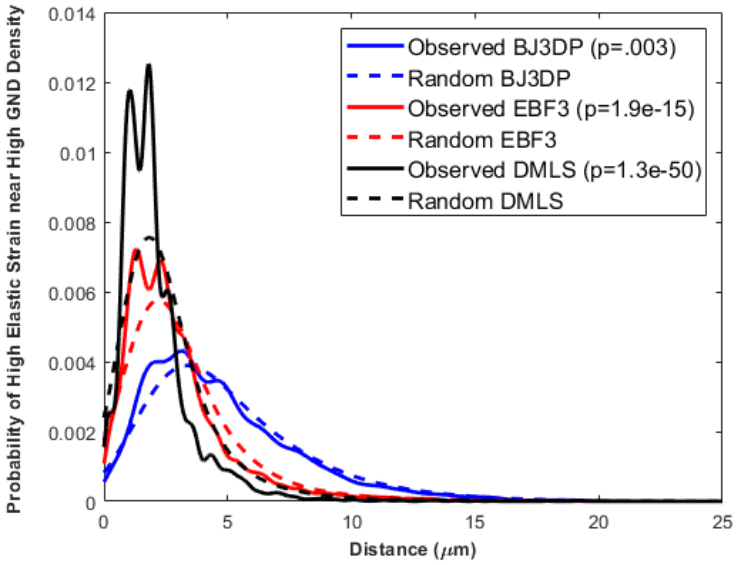

Figure 4-34. PDF of high elastic strain values and their NN distance to high GND density values. p-values in legend show significance of observed probability compared to random probability.

DMLS elastic strain results vary greatly from both other methods and have an average value greater than twice that of EBF3, with a maximum calculated strain value of .19. Two-sample t-tests performed pairwise on normalized elastic strain values from all three samples found significant difference in mean at a confidence level of 99% ($p<.0001$). The distribution of elastic strain in DMLS appears to have some organization which coincides with GND density, shown in the inset in figure 3c where relatively high elastic strain coincides with regions of high dislocation density. While the elastic strain content and distribution in DMLS appear to be connected to GND density more so than in either EBF3 or BJ3DP, statistical analysis is necessary to make reliable quantitative statements.

A probability density function (PDF), resulting from the MosaicIA plugin of the distribution of elastic strain relative to GND density is shown in figure 4-4, where a higher peak

can be said to portray a stronger spatial relationship. Dashed lines show the strength of an independent relationship between the two features, calculated using a theoretical square grid of objects and measuring NN distances from these to high GND density objects. Solid lines show the observed relationship between high elastic strain and GND density, demonstrating the increasing strength of spatial relationship with increasing solidification rate. The strength of the independent relationship increases as well because high GND density values are less clustered throughout the scan in EBF3 and DMLS than in BJ3DP. As shown in figure 4-4, DMLS is nearly twice as likely to have a high elastic strain value within 1-4µm of a high GND density value than EBF3, and three times more likely than BJ3DP. The p-values in figure 4-4 are the significance levels found using a KS test of the observed distributions compared to a random distribution in each AM method, showing that each observed distribution is significantly different than an independent distribution of elastic strain with respect to that method's GND density distribution. The KS test was used to test the significance of the difference between observed distributions in each AM method, finding that each method had a significantly different interaction between GND density and elastic strain compared to each of the others (p-values in table 4-2). By comparing the observed interaction and the independent distribution, we can determine the strength of a proposed relationship between increased elastic strain and GND density values.

Table 4-9. p-values of pairwise KS tests from observed interactions between elastic strain and GND density in each AM method.

Observed Distributions	**KS test p-values**
BJ3DP-EBF3	1.2e-17
EBF3-DMLS	2.0e-19
BJ3DP-DMLS	7.7e-55

Discussion

Previous work has hypothesized that the dislocation substructures present in AM fabricated alloys form as a response to the microscale elastic strain induced by the complex thermal environment of additive techniques[35,38,63]. Our results support this hypothesis and show that a faster solidification rate results in dislocation substructures that are spatially correlated to elastic strain. Our previous work observed the elastic strain and dislocation substructure content at a 5mm depth of a DMLS build in IN625, finding a more linear substructure morphology within grains than seen here.[34] The DMLS results shown here combined with these previous findings support the hypothesis that there is microstructural evolution occurring throughout an AM build in response to the evolving thermal environment. Here, we have used the same method to demonstrate differences between AM techniques with highly varying thermal environments, again supporting substructure evolution hypotheses. The ability to characterize these two features and their spatial relationship provides a greater understanding of solidification mechanisms in extreme thermal environments and provides a pathway to predicting their distribution based on the known thermal environment. ML frameworks which predict material properties based on the spatial variation of microstructures

in AM have gained attention because of their potential to optimize processing parameters for desired mechanical properties [64]. Until now, however, quantified microscale elastic strain and its spatial relationship to GND density under varying thermal gradients, have not been available data to be included in ML frameworks.

The comparative grain structures in BJ3DP, EBF3 and DMLS are to be expected from the thermal environments present in each AM technique. In BJ3DP, supersolidus liquid phase sintering (SLPS) occurs, in which a liquid forms inside the alloyed particle and spreads to particle contacts, causing a viscous flow which leads to grain growth during sintering and a grain structure similar to casting [17,65–67]. EBF3 and DMLS, however, both involve thermal cycles in which the electron beam or laser remelts previously deposited metal layers and causes high temperature melt pools in the component which affect grain growth during processing [68]. The size of these melt pools varies between the two methods; in EBF3 the melt pool has been measured to have a width and depth as high as 3mm in Ti-6Al-4V alloys, while the DMLS melt pool in the same alloys was measured to be 150µm wide and 50µm deep [69]. Additionally, the temperature in the melt pool varies based on beam or laser power and the speed of translation of the laser or the build plate and has been measured to be 2100°C in EBF3 while DMLS melt pools have been measured to be between 2000°-4500°C in Ti-6Al-4V [70,71]. The differences in thermal environment between EBF3 and DMLS explains the variation in grain size between the two techniques. EBF3 has a grain size distribution more similar to BJ3DP than to DMLS (Figure 5) although it has a smaller fraction of grains larger than 1000µm^2 than BJ3DP. DMLS meanwhile, has a distribution of grain sizes that differs from each of the others, with most DMLS grains having an area less than 35µm^2. The fine grain structure found in DMLS is

indicative of the faster cooling rate found in this AM technique with the parameters used in this study.

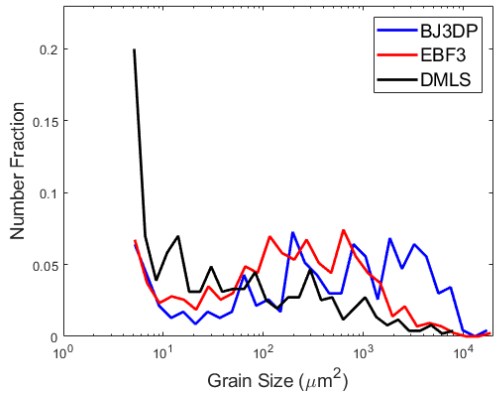

Figure 4-35. Number fraction of grain sizes resulting from AM methods in IN625.

Although AM is an area of intense study, there is still a need for deeper understanding of the solidification mechanisms involved, including the control of stresses and distortion produced during building [4,72]. The dislocation density and elastic strain results found here suggest that BJ3DP, EBF3 and DMLS have significantly different solidification kinetics. This is supported by previous findings; particularly in BJ3DP compared to each of the cyclic thermal processes EBF3 and DMLS. The SLPS process present during BJ3DP does not fully melt the particles, and thermal stresses are not expected to arise during this AM technique [73]. Diffusion in BJ3DP is not suppressed by fast cooling rates, allowing relaxation of elastic strain and dislocation movement during sintering. Indeed, the average residual elastic strain level in BJ3DP here is .15% and regions of elevated elastic strain as well as the highest GND density levels are seen to coincide with the presence of precipitates. Cr_2O_3 precipitates such as those present here are known to form both on surfaces and in the matrix of IN625 at temperatures

approaching 1300°C [7,74]. The spatial analysis of increased GND density and elastic strain in BJ3DP show that, while the observed interaction between the two is significantly different than random (p=.003), the observed and random distributions are more similar to each other than in EBF3 or DMLS, suggesting that the relation between GND density and elastic strain is the weakest in BJ3DP. The presence of a weak interaction between dislocation density and elastic strain can be explained by the presence of Cr_2O_3 precipitates, which are surrounded by increased levels of both strain and GND density. However, intragranular regions of increased dislocation density do not usually coincide with increased intragranular elastic strain.

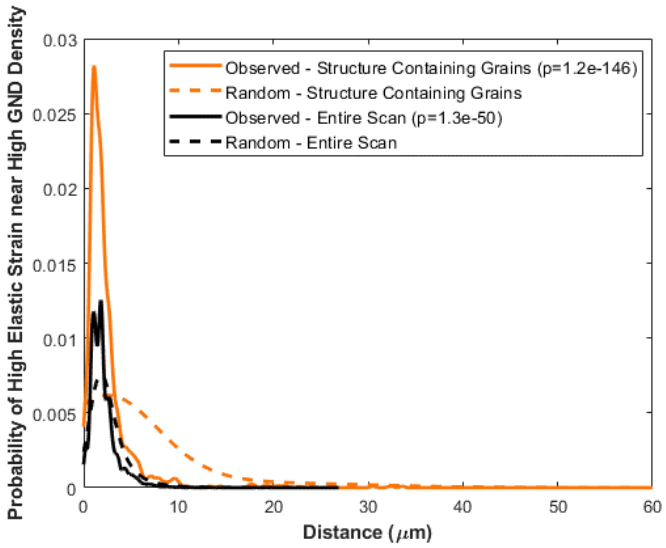

Figure 4-36. DMLS observed and random distributions in grains where dislocation substructures were observed (orange) vs the entire scan area (black). p-values are significance values of observed vs. random distribution of elastic strain in relation to GND density.

The solidification kinetics in EBF3 have not been widely studied, however this process has been shown to lead to fine grained microstructures indicative of rapid solidification mechanisms [9] as well as larger grain sizes seen here [69,75] due to the many combinations of

processing parameters. The wavy grain boundary morphology and the number of LAGBs seen here may be a product of the impingement of dendritic fronts in EBF3 components (Supp. Figure 4-2) [76,77]. The elastic strain and dislocation density in EBF3 are 2x and 1.5x that found in BJ3DP, respectively (by average), as can be expected if EBF3 results in faster solidification kinetics than binder jet, although the presence of dendrites and wavy LAGBs suggests that the EBF3 parameters used here do not quite result in rapid solidification [78]. In EBF3, the size and temperature of the melt pool result in diffusion throughout the pool as well as in the semisolid tail which has been measured to be more than 1000°C [70]. Additionally, the electron beam, unlike the laser, penetrates the deposited material to create a heat flux vertically in the z-direction [79]. The strength of the relationship between GND density and elastic strain in EBF3 (red in figure 4-4) is stronger than that found in BJ3DP and may be explained by the presence of elevated elastic strain 'clouds' that are found near GBs in EBF3.

The elastic strain and dislocation density found here in the DMLS fabricated sample are more highly linked than these features in either EBF3 or BJ3DP. Dislocation substructures seen here have been seen previously in IN625 and stainless steel fabricated by DMLS [34,37,38]. Bertsch et al. recently showed that these structures in laser AM 316L are due to residual strain caused by thermal cycles inherent in the process, while Thampy, et al demonstrated correlation between residual strain and cooling rate using X-ray diffraction in laser AM Ti-6Al-4V [35,80]. These findings emphasize the importance of tracking the evolution of residual strain in laser AM techniques, as the organization of dislocations in response to strain has a direct impact on the mechanical properties of AM materials. The solidification rate in DMLS is usually between 10^4-10^6K/s, well above the threshold for rapid solidification; since RS can happen at speeds faster

than the diffusive limit this leads to diffusionless microstructures, trapping elastic strain and dislocations in metastable states [81–83]. Indeed, the difference in elastic strain between BJ3DP and DMLS demonstrates that at slower cooling rates there is a relatively consistent absence of high elastic strain in AM IN625. While this may be an intuitive result, the distribution of elastic strain in relation to high dislocation density gives some further insight to solidification kinetics during fast solidification. DMLS resulted in the strongest relationship between elevated GND density and elastic strain (black in figure 4-4), with the observed relationship being significantly stronger than an independently distributed elastic strain with relation to the observed GND density ($p=1.3e-50$). Furthermore, in those grains where intragranular dislocation substructures were noticed, the relationship between the two was even stronger ($p=1.2e-146$) (orange in figure 4-6).

The microstructures and residual stress content in AM materials are known to be highly dependent on processing parameters and have been shown to vary across AM alloys. [84] Here, we have focused on one alloy, but the parameter dependence of structure and properties across AM techniques, including feedstock material, is difficult to account for. Microstructures and microscale properties are also location dependent within single AM components due to variations in local thermal history [85,86]; therefore the results found here are a first step toward quantifying differences in microstructure and spatial distribution of microstructural features based on the extremes of the thermal environments present in different AM processes. Future investigations on microstructural elemental segregations would further outline the mechanisms at work. Our results provide a framework of microstructural descriptors, including the characterization of elastic strain, GND density, and their spatial

evolution during a build, that if used in conjunction with machine learning-assisted processing, will aid in the understanding of the effect of thermal environment on AM microstructure and assist in development of AM simulations and automated platforms for build optimization.

Conclusions

Analysis of resultant microstructures gives indications of the relative solidification environments in different AM processes. Using the parameters in this study, DMLS has the fastest solidification rate followed by EBF3 and BJ3DP.

Average GND density and elastic strain generally increase with increasing solidification rate, with DMLS containing the overall highest GND density and elastic strain values. Likewise, we show that the spatial relationship between GND density and elastic strain is strongest in components fabricated in more violent thermal environments, being strongest in DMLS and weakest in BJ3DP. These results indicate that a faster solidification rate gives rise to organization of or interrupts diffusion of microstructural features. This is supported by previous findings on dislocation substructures and residual strain[35] and by the moderate strength of relationship in EBF3, the method with an intermediate solidification rate in this study.

The microstructural analysis shown here furthers the understanding of evolution of elastic strain and GND density during AM processes and enables the inclusion of new microstructural descriptors: GND density, elastic strain and their spatial relationship, in the building of ML frameworks such as those described by Ling et al[60], which are capable of taking into account structure and property descriptors for optimized build processes and simulations.

References

[1] T. Debroy, H.L. Wei, J.S. Zuback, T. Mukherjee, J.W. Elmer, J.O. Milewski, A.M. Beese, A. Wilson-Heid, A. De, W. Zhang, Additive manufacturing of metallic components-Process, structure and properties, (2017). https://doi.org/10.1016/j.pmatsci.2017.10.001.

[2] R. Liu, Z. Wang, T. Sparks, F. Liou, J. Newkirk, Aerospace applications of laser additive manufacturing, in: Laser Addit. Manuf. Mater. Des. Technol. Appl., Elsevier Inc., 2017: pp. 351–371. https://doi.org/10.1016/B978-0-08-100433-3.00013-0.

[3] P.D. Enrique, E. Marzbanrad, Y. Mahmoodkhani, Z. Jiao, E. Toyserkani, N.Y. Zhou, Surface modification of binder-jet additive manufactured Inconel 625 via electrospark deposition, Surf. Coatings Technol. 362 (2019) 141–149. https://doi.org/10.1016/j.surfcoat.2019.01.108.

[4] L.E. Murr, S.M. Gaytan, D.A. Ramirez, E. Martinez, J. Hernandez, K.N. Amato, P.W. Shindo, F.R. Medina, R.B. Wicker, Metal Fabrication by Additive Manufacturing Using Laser and Electron Beam Melting Technologies, J. Mater. Sci. Technol. 28 (2012) 1–14. https://doi.org/10.1016/S1005-0302(12)60016-4.

[5] Y.-L. Hao, S.-J. Li, R. Yang, Biomedical titanium alloys and their additive manufacturing, Rare Met. 35 (2016) 661–671. https://doi.org/10.1007/s12598-016-0793-5.

[6] J.J. Lewandowski, M. Seifi, Metal Additive Manufacturing: A Review of Mechanical Properties, Annu. Rev. Mater. Res. 46 (2016) 151–186. https://doi.org/10.1146/annurev-matsci-070115-032024.

[7] A. Mostafaei, E.L. Stevens, E.T. Hughes, S.D. Biery, C. Hilla, M. Chmielus, Powder bed binder jet printed alloy 625: Densification, microstructure and mechanical properties, Mater. Des. 108 (2016) 126–135. https://doi.org/10.1016/j.matdes.2016.06.067.

[8] A. Mostafaei, J. Toman, E.L. Stevens, E.T. Hughes, Y.L. Krimer, M. Chmielus, Microstructural evolution and mechanical properties of differently heat-treated binder jet printed samples from gas- and water-atomized alloy 625 powders, Acta Mater. 124 (2017) 280–289. https://doi.org/10.1016/j.actamat.2016.11.021.

[9] K. Taminger, R. Hafley, Electron beam freeform fabrication: a rapid metal deposition process, Proc. 3rd Annu. Automot. Compos. Conf. (2003) 9–10. http://www.ntrs.nasa.gov/archive/nasa/casi.ntrs.nasa.gov/20040042496_2004036110.pdf.

[10] Y. Tian, D. McAllister, H. Colijn, M. Mills, D. Farson, M. Nordin, S. Babu, Rationalization of microstructure heterogeneity in INCONEL 718 builds made by the direct laser additive manufacturing process, Metall. Mater. Trans. A Phys. Metall. Mater. Sci. 45A (2014) 4470–4483. https://doi.org/10.1007/s11661-014-2370-6.

[11] X. Zhao, J. Chen, X. Lin, W. Huang, Study on microstructure and mechanical properties of laser rapid forming Inconel 718, Mater. Sci. Eng. A. 478 (2008) 119–124. https://doi.org/10.1016/j.msea.2007.05.079.

[12] T.M. Rodgers, J.D. Madison, V. Tikare, Simulation of metal additive manufacturing microstructures using kinetic Monte Carlo, Comput. Mater. Sci. 135 (2017) 78–89. https://doi.org/10.1016/j.commatsci.2017.03.053.

[13] L.M. Suave, J. Cormier, P. Villechaise, A. Soula, Z. Hervier, D. Bertheau, J. Laigo, Microstructural Evolutions During Thermal Aging of Alloy 625: Impact of Temperature and Forming Process, Metall. Mater. Trans. A. 45 (2014) 2963–2982. https://doi.org/10.1007/s11661-014-2256-7.

[14] M.R. Stoudt, E.A. Lass, D.S. Ng, M.E. Williams, F. Zhang, C.E. Campbell, G. Lindwall, L.E. Levine, The Influence of Annealing Temperature and Time on the Formation of δ-Phase in Additively-Manufactured Inconel 625, Metall. Mater. Trans. A. 49 (2018) 3028–3037. https://doi.org/10.1007/s11661-018-4643-y.

[15] E. Popova, T.M. Rodgers, X. Gong, A. Cecen, J.D. Madison, S.R. Kalidindi, Process-Structure Linkages Using a Data Science Approach: Application to Simulated Additive Manufacturing Data, Integr. Mater. Manuf. Innov. 6 (2017) 54–68. https://doi.org/10.1007/s40192-017-0088-1.

[16] B. Yuan, G.M. Guss, A.C. Wilson, S.P. Hau-Riege, P.J. DePond, S. McMains, M.J. Matthews, B. Giera, Machine-Learning-Based Monitoring of Laser Powder Bed Fusion, Adv. Mater. Technol. 3 (2018) 1800136. https://doi.org/10.1002/admt.201800136.

[17] P. Nandwana, A.M. Elliott, D. Siddel, A. Merriman, W.H. Peter, S.S. Babu, Powder bed binder jet 3D printing of Inconel 718 : Densification , microstructural evolution and challenges q, Curr. Opin. Solid State Mater. Sci. (2017) 1–12. https://doi.org/10.1016/j.cossms.2016.12.002.

[18] K. Kimes, K. Myers, A. Klein, M. Ahlfors, E. Stevens, M. Chmielus, Binder Jet 3D Printing of 316L Stainless Steel: Effects of HIP on Fatigue, Microsc. Microanal. 25 (2019) 2600–2601. https://doi.org/10.1017/s1431927619013734.

[19] R. Hafley, K.M.B. Taminger, R. Bird, Electron Beam Freeform Fabrication in the Space Environment, AIAA Pap. (2007) 1–9. https://doi.org/10.2514/6.2007-1154.

[20] S.C. Joshi, A.A. Sheikh, 3D printing in aerospace and its long-term sustainability, Virtual Phys. Prototyp. 10 (2015) 111–175. https://doi.org/10.1080/17452759.2015.1111519.

[21] X. Shu, G. Chen, J. Liu, B. Zhang, J. Feng, Microstructure evolution of copper/steel gradient deposition prepared using electron beam freeform fabrication, Mater. Lett. 213 (2018) 374–377. https://doi.org/10.1016/j.matlet.2017.11.016.

[22] J. Xu, J. Zhu, J. Fan, Q. Zhou, Y. Peng, S. Guo, Microstructure and mechanical properties of Ti–6Al–4V alloy fabricated using electron beam freeform fabrication, Vacuum. 167 (2019) 364–373. https://doi.org/10.1016/j.vacuum.2019.06.030.

[23] K.M. Taminger, R.A. Hafley, Electron beam freeform fabrication for cost effective near-net shape manufacturing, Nato Avt. 139 (2006).

[24] J. Gockel, J. Beuth, K. Taminger, Integrated control of solidification microstructure and melt pool dimensions in electron beam wire feed additive manufacturing of Ti-6Al-4V, Addit. Manuf. (2014) 119–126. https://doi.org/10.1016/j.addma.2014.09.004.

[25] L.M. Sochalski-Kolbus, E.A. Payzant, P.A. Cornwell, T.R. Watkins, S.S. Babu, R.R. Dehoff, M. Lorenz, O. Ovchinnikova, C. Duty, Comparison of Residual Stresses in Inconel 718 Simple Parts Made by Electron Beam Melting and Direct Laser Metal Sintering, Metall. Mater. Trans. A Phys. Metall. Mater. Sci. 46 (2015) 1419–1432. https://doi.org/10.1007/s11661-014-2722-2.

[26] A.K. Agrawal, G. Meric de Bellefon, D. Thoma, High-throughput experimentation for microstructural design in additively manufactured 316L stainless steel, Mater. Sci. Eng. A. 793

(2020). https://doi.org/10.1016/j.msea.2020.139841.

[27] A.E. Patterson, S.L. Messimer, P.A. Farrington, Overhanging Features and the SLM/DMLS Residual Stresses Problem: Review and Future Research Need, Technologies. 5 (2017) 15. https://doi.org/10.3390/technologies5020015.

[28] G. Nicoletto, R. Konečná, M. Frkáň, E. Riva, Surface roughness and directional fatigue behavior of as-built EBM and DMLS Ti6Al4V, Int. J. Fatigue. 116 (2018) 140–148. https://doi.org/10.1016/j.ijfatigue.2018.06.011.

[29] D.W. Brown, J.D. Bernardin, J.S. Carpenter, B. Clausen, D. Spernjak, J.M. Thompson, Neutron diffraction measurements of residual stress in additively manufactured stainless steel, Mater. Sci. Eng. A. 678 (2016) 291–298. https://doi.org/10.1016/j.msea.2016.09.086.

[30] Z. Wang, E. Denlinger, P. Michaleris, A.D. Stoica, D. Ma, A.M. Beese, Residual stress mapping in Inconel 625 fabricated through additive manufacturing: Method for neutron diffraction measurements to validate thermomechanical model predictions, Mater. Des. 113 (2017) 169–177. https://doi.org/10.1016/j.matdes.2016.10.003.

[31] P.J. Withers, H.K.D.H. Bhadeshia, P.J. Withers, H.K.D.H. Bhadeshia, Residual stress . Part 1 – Measurement techniques Residual stress Part 1 – Measurement techniques, 0836 (2016). https://doi.org/10.1179/026708301101509980.

[32] T.B. Britton, A.J. Wilkinson, Measurement of residual elastic strain and lattice rotations with high resolution electron backscatter diffraction, Ultramicroscopy. 111 (2011) 1395–1404. https://doi.org/10.1016/j.ultramic.2011.05.007.

[33] A.J. Wilkinson, G. Meaden, D.J. Dingley, High-resolution elastic strain measurement from electron backscatter diffraction patterns: New levels of sensitivity, Ultramicroscopy. 106 (2006) 307–313. https://doi.org/10.1016/j.ultramic.2005.10.001.

[34] K.A. Small, Z. Clayburn, R. DeMott, S. Primig, D. Fullwood, M.L. Taheri, Interplay of dislocation substructure and elastic strain evolution in additively manufactured Inconel 625, Mater. Sci. Eng. A. 785 (2020) 139380. https://doi.org/10.1016/j.msea.2020.139380.

[35] K.M. Bertsch, G. Meric de Bellefon, B. Kuehl, D.J. Thoma, Origin of dislocation structures in an additively manufactured austenitic stainless steel 316L, Acta Mater. 199 (2020) 19–33. https://doi.org/10.1016/j.actamat.2020.07.063.

[36] Y. Zhong, L. Liu, S. Wikman, D. Cui, Z. Shen, Intragranular cellular segregation network structure strengthening 316L stainless steel prepared by selective laser melting, J. Nucl. Mater. 470 (2016) 170–178. https://doi.org/10.1016/j.jnucmat.2015.12.034.

[37] M.D. Sangid, T.A. Book, D. Naragani, J. Rotella, P. Ravi, A. Finch, P. Kenesei, J.-S. Park, H. Sharma, J. Almer, X. Xiao, Role of heat treatment and build orientation in the microstructure sensitive deformation characteristics of IN718 produced via SLM additive manufacturing, Addit. Manuf. 22 (2018) 479–496. https://doi.org/10.1016/j.addma.2018.04.032.

[38] Y.S.J. Yoo, T.A. Book, M.D. Sangid, J. Kacher, Identifying strain localization and dislocation processes in fatigued Inconel 718 manufactured from selective laser melting, Mater. Sci. Eng. A. 724 (2018) 444–451. https://doi.org/10.1016/j.msea.2018.03.127.

[39] A. Hadadzadeh, B. Shalchi Amirkhiz, A. Odeshi, J. Li, M. Mohammadi, Role of hierarchical

microstructure of additively manufactured AlSi10Mg on dynamic loading behavior, Addit. Manuf. 28 (2019) 1–13. https://doi.org/10.1016/j.addma.2019.04.012.

[40] T. Pinomaa, M. Lindroos, M. Walbrühl, N. Provatas, A. Laukkanen, The significance of spatial length scales and solute segregation in strengthening rapid solidification microstructures of 316L stainless steel, Acta Mater. 184 (2020) 1–16. https://doi.org/10.1016/j.actamat.2019.10.044.

[41] G. Meric de Bellefon, K.M. Bertsch, M.R. Chancey, Y.Q. Wang, D.J. Thoma, Influence of solidification structures on radiation-induced swelling in an additively-manufactured austenitic stainless steel, J. Nucl. Mater. 523 (2019) 291–298. https://doi.org/10.1016/j.jnucmat.2019.06.012.

[42] L.E. Murr, Metallurgy of additive manufacturing: Examples from electron beam melting, Addit. Manuf. 5 (2015) 40–53. https://doi.org/10.1016/j.addma.2014.12.002.

[43] Y. Han, R.J. Griffiths, H.Z. Yu, Y. Zhu, Quantitative microstructure analysis for solid-state metal additive manufacturing via deep learning, J. Mater. Res. 35 (2020) 1936–1948. https://doi.org/10.1557/jmr.2020.120.

[44] S.S. Razvi, S. Feng, A. Narayanan, Y.T.T. Lee, P. Witherell, A review of machine learning applications in additive manufacturing, in: Proc. ASME Des. Eng. Tech. Conf., 2019. https://doi.org/10.1115/DETC2019-98415.

[45] C. Herriott, A.D. Spear, Predicting microstructure-dependent mechanical properties in additively manufactured metals with machine- and deep-learning methods, Comput. Mater. Sci. 175 (2020) 109599. https://doi.org/10.1016/j.commatsci.2020.109599.

[46] H. Chandler, ed., Heat Treater's Guide: Practices and Procedures for Nonferrous Alloys, ASM International, Materials Park, OH, 1996.

[47] S. Qin, T.C. Novak, M.K. Vailhe, Z.-K. Liu, A.M. Beese, Plasticity and fracture behavior of Inconel 625 manufactured by laser powder bed fusion: Comparison between as-built and stress relieved conditions, Mater. Sci. Eng. A. 806 (2021) 140808. https://doi.org/10.1016/j.msea.2021.140808.

[48] E.A. Lass, M.R. Stoudt, M.E. Williams, M.B. Katz, L.E. Levine, T.Q. Phan, T.H. Gnaeupel-Herold, D.S. Ng, Formation of the Ni3Nb δ-Phase in Stress-Relieved Inconel 625 Produced via Laser Powder-Bed Fusion Additive Manufacturing, Metall. Mater. Trans. A Phys. Metall. Mater. Sci. 48 (2017) 5547–5558. https://doi.org/10.1007/s11661-017-4304-6.

[49] G. Marchese, S. Parizia, M. Rashidi, A. Saboori, D. Manfredi, D. Ugues, M. Lombardi, E. Hryha, S. Biamino, The role of texturing and microstructure evolution on the tensile behavior of heat-treated Inconel 625 produced via laser powder bed fusion, Mater. Sci. Eng. A. 769 (2020) 138500. https://doi.org/10.1016/j.msea.2019.138500.

[50] M. Godec, S. Zaefferer, B. Podgornik, M. Šinko, E. Tchernychova, Quantitative multiscale correlative microstructure analysis of additive manufacturing of stainless steel 316L processed by selective laser melting, Mater. Charact. 160 (2020) 110074. https://doi.org/10.1016/j.matchar.2019.110074.

[51] C. Li, R. White, X.Y. Fang, M. Weaver, Y.B. Guo, Microstructure evolution characteristics of Inconel 625 alloy from selective laser melting to heat treatment, Mater. Sci. Eng. A. 705 (2017) 20–31. https://doi.org/10.1016/j.msea.2017.08.058.

[52] S.K. Nayak, S.K. Mishra, A.N. Jinoop, C.P. Paul, K.S. Bindra, Experimental Studies on Laser Additive Manufacturing of Inconel-625 Structures Using Powder Bed Fusion at 100 µm Layer Thickness, J. Mater. Eng. Perform. 29 (2020) 7636–7647. https://doi.org/10.1007/s11665-020-05215-9.

[53] BYU - OpenXY, (2018). https://github.com/BYU-MicrostructureOfMaterials/OpenXY.

[54] T.B. Britton, A.J. Wilkinson, High resolution electron backscatter diffraction measurements of elastic strain variations in the presence of larger lattice rotations, Ultramicroscopy. 114 (2012) 82–95. https://doi.org/10.1016/j.ultramic.2012.01.004.

[55] A.C. Leff, C.R. Weinberger, M.L. Taheri, Estimation of dislocation density from precession electron diffraction data using the Nye tensor, Ultramicroscopy. 153 (2015) 9–21. https://doi.org/10.1016/j.ultramic.2015.02.002.

[56] A. Shivanandan, A. Radenovic, I.F. Sbalzarini, MosaicIA: an ImageJ/Fiji plugin for spatial pattern and interaction analysis, BMC Bioinformatics. 14 (2013) 349. https://doi.org/10.1186/1471-2105-14-349.

[57] N.H. Paulson, M.W. Priddy, D.L. McDowell, S.R. Kalidindi, Reduced-order structure-property linkages for polycrystalline microstructures based on 2-point statistics, Acta Mater. 129 (2017) 428–438. https://doi.org/10.1016/j.actamat.2017.03.009.

[58] C. Xu, S. Gao, M. Li, A novel PCA-based microstructure descriptor for heterogeneous material design, Comput. Mater. Sci. 130 (2017) 39–49. https://doi.org/10.1016/j.commatsci.2016.12.031.

[59] A. Gupta, A. Cecen, S. Goyal, A.K. Singh, S.R. Kalidindi, Structure–property linkages using a data science approach: Application to a non-metallic inclusion/steel composite system, Acta Mater. 91 (2015) 239–254. https://doi.org/10.1016/j.actamat.2015.02.045.

[60] J. Ling, M. Hutchinson, E. Antono, B. DeCost, E.A. Holm, B. Meredig, Building data-driven models with microstructural images: Generalization and interpretability, Mater. Discov. 10 (2017) 19–28. https://doi.org/10.1016/j.md.2018.03.002.

[61] S. Keshavarz, S. Ghosh, Hierarchical crystal plasticity FE model for nickel-based superalloys: Sub-grain microstructures to polycrystalline aggregates, Int. J. Solids Struct. 55 (2015) 17–31. https://doi.org/10.1016/j.ijsolstr.2014.03.037.

[62] G. Fleury, F. Schubert, H. Nickel, Modelling of the thermo-mechanical behaviour of the single crystal superalloy CMSX-4, Comput. Mater. Sci. 7 (1996) 187–193. https://doi.org/10.1016/s0927-0256(96)00079-1.

[63] H. Mughrabi, Dislocation wall and cell structures and long-range internal stresses in deformed metal crystals, Acta Metall. 31 (1983) 1367–1379. https://ac-els-cdn-com.ezproxy2.library.drexel.edu/000161608390007X/1-s2.0-000161608390007X-main.pdf?_tid=cfff344b-67bf-488c-8a81-05852b1dda3e&acdnat=1543879427_a5f0644736ba21293d3c39300b70ae4b (accessed December 3, 2018).

[64] C. Herriott, X. Li, N. Kouraytem, V. Tari, W. Tan, B. Anglin, A.D. Rollett, A.D. Spear, A multi-scale, multi-physics modeling framework to predict spatial variation of properties in additive-manufactured metals, Model. Simul. Mater. Sci. Eng. 27 (2019) 025009. https://doi.org/10.1088/1361-651X/aaf753.

[65] A. Mostafaei, P. Rodriguez De Vecchis, I. Nettleship, M. Chmielus, Effect of powder size distribution on densification and microstructural evolution of binder-jet 3D-printed alloy 625, Mater. Des. 162 (2019) 375–383. https://doi.org/10.1016/j.matdes.2018.11.051.

[66] A. Lal, R.G. Iacocca, R.M. German, Microstructural evolution during the supersolidus liquid phase sintering of nickel-based prealloyed powder mixtures, J. Mater. Sci. 35 (2000) 4507–4518.

[67] R.M. German, Supersolidus liquid-phase sintering of prealloyed powders, Metall. Mater. Trans. A Phys. Metall. Mater. Sci. 28 (1997) 1553–1567. https://doi.org/10.1007/s11661-997-0217-0.

[68] H.L. Wei, G.L. Knapp, T. Mukherjee, T. Debroy, Three-dimensional grain growth during multi-layer printing of a nickel-based alloy Inconel 718, Addit. Manuf. 25 (2018) 448–459. https://doi.org/10.1016/j.addma.2018.11.028.

[69] A. Panin, M. Kazachenok, O. Perevalova, S. Martynov, A. Panina, E. Sklyarova, Continuous Electron Beam Post-Treatment of EBF 3-Fabricated Ti-6Al-4V Parts, Metals (Basel). 9 (2019). https://doi.org/10.3390/met9060699.

[70] J.N. Zalameda, E.R. Burke, R.A. Hafley, K.M. Taminger, C.S. Domack, A. Brewer, R.E. Martin, Thermal imaging for assessment of electron-beam freeform fabrication (EBF 3) additive manufacturing deposits , Thermosense Therm. Infrared Appl. XXXV. 8705 (2013) 87050M. https://doi.org/10.1117/12.2018233.

[71] L.E. Criales, T. Özel, Temperature profile and melt depth in laser powder bed fusion of Ti-6Al-4V titanium alloy, Prog. Addit. Manuf. 2 (2017) 169–177. https://doi.org/10.1007/s40964-017-0029-8.

[72] N. Li, S. Huang, G. Zhang, R. Qin, W. Liu, H. Xiong, G. Shi, J. Blackburn, Progress in additive manufacturing on new materials: A review, J. Mater. Sci. Technol. 35 (2019) 242–269. https://doi.org/10.1016/j.jmst.2018.09.002.

[73] M. Chmielus, E. Stevens, A. Mostafaei, P. Rodriguez De Vecchis, R. Rodriguez De Vecchis, A. Acierno, K. Kimes, J. Toman, Additive Manufacturing: Opportunities and Challenges for Functional Magnetic Materials, in: 6th Int. Conf. Ferromagn. Shape Mem. Alloy., 2019: pp. 46–47.

[74] F. Pyczak, B. Devrient, H. Mughrabi, THE EFFECTS OF DIFFERENT ALLOYING ELEMENTS ON THE THERMAL EXPANSION COEFFICIENTS, LATTICE CONSTANTS AND MISFIT OF NICKEL-BASED SUPERALLOYS INVESTIGATED BY X-RAY DIFFRACTION, Superalloys. (2004) 827–836.

[75] K.M. Taminger, R.A. Hafley, Electron Beam Freeform Fabrication for Cost Effective Near-Net Shape Manufacturing, n.d. https://ntrs.nasa.gov/search.jsp?R=20080013538 (accessed May 18, 2020).

[76] R.K. Bird, J. Hibberd, Tensile Properties and Microstructure of Inconel 718 Fabricated with Electron Beam Freeform Fabrication, 2009.

[77] M. Huo, L. Liu, W. Yang, Y. Li, S. Hu, H. Su, J. Zhang, H. Fu, Formation of low-angle grain boundaries under different solidification conditions in the rejoined platforms of Ni-based single crystal superalloys, J. Mater. Res. 34 (2019) 251–260. https://doi.org/10.1557/jmr.2018.408.

[78] R. Willnecker, D.M. Herlach, B. Feuerbacher, Evidence of nonequilibrium processes in rapid solidification of undercooled metals, Phys. Rev. Lett. 62 (1989) 2707–2710. https://doi.org/10.1103/PhysRevLett.62.2707.

[79] N. Raghavan, R. Dehoff, S. Pannala, S. Simunovic, M. Kirka, J. Turner, N. Carlson, S.S. Babu, Numerical modeling of heat-transfer and the influence of process parameters on tailoring the grain morphology of IN718 in electron beam additive manufacturing, Acta Mater. 112 (2016) 303–314. https://doi.org/10.1016/j.actamat.2016.03.063.

[80] V. Thampy, A.Y. Fong, N.P. Calta, J. Wang, A.A. Martin, P.J. Depond, A.M. Kiss, G. Guss, Q. Xing, R.T. Ott, A. van Buuren, M.F. Toney, J.N. Weker, M.J. Kramer, M.J. Matthews, C.J. Tassone, K.H. Stone, Subsurface Cooling Rates and Microstructural Response during Laser Based Metal Additive Manufacturing, Sci. Rep. 10 (2020) 1981. https://doi.org/10.1038/s41598-020-58598-z.

[81] K.N. Amato, S.M. Gaytan, L.E. Murr, E. Martinez, P.W. Shindo, J. Hernandez, S. Collins, F. Medina, Microstructures and mechanical behavior of Inconel 718 fabricated by selective laser melting, Acta Mater. 60 (2012) 2229–2239. https://doi.org/10.1016/j.actamat.2011.12.032.

[82] E. Chlebus, K. Gruber, B. Kuznicka, J. Kurzac, T. Kurzynowski, Effect of heat treatment on the microstructure and mechanical properties of Inconel 718 processed by selective laser melting, Mater. Sci. Eng. A. 639 (2015) 647–655. https://doi.org/10.1016/j.msea.2015.05.035.

[83] P.J. Withers, H.K.D.H. Bhadeshia, Residual stress. Part 2 – Nature and origins, Mater. Sci. Technol. 17 (2001) 366–375. https://doi.org/10.1179/026708301101510087.

[84] A.T. Polonsky, N. Raghavan, M.P. Echlin, W.C. Lenthe, M.M. Kirka, R.R. Dehoff, T.M. Pollock, Processing-Microstructure Relationships From 3D Characterization of Additively Manufactured Metals, Microsc. Microanal. 25 (2019) 2019. https://doi.org/10.1017/S1431927619013643.

[85] Q. Wu, T. Mukherjee, C. Liu, J. Lu, T. Debroy, Residual stresses and distortion in the patterned printing of titanium and nickel alloys, Addit. Manuf. 29 (2019). https://doi.org/10.1016/j.addma.2019.100808.

[86] R. Jiang, A. Mostafaei, Z. Wu, A. Choi, P.-W. Guan, M. Chmielus, A.D. Rollett, Effect of heat treatment on microstructural evolution and hardness homogeneity in laser powder bed fusion of alloy 718, Addit. Manuf. 35 (2020) 101282. https://doi.org/10.1016/j.addma.2020.101282.

Chapter 5. Microstructural evolution in single track L-PBF Inconel 625

Introduction

Laser-powder bed fusion (L-PBF) is an additive manufacturing (AM) technique that has gained popularity in recent years due to its potential for fast, low-waste manufacturing of complex components with narrow geometric tolerances. Due to the rapid solidification (RS) level cooling rates inherent in laser processes, the microstructures of metal alloys fabricated using this technique contain high residual stresses and non-equilibrium microstructures [1,2]. Epitaxial grain growth, where grain orientation is taken from the orientation in the previous layer, is often seen in AM metals as well as high intragranular misorientation and dislocation cell structures [1,3–5]. Mechanical properties of AM alloys are often unpredictable due to the variation in microstructure depending on processing parameters. However, improved mechanical properties in AM components can be attributed to the unique structures and, specifically, the dislocation cells which are produced by these methods [6]. The non-equilibrium nature of the cells means that they are not permanent features and will recrystallize in certain conditions. Indeed, Ghiaasiaan, et al. found that heat treatment of as-printed Hastelloy X resulted in the removal of dislocation cell structures and a corresponding decrease in yield strength [7]. While solidification cell structures may be advantageous for mechanical properties, the manipulation of these features has not yet been perfected.

AM carries the potential to result in new microstructure and property combinations that can be beneficial, therefore a deeper understanding of the evolution and kinetics of microstructural features during processing is necessary. Cell structures formed by dislocation

dense cell walls have been heavily investigated in laser AM steels, and to a lesser extent in Ni superalloys. De Terris et al. reported that the volumetric energy density (VED) affects the GND density and recrystallization in L-PBF Inconel 625 (IN625) giving a simple relation for estimation of the cooling rate based on the size of dislocation cells [8]. Using crystal plasticity and phase field models, Pinomaa et al. found that the cell diameter and orientation has a direct effect on the strength of selective laser melted (SLM) 316L and that cell size is more sensitive to cooling rate than to thermal gradient [9]. Bertsch, et al. demonstrated that dislocation cell structures are more prevalent in 3D builds, compared to 2D or 1D, in direct energy deposited (DED) steel, a result that suggests that the residual strain caused by increased constraints in higher dimension builds is crucial to the formation of cell structures in stainless steel 316L [3].

The presence of residual stress and strain in AM components has been well documented and is thought to be a result of thermal contraction during solidification [10–12]. The premature failure of a component cannot always be avoided by post processing, creating yet another motivation towards full understanding and control of the AM process at the microscale. Characterization of microscale elastic strain has been demonstrated in our previous works where increased temperature gradients and cooling rates resulted in higher levels of strain as well as increased spatial correlation with dislocation density [4,13]. Simulation of residual stress in AM components has been reported on grain and bulk scales, such as in [14] where Machirori et al. demonstrate the dependence of residual stress on scanning strategy in L-PBF Ti-6Al-4V. However, the prediction of this feature on the microscale may improve the understanding of microstructural evolution during laser processing. Our characterization of microscale elastic strains results in not only the level of strain, but also its distribution, an

important aspect which could affect the bulk mechanical properties such as in medium-Mn alloys, where a homogeneous microstrain distribution was reported to increase tensile strength [15].

Due to the unique events during AM including cyclic remelting and exposure to high temperatures, the microstructure of AM components is dependent on location and thermal history. For example, recent kinetic Monte Carlo simulations by Rodgers et al. have demonstrated that there is a correlation between columnar grain sizes and the number of melting cycles experienced during a build [16]. Similarly, the grain and dendrite morphology has been found to differ both experimentally and in simulations based on the location within the build [17,18]. In finite element modeling (FEM) simulations of L-PBF Ti-6Al-4V, grain scale residual stresses have been reported to decrease in layers with more remelting cycles due to local reheating – however the extent of relaxation varied and was highly temperature dependent [14]. Here, characterization of the dislocation density and microscale elastic strain at the surface and 5mm depth of the same component support these simulations, demonstrating changes in microstructure that can result from a single build and that are attributed to differences in number of remelting cycles and relative time at elevated temperature.

The location dependence of microstructural evolution in L-PBF provides motivation for further study of the effect of temperature gradient and cooling rate on microstructural evolution during laser AM. The use of 3D builds can give some understanding of how thermal environment can shape the microstructure, but in order to have concrete understanding of solidification mechanisms in the melt pool, it is necessary to use simple geometries without the added complexities of overlap, remelting, or cyclic reheating. 1D geometries have been used

previously to analyze the effects of processing parameter on melt pool shape and resulting mechanical and microstructural properties. The conditions for keyhole mode melting and the energy density range for formation of stable tracks have both been reported using single track experiments [19,20]. The ratio between the temperature gradient, *G,* and the cooling rate, *R,* at the solid liquid interface is known to affect the solidification regime within the melt pool of single track selective laser melted (SLM) 316L, where high *G/R* results in planar, low *G/R* in dendritic and moderate *G/R* in cellular solidification [21]. Similarly, simulations of single tracks have shed light on crystallography and grain development during laser AM, demonstrating β grain structure and α phase formation as a function of laser power and scanning speed in the evolution of the two-phase Ti-6Al-4V during L-PBF [22]. Gerstgrasser, et al. used cellular automata (CA) simulations combined with experimental single track experiments to demonstrate the dependence of melt pool geometry on energy density, while Lindroos et al. used crystal plasticity models of H13 tool steel to report martensitic phase transformation and grain level residual strains in single track L-PBF [23,24]. Although single track studies have been performed to shed light on microstructural development during laser AM, the development and kinetics of dislocation cells and, especially, subgrain scale elastic strain has not been sufficiently researched.

The aims of this study are to define the spatiotemporal variation of microstructure and temperature in tandem through a combination of experimental and simulation techniques and to define the distribution of microscale elastic strain in different thermal environments. Using HR-EBSD characterization we demonstrate the morphology and orientation variations at different locations in the single track defined by thermal environments simulated by a high-

fidelity computational fluid dynamics (CFD) model. Cross-correlation and Nye tensor analysis enable calculation and spatial analysis of subgrain elastic strain and dislocation density while transmission electron microscopy (TEM) provides high resolution observation of these features. Discrete dislocation dynamics (DDD) modeling is used to provide further insight into the formation of dislocation cells as a function of temperature and stress during the laser AM process. Using these methods we demonstrate that the average microscale strain levels increase under higher temperature gradients and faster cooling rates, as does the spatial correlation between elastic strain and dislocation density. We also observe the decreased organization of dislocations, and increased dislocation density, nearer to the end of the track where thermal gradient and cooling rate are higher, suggesting dislocation movement is cut short. DDD simulations mimic this result using grain level von Mises stress as an input, suggesting that increased strain drives dislocation organization into cells.

Methods and Materials

Inconel 625 was chosen as the material of interest in this study due to its usefulness in many industries and its ability to be used in L-PBF, as well as its having well-known material constants for use in modelling and simulation environments.

Laser-Powder Bed Fabrication

An EOS M270 system was used to fabricated 10mmx10mmx10mm cubes of IN625 using a laser power of 195W, a laser speed of 700mm/s and a layer thickness of 20µm. A stress relieving step of 870°C for 1 hour was applied to this sample, which is a manufacturer-recommended process resulting in a very low level of recrystallization, if any [25–27].

Characterization of a 3D part at the surface and at 5mmdepth demonstrate the necessity of characterization of simplified geometries, which are absent of remelting or overlapping laser tracks. These samples were characterized fully in our previous works [4,13].

An L-PBF single track of IN625 powder was melted at AFRL as part of the MIDAS AM contest using an EOS M280 L-PBF system. The 20mm long track was melted on an AM printed IN625 block with a 3mm thick 'topskin' layer and commercially available, gas atomized IN625 powder. Parameters include laser power of 241W, laser speed of 1529mm/s, spot size of .1mm and a layer thickness of 40um. The relatively low volumetric energy density (VED) using these parameters results in a melt pool which does not penetrate deeply into the build plate. **Error! R eference source not found.** is a schematic of the resulting sample showing where cross-sections at different X coordinates were polished for EBSD characterization, as well as an example cross section showing the (x,y,z) coordinate system.

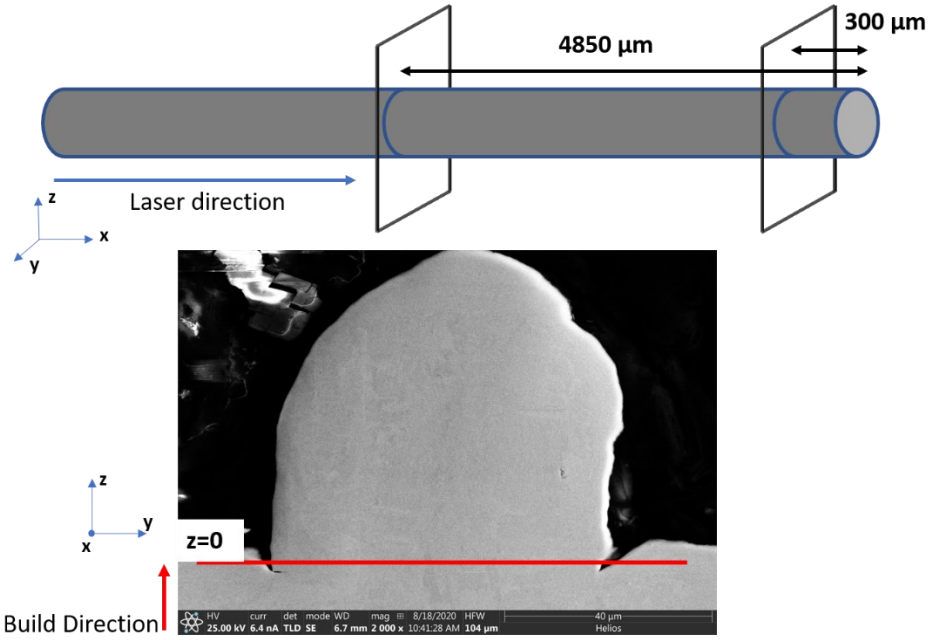

Figure 5-37.Top: Schematic of L-PBF single track of IN625 showing locations of representative cross-sections. Bottom: SEM image of cross-section of L-PBF single track showing reference coordinate system

Characterization and Statistical Analysis

All EBSD surfaces were manually sectioned and prepared for characterization by manual polishing to 1 µm using diamond suspension followed by silica. The 10mm cube was cut in half and the top surface (<100um deep) and half-depth (5mm deep, figure 5-2) while cross-sections of the single track sample were prepared in ten locations (Table 5-10). All ten locations were characterized and included in statistical analysis, while two representative locations (E and J) were chosen for demonstration of microstructural features. Characterized cross-sections were chosen in clusters at locations roughly halfway, three-quarters, and as near to the end as possible in an effort to capture distinct thermal environments and their effects on microstructural features, specifically dislocation density and elastic strain.

SEM high resolution electron backscatter diffraction (HR-EBSD) was used for orientation, elastic strain, and dislocation density analysis. EBSD was carried out on a FEI XL30 ESEM equipped with an EDAX DigiView camera and a Helios NanoLab DualBeam using an EDAX Velocity camera with 1x1 binning. Kikuchi patterns of each scan were collected for cross-correlation calculation of elastic strain with OpenXY [28].

The Ga^{+} focused ion beam (FIB) on the Helios NanoLab DualBeam was used to lift out and polish TEM samples from the same regions analyzed by SEM in samples E and H (figure 5-3) for TEM data collection, allowing the cross-sections of dislocation structures seen in SEM. TEM data was obtained with a Thermofisher Spectra 300kV fitted with an X-CFEG cold field emission source, panther STEM detection system, Super-X symmetrical quad-crystal EDS system and 5^{th} order corrected S-corr Cs probe corrector. The system also has an EMPAD (Electron Microscope Pixel Array Detector) fitted for the acquisition of 4D STEM data. The cell diameter, thickness of cell walls, and the accompanying elemental microsegregation was measured to inform theories of solidification kinetics during laser processing.

Dislocation density analysis was performed on EBSD and TEM-PED acquired data using the Nye tensor lower bound calculation described by Leff et al. [29]. It should be noted that this method results in increased accuracy of dislocation density with improved spatial resolution of the characterization method; as the length scale of dislocation spacing is approached, information regarding all dislocations begins to be accessible. However, with the relatively poor spatial resolution of EBSD, the dislocation density is calculated using curvature in the orientation data, giving access only to geometrically necessary dislocations (GND). Using TEM

data will therefore result in increased dislocation density, since the improved spatial resolution of TEM allows a higher fraction of dislocations to be counted.

Table 5-10. Locations of analyzed cross-sections for statistical analysis. Representative cross-sections for demonstration are in red.

Sample	Distance from end of track (µm)
A	8500
B	5000
C	4950
D	4900
E	4850
F	1000
G	950
H	300

Elastic strain and dislocation density at each cross-section of the single track analyzed by EBSD were observed in tandem to note dislocation cells and strain concentrations which may impact one another during L-PBF processing. The spatial correlation between high dislocation density and high elastic strain was quantified using the MosaicIA Fiji/ImageJ plugin [30]. This method was used previously to determine increased spatial relationship between high elastic strain and GND density in IN625 fabricated by three different AM techniques, where laser processing demonstrated a significantly increased relationship between the two features [13]. Analysis of a single sample at different locations in the build by this technique may improve understanding between thermal environment and existing cell structures or elastic strain concentrations.

Simulations and Computational Techniques

A high-fidelity computational fluid dynamics model, FLOW-3D, was used to obtain fluid motion and temperature profiles at locations halfway through and 300um away from the end of the track. Briefly, the model numerically solves coupled mass, energy and momentum conservation equations, and tracks the fluid surface *via* Volume of Fluid Advection with the split Lagrangian method; details of the equations used in this method can be found in [31–33] . Physical properties for Inconel 625 were used (Table 5-2) with all properties (e.g., density, thermal diffusivity, surface tension) as temperature-dependent. The heat input, assuming a Gaussian distribution, is modeled as vertical rays that undergo partial absorption and reflect until the ray flux is <5% of its initial value [19,34].

The 3-D computational domain consisted of a powder layer (5,520 µm in length, 100 µm in width, 120 µm in height,), on top of a substrate/previous build layers (5,520 µm x 708 µm x 360 µm). A 6 µm grid spacing was used in the substrate region where the material underwent a phase transformation from solid-to-liquid, a 12 µm grid spacing was used in the un-melted regions, a 3 µm grid spacing was used in the powder region to capture partial particle melting, and a 1 µm grid spacing was used in two small regions (~20x20x50 μm^3) where experimental analysis was performed. Due to computational constraints, and preliminary simulations which suggest the thermal profile in the single track does not change significantly until approximately 300 µm away from the end of the track, a single laser track of only 1mm long was modelled. The simulations took ~168 hours of CPU clock time, using a workstation with an Intel(R) Core(TM) i9-7940x CPU @3.10 GHz and 64 GB RAM.

Table 5-11. Thermo-physical properties of IN625 in this study

Property	Value	Temperature Range [K]
Melting Point [K]	Solidus	1577.15
	Liquidus	1689.15
Enthalpy of Fusion [J/g]	260	-
Enthalpy of Vaporization [J/g]	7340	-
Density [g/cm^3]	$8.19 – 3.62x10^{-4}$ *(Tempature-298K)	298-1577.15
	$7.727 – 2.9x10^{-3}$ *(Tempature-1577.15K)	1577.15-1689.15
	$7.4 –1.5x10^{-4}$ *(Tempature-1689.15K)	1689.15-3000
Specific heat [J/g/K]	$0.435 + 1.45x10^{-4}$ *(Tempature-298K)	298-1577.15
	$0.62 + 9.0x10^{-4}$ *(Tempature-1689.15K)	1577.15-1689.15
	0.72	1689.15-3000
Thermal conductivity [W/cm/K]	$0.089 + 1.3x10^{-4}$ *(Tempature-298K)	298-1577.15
	$0.258 + 3.4x10^{-4}$ *(Tempature-1743K)	1577.15-1689.15
	0.296	1689.15-3000
Surface tension [g/s^2]	1970-0.34 *(Tempature-1743.15K)	1689.15-3000
Viscosity [g/cm/s]	$0.072-1.15x10^{-4}$ *(Temperature-1689.15K)	1689.15-3000
Saturation Pressure [Pa]	$1.013x10^5$	-
Absorption coefficient	0.55	298-3000

Three dimensional (3D) Discrete dislocation dynamics (DDD) simulations were performed using an in-house modified version of the 3D DDD open-source code ParaDiS [35,36] to provide a mechanistic view of the evolution of dislocation ensembles under L-PBF processing conditions. To model dislocation plasticity in L-PBF IN625, additional aspects must be considered in 3D DDD: (i) The temperature and stress profiles originating from the thermo-mechanical stresses in laser processing, and (ii) a physically meaningful representation of the dislocation mobility and interaction in the chemical environment of IN625 involving solute microsegregation.

To obtain the temperature and stress profiles during an L-PBF single track of IN625, we performed 3D thermo-mechanical FEM simulations using the commercial FEM suite ABAQUS in version 2020. The L-PBF processing was modeled as a uniform surface heat flux which moves

along the laser scanning direction on a length of 6mm with the velocity equivalent to the experiment. The intensity and size of the heat flux in the FEM simulation was adjusted such that the resulting melt pool size and shape is sufficiently equivalent to the experiments and CFD simulations. Further, in the interest of simplicity we assume an isotropic elastic-perfectly plastic material model with temperature-dependent thermal and mechanical material parameters [37].

The stresses and temperature profile obtained from the FEM simulation serves as an input to the DDD simulation, Furthermore, to account for the stress induced by alloying atoms on the dislocations as they glide in the crystal lattice, we utilize the model developed by [38,39]. In this model, the critical resolved shear stress (CRSS) for a dislocation segment is derived from the elastic interaction between the solutes and a dislocation segment which can be quantified by an energy barrier ΔE_b which the dislocation must overcome after reaching the related zero-temperature strength τ_c^0 [38]. By accounting for thermal activation, the CRSS of the dislocation can be described as [40]

$$\tau_c(T,\ \dot{\varepsilon}) = \begin{cases} \tau_c^0 \exp\left(-\frac{1}{0.52}\frac{kT}{\Delta E_b}\ln\frac{\dot{\varepsilon_0}}{\dot{\varepsilon}}\right) & 0.2 < \frac{\tau_c}{\tau_c^0} < 0.5 \\ \tau_c^0 \left(\frac{1}{0.52}\frac{kT}{\Delta E_b}\ln\frac{\dot{\varepsilon_0}}{\dot{\varepsilon}}\right)^{-\frac{1}{0.54}} & \frac{\tau_c}{\tau_c^0} < 0.03 \end{cases},$$

which is separated into a medium ($0.2 < \frac{\tau_c}{\tau_c^0} < 0.5$) and a high temperature regime ($\frac{\tau_c}{\tau_c^0} < 0.03$), between which we interpolate using a Gaussian cumulative distribution function of the normal distribution. Further, T is the temperature, k is Boltzmann's constant, $\dot{\varepsilon}$ is an experimental strain rate and $\dot{\varepsilon_0}$ is a reference strain rate [38]. For the energy barrier ΔE_b and the zero-temperature strength τ_c^0 we use the formulations described in [38], which only depend on the

elastic parameters, the solute concentration, c_i, and the average misfit volume, $\Delta\bar{V}_i = V_i - \bar{V}$, of the individual solute, i, which compares the individual atomic volume, V_i, to the average atomic volume, $\bar{V} = \sum_i c_i V_i$. The elastic parameters are the same as for the FEM simulation and the individual atomic volumes are given in **Error! Reference source not found.**.

All DDD simulations incorporate a microsegregation of Molybdenum (Mo) and Niobium (Nb) in cell walls with a chemical composition given in 5-3. The microsegregation was modeled as a step-wise transition between cell wall and cell interior using a cell wall thickness of 200nm. In all DDD simulations, the cell walls are oriented parallel to the [100] and [010] plane with 800nm spacing, leading to cells elongated in [001] crystal direction. We assume that this chemical segregation is formed during solidification and is maintained during cool-down. We use a simulation volume of $5^3 \mu\mathrm{m}^3$ with an initial dislocation density of $\approx 10^{12}\mathrm{m}^{-2}$.

Table 5-12. Chemical composition in the solidification cell walls and cell interior from [41,42], atomic radii r_i from [43], and the atomic volume $V_i = a_i^3/4$ with the lattice constant, $a_i = (4r_i)/\sqrt{2}$, for the different elements used in the current study.

	Mo	Fe	Ni	Cr	Nb
Composition cell walls (%)	11	4.8	59.1	21.1	4
Composition cell interior (%)	7	5.2	63	22.2	2
Atomic radius (nm)	0.13626	0.12412	0.12459	0.12491	0.14290
Atomic volume (nm^3)	0.0143113	0.0108168	0.0109402	0.0110247	0.0165071

Results

Microstructural Characterization

Figure 5-2 demonstrates the microstructural evolution occurring during L-PBF processing by showing the inverse pole figure (IPF), elastic strain and GND density maps at different depths of the same 3D sample. In addition to the grain boundary (GB) character changing from the surface to the center of the material, the average elastic strain and GND density values both decrease, suggesting some level of recrystallization taking place with increased exposure to remelting and the HAZ. The elastic strain near the surface of the sample exceeds 1%, which is beyond the reported plasticity limit for Ni superalloys [44,45]. It has previously been reported that laser processing of metals can result in microstrains which exceed the yield limit for the material without inducing structural plastic collapse [46,47], however these regions of increased strains could also be a result of reference patterns chosen by the OpenXY algorithm was of low image quality or was not near the average grain orientation. These results demonstrate the non-equilibrium nature of laser AM microstructures that evolve during processing and can remain in a finished component until post-processing.

Figure 5-3 shows two full cross sections at locations halfway through the single track (4850um from end, sample E) and 300um from the end of the track (sample H). The difference in the shape of the melt pool is immediately noticeable, with the end location showing a non-melted particle fused to the melted powder. The overall grain morphology showing epitaxial growth from the build plate prevails in both locations.

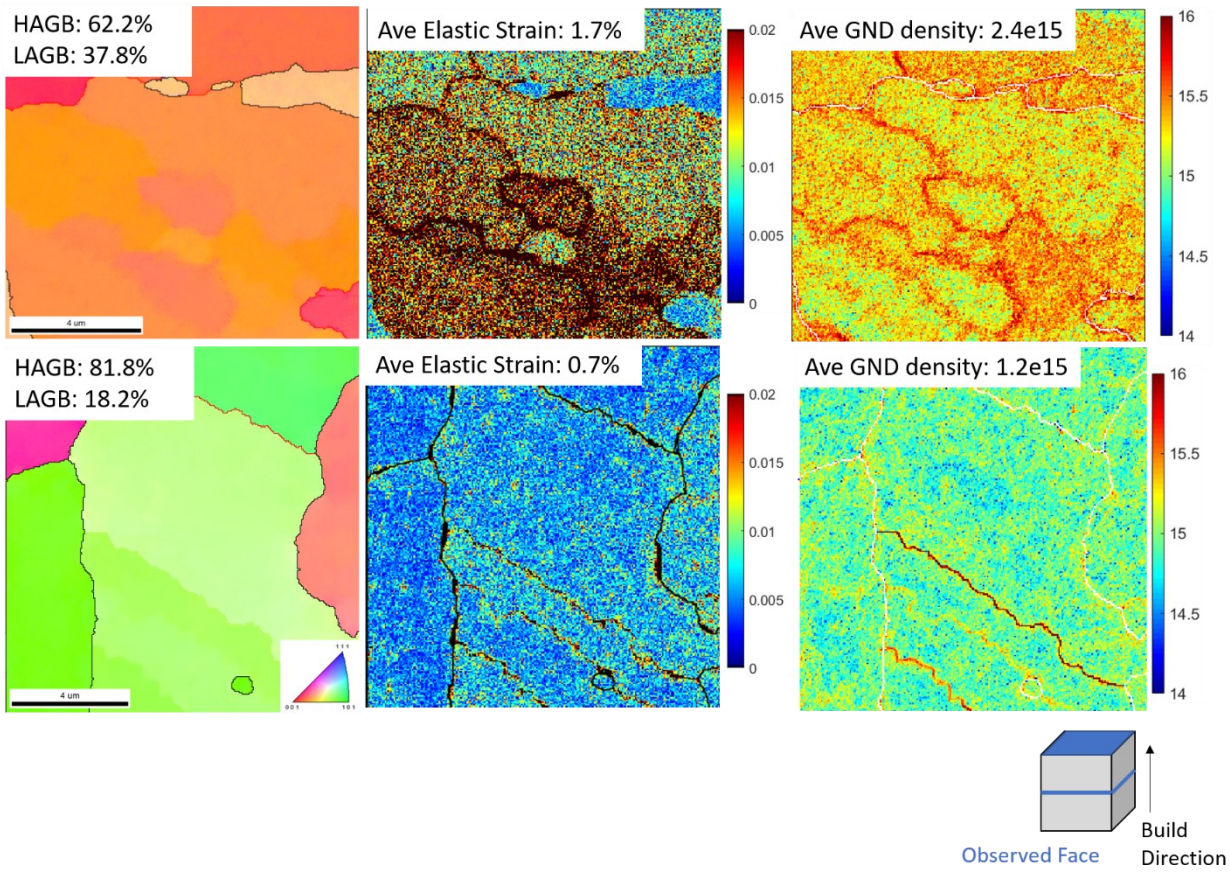

Figure 5-38. IPF, elastic strain and GND density at the surface of a bulk L-PBF IN625 sample (top) and at 5mm depth of the same part (bottom) demonstrating changes in microstructure during processing

Figure 5-4 shows the IPF map, GND density distribution, and calculated elastic strain map of the inset regions of Figure 5-3 characterized using HR-EBSD. In the IPF maps, intragranular misorientation is observable based on slight variations in color, where sample E shows slightly higher misorientation than sample H (maxima of 8.4 and 4.8 degrees, respectively). The average GND density shown in Figure 5-4 differs between locations by approximately 1e15 m^{-2} (3.2e15 in sample H and 2.9e15 is sample E). The average calculated elastic strain shown in figure 5-3 differs by 1.6% (.03 in sample H and .014 in sample E). Also

noticeable in the GND density and strain maps is the change in morphology of the dislocation cells and the arrangement of elastic strain in relation to the cell walls; in sample E, the GND dense walls are discrete and the interiors contain relatively low GND density. Similarly at this location the elastic strain is largely contained in the cell walls, perhaps indicating the cross-correlation is picking up on long-range strain fields arising from high dislocation density. In sample H, the dislocation cell walls are able to be visualized, however they are more diffuse and indeed the maximum dislocation density in this location (3.1e16 m^{-2}) is half of the maximum density in sample E (6.6e16 m^{-2}). The elastic strain is also less organized and more likely to be distributed within the cell interior. The orientation of similar dislocation cells in stainless steel and other Ni alloys has been reported to align with the [100] orientation [1,3]. Figure 5-4b echoes these findings, showing the long axis of the cells aligning well with the shown <100> direction; in Figure 5-4e the orientation of the cells is less clear due to their diffusive nature, however a small change in the oberved orientation may not result in a measurable shape change in the cells, as demonstrated by Voisin, et al. [1].

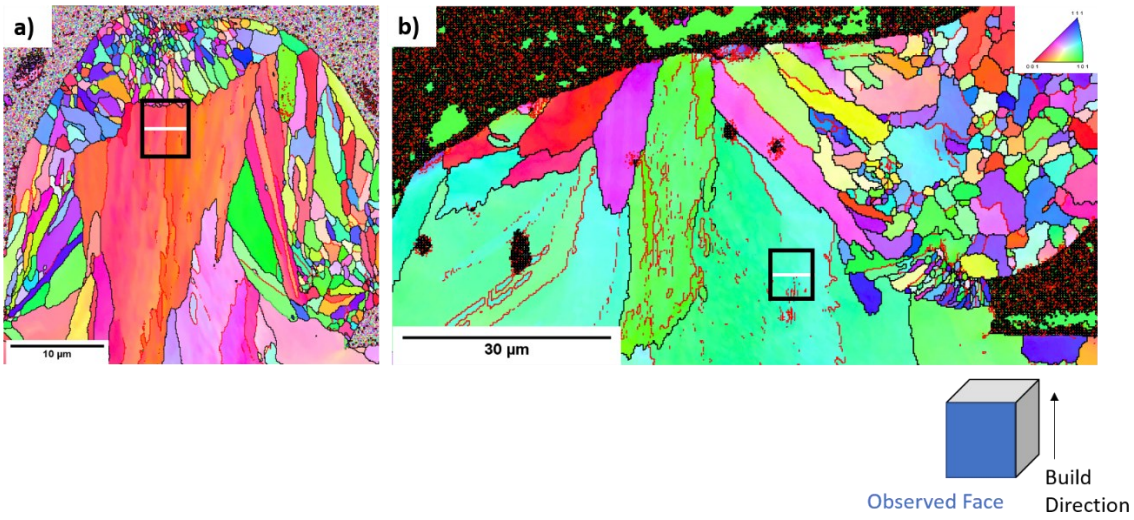

Figure 5-39. IPF maps of full cross sections a) 4850 µm and b) 300 µm from the end of the melted track. Black insets show regions which contained dislocation cells where HR-EBSD GND density and strain analysis were performed, white lines show the locations of TEM liftouts.

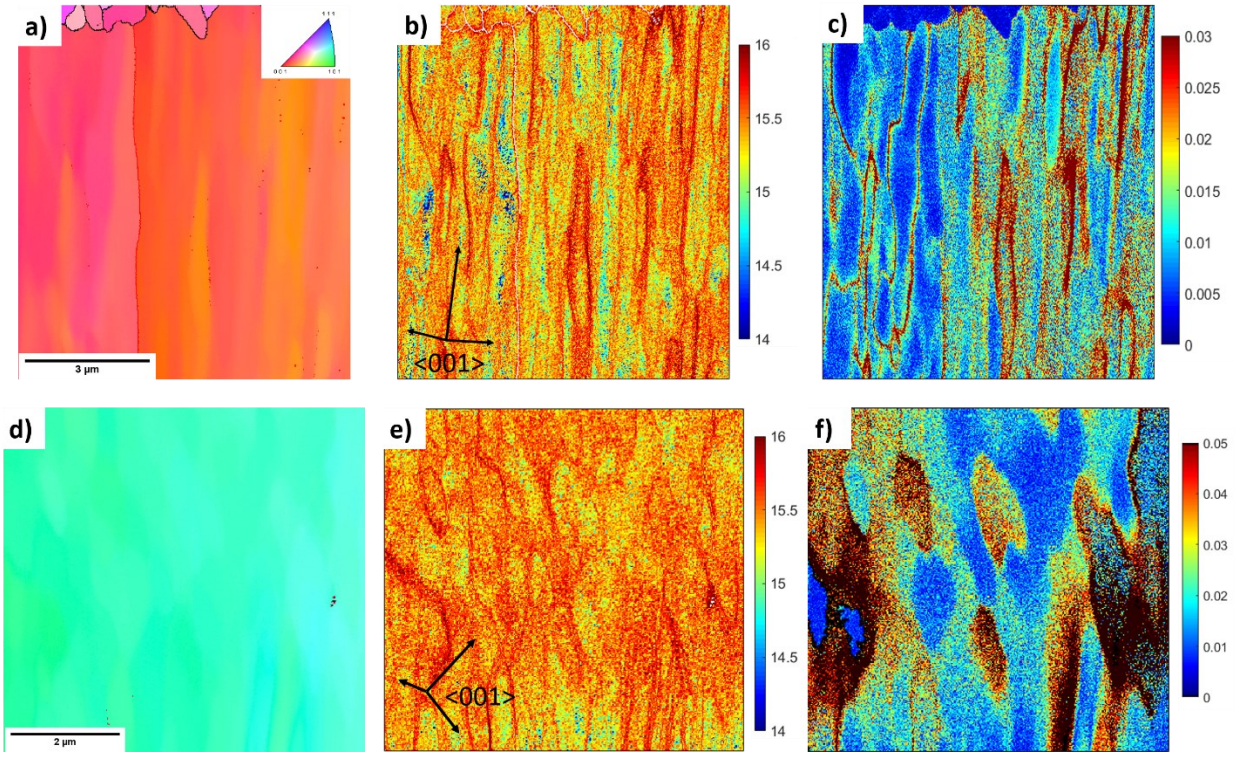

Figure 5-40. IPF, GND density and elastic strain maps from (a-c) sample E (4850um from the end of track) and (d-f) sample H (300um from end of track). Note the difference in color scale of elastic strain.

Ten locations were characterized using HR-EBSD for quantitative and statistical analysis of microstructural features. The average calculated elastic strain in most samples is approximately 1%, while near the end of the track the average strain leaps up to 3%, again exceeding the elastic limit for IN625. Spatial interaction analysis was carried out on the high GND density and high elastic strain values using MosaicIA, where the strength of a random, independent relationship between two features is defined as zero [30]. In figure 5-5, the strength of the relationship is highest at 300µm from the end of the single track (sample H) and tends to decrease with increasing distance from the end of the track. In this analysis, values of strain between .78 and 1% were used as the high values to eliminate phantom high strains which may be caused by low quality Kikuchi patterns.

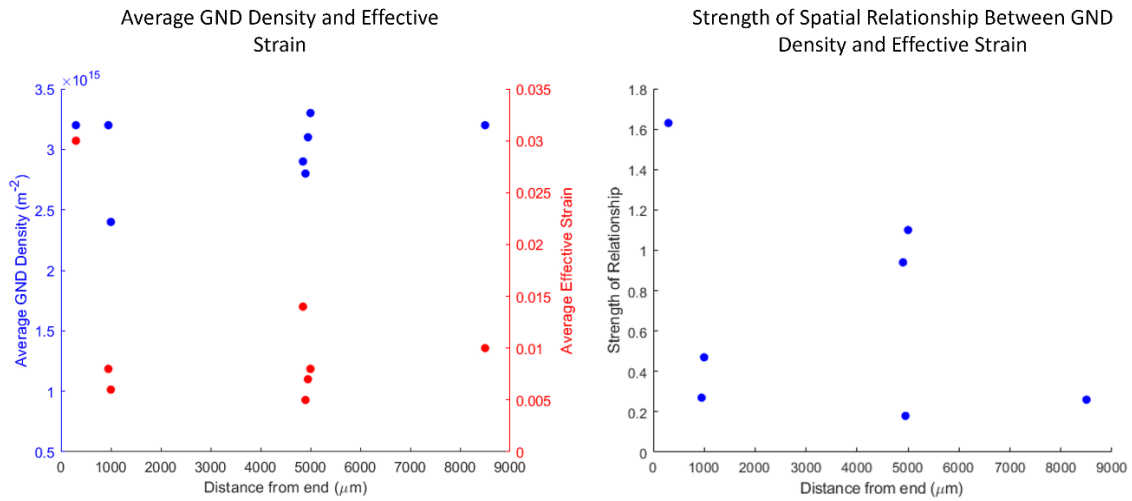

Figure 5-41. (left) Average GND density and elastic strain with distance from end of track and (right) the strength of the spatial relationship between GND density and elastic strain

TEM results of samples E and H are shown in Figure 5-6. The average cell diameter in location E is 600nm, with cell walls that are a bit wider than typical grain boundaries, about 20-30nm. Figure 5-6 shows a representative cell in sample E, including microsegregation of Nb to the cell walls. The average cell diameter in sample H is 362nm, with cell walls that are thicker than those at location E, reaching up to 60nm with an average approximately 30nm wide. A higher number of dislocations are seen in the cell interior in sample E, similar to what was seen using HR-EBSD.

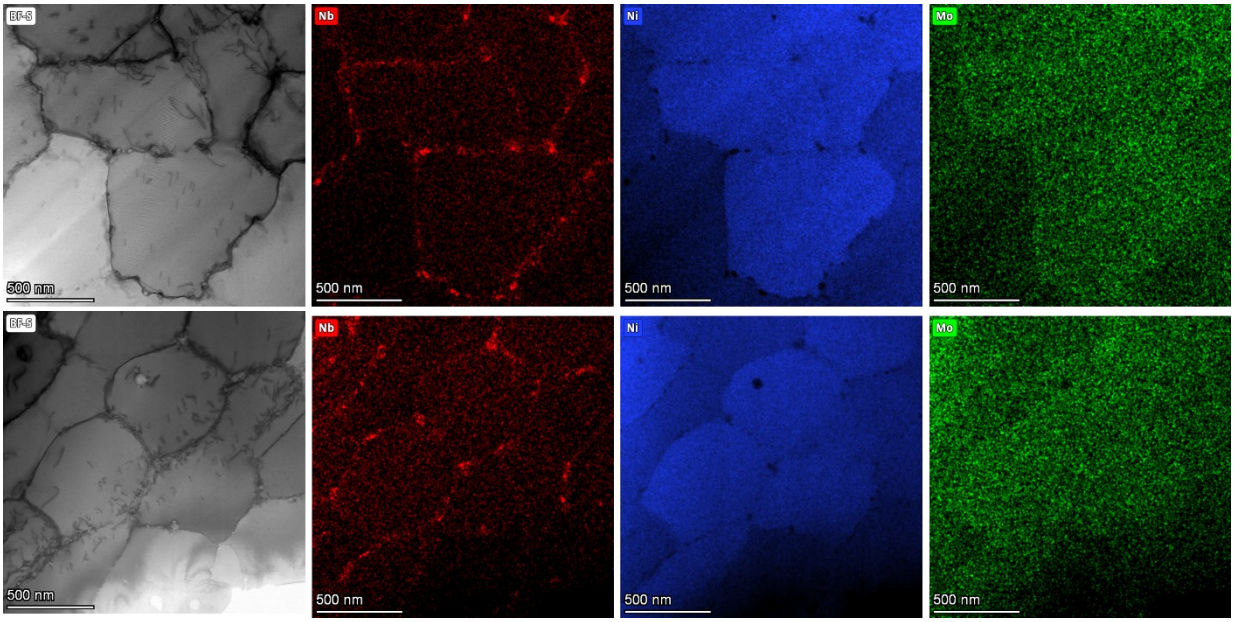

Figure 5-42. Top: Representative dislocation cell in sample E, halfway through L-PBF single track IN625, Bottom: Representative cell in sample H near the end of the single track

CFD Thermal Simulations

Figure 5-7 shows the relative thermal environments simulated by the CFD model of powder-bed IN625. Because the temperature exceeds the melting point of the material, the fluid does not remain in the fixed coordinates of the simulation window, which results in

discontinuous temperatures changes when neighboring pixels drop to room temperature (293K). During processing, the point closest to the end of the track is seen to reach the highest temperature in addition to reaching the highest cooling rate. However, the highest cooling rate here (2.8e8K/s) is seen to be during an abrupt return to room temperature by the flowing of molten metal out of the simulation frame (Figure 5-7). Even so, the peak cooling rate reached near the end of the simulated track when the metal cools down enough to stop flowing out of the simulation frame is nearly an order of magnitude higher than the cooling rate reached in the middle of the track (2.1e7 K/s and 4.2e6 K/s, respectively). This decreased cooling rate results in an increased time at elevated temperature hallway through the track (circle in figure 5-7), which allows a brief window for increased evolution of cell structures.

Figure 5-8 shows the spatial thermal gradient at the moment of peak cooling rate at each location in the CFD simulation. At halfway through the track (X=500µm) the highest thermal gradient during cooling is at a later time point than at X=700µm, as can be seen in the graph in figure 5-7 and in figure 5-8. Additionally, the thermal gradient at maximum cooling rate is 6x higher at X=700µm than at X=500µm (Table 5-4).

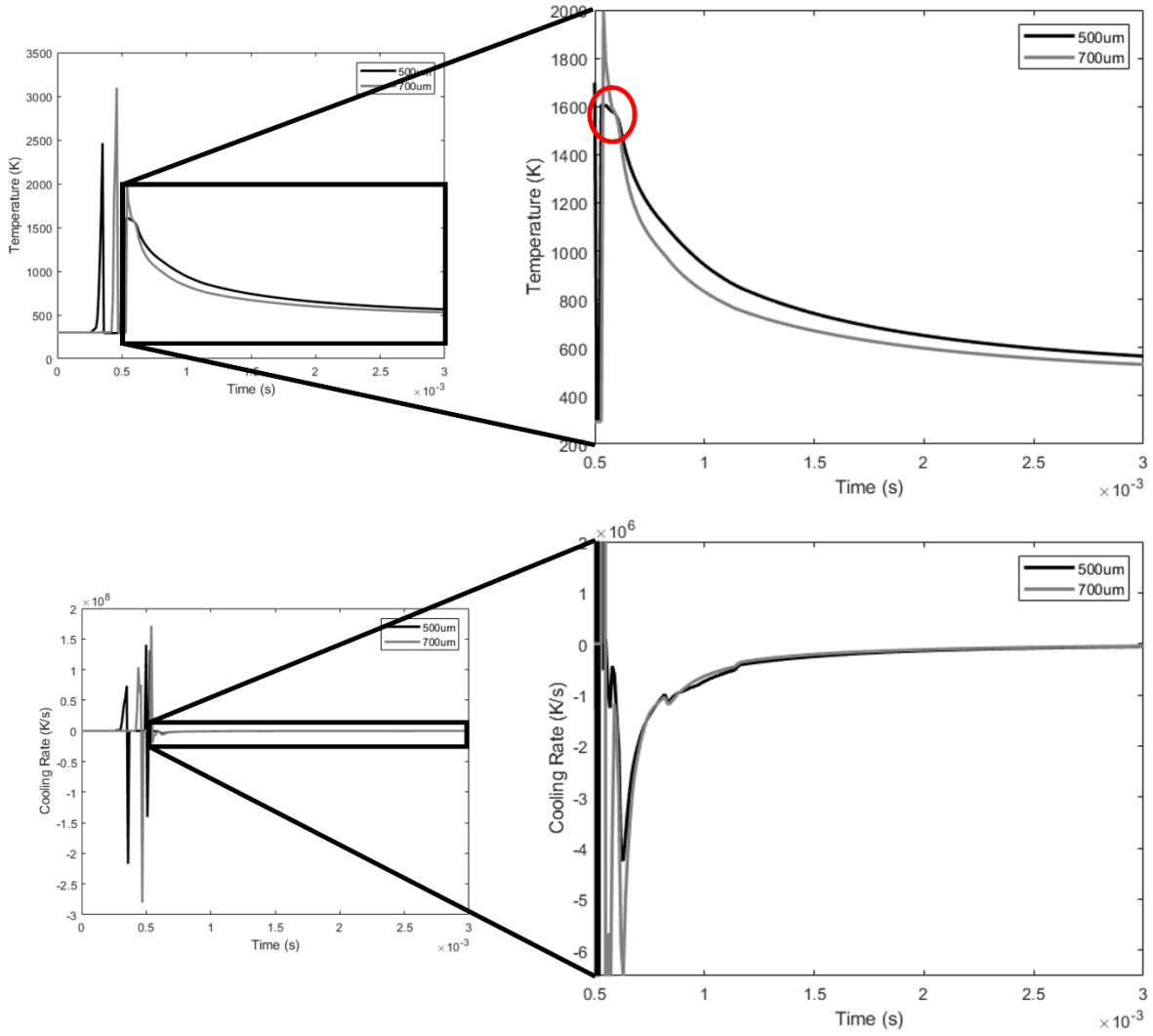

Figure 5-43. Temperature (top) and cooling rate (bottom) of different locations in the CFD simulation. Insets are temperature and cooling rate. The circled region in the temperature profile shows an increased time at high temperature halfway through the track, analogous to location E.

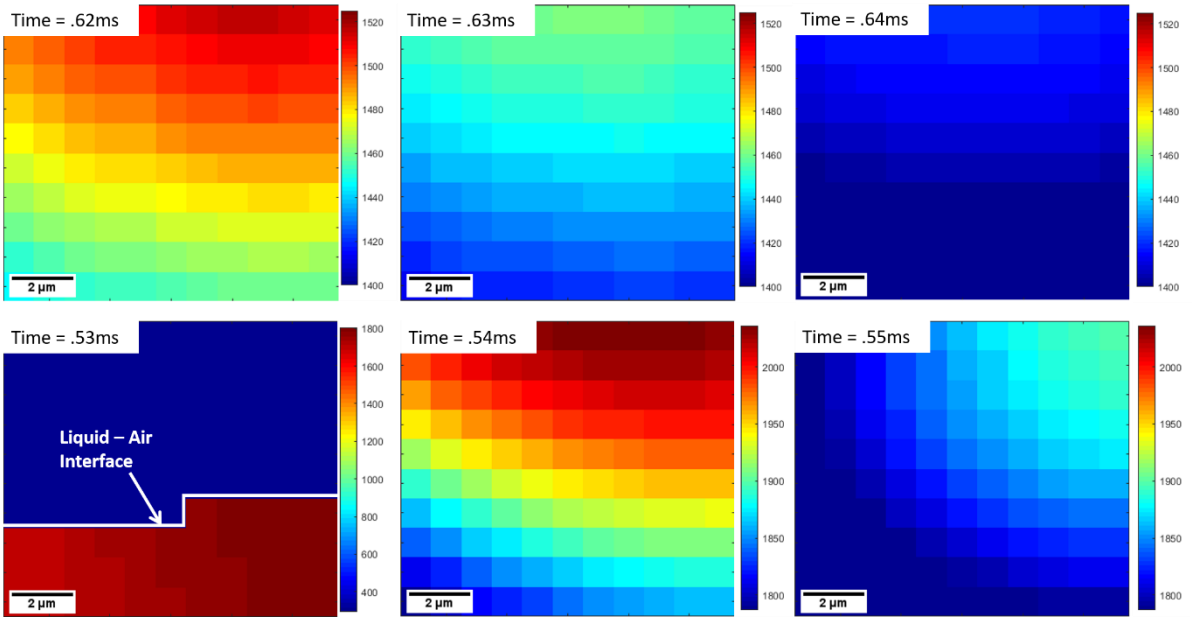

Figure 5-44. Temperature maps from 1 micron resolution CFD simulation of regions of interest captured by HR-EBSD showing difference in thermal gradient at (top) X = 500um and (bottom) X = 300um from end of track

Table 5-13. Thermal data from CFD simulation of IN625 single track

X Position (µm)	Max. Temp. (K)	Max. Cooling Rate (K/s)	Max. Thermal Gradient (K/mm)	Time at Max. Cooling Rate (ms)
500	1516.0	4.3e6	3852.5	.63
700	2036.0	2.1e7	19531.3	.54

Dislocation Simulations

Discrete dislocation dynamics (DDD) simulations at x=500µm and x=700µm were performed to observe the predicted dislocation behavior during the single-track modeled by CFD simulation. Figure 5-9 shows the difference in dislocation arrangement at each location, where at x=500µm the dislocations are organized into previously reported cell structures and are elongated in the [001] direction. At x=700µm, however, the dislocations are more loosely organized and there is an increase in the dislocation density, echoing the results from EBSD and

TEM. The DDD model shows dislocation movement in a volume, figure 5-9 shows 2D representations of the full simulated volume, while figure 5-10 shows slices of the volume, giving a better comparison to TEM results. Figure 5-10 demonstrates the decrease in GND density near the center of the track, and the lack of organization close to the end of the track which, in the DDD simulation, is a result of higher stress near the end of the track than in the center at the same temperature.

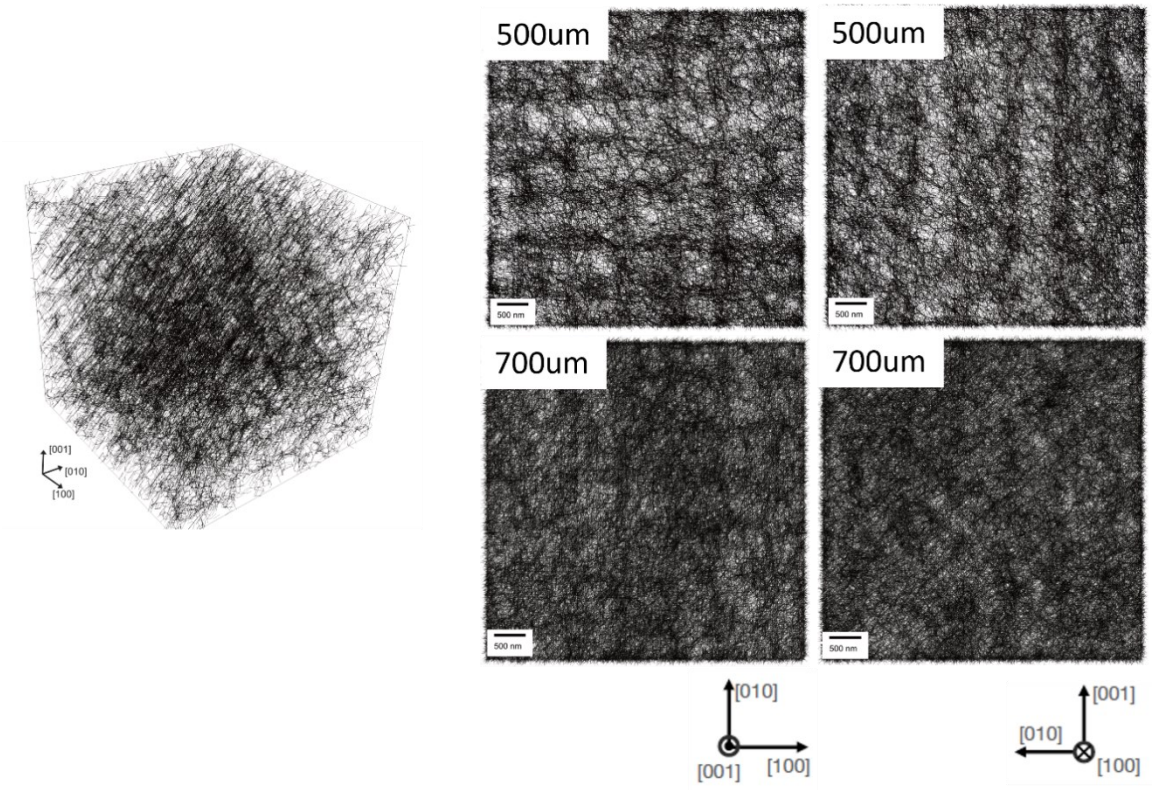

Figure 5-45. (left) 3D representation of DDD simulation and (right) 2D side views showing increased organization of cell structures at x=500µm and increased dislocation density at x=700µm

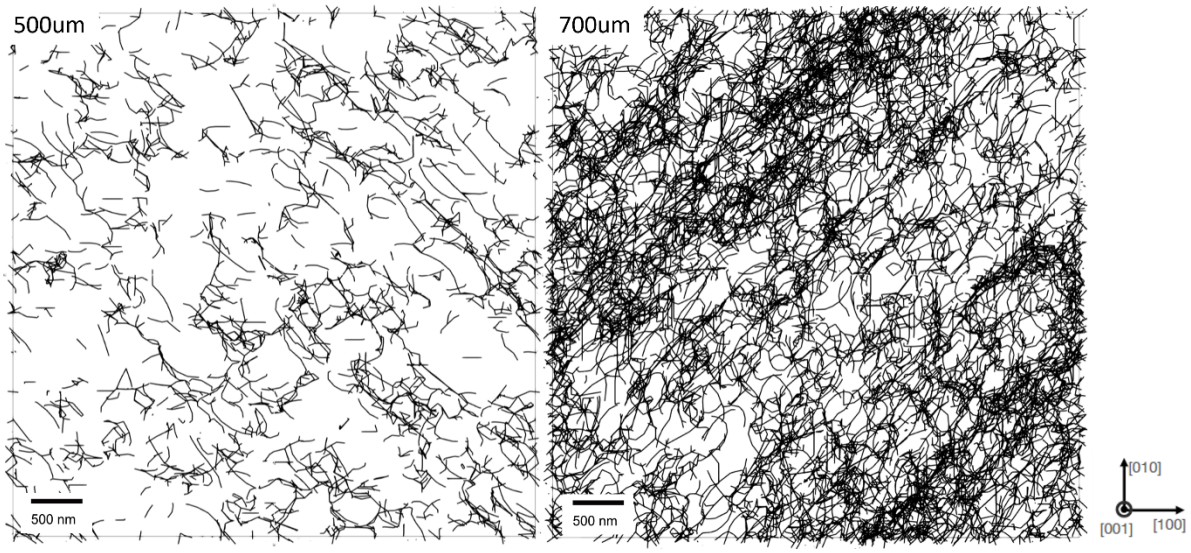

Figure 46. (left) Slice of volumetric DDD simulation from center of track, and (right) slice of volumetric DDD simulation from end of track

Discussion

The presence of cell structures has been well documented in AM microstructures, but their non-equilibrium nature has made their origins and properties difficult to characterize. Here, HR-EBSD has shown that the formation of dislocation cells is tied to the thermal environment and strain state of the surrounding microstructure. This supports the results shown by Bertsch et al. [3] that showed decreased dislocation density in cell walls in 1D builds of laser AM 316L. The single track in this study could also be considered a 1D build, however the single track in [3] was built with the long axis in the Z-direction, while our long axis was in the X-direction, meaning the 1D build here included the constraints of the build plate, presumably resulting in higher strains than in a Z-direction 1D build. Here, the resulting elastic strain is shown to vary depending on location (and therefore on thermal environment) within the build. In location E, the average elastic strain is around 1%, which has been reported as the elastic limit in IN625, while in sample H the average strain was calculated to be 3%. Local

stresses which exceed the yield strength of a material (i.e. hot spots) do not necessarily induce mechanical failure, but may drive microstructural deformation during the cyclic thermal processes of laser AM, in addition to being more vulnerable to mechanical attack [48]. The 'hot spots' of high elastic strain in sample H are localized within the cell structures, while in sample E the elastic strain has not only relaxed, but the highest levels of strain have been largely isolated to the cell walls with the dislocations. The evolution of strain distribution suggests that the small amount of microstructural evolution which is allowed to occur over the time scale of solidification in location E may be driven by, and eventually relax, much of the microscale elastic strain initially present during solidification; in location H, where there is a shorter time scale of solidification, the microstructure is not allowed to evolve to the same extent.

Planar, dendritic and cellular solidification have all been reported in laser AM depending on the ratio between thermal gradient, *G*, and cooling rate, *R* [9,49]. In 2D phase field models, Pinomaa et al. predicted that at high solidification velocities and thermal gradients of 10^6-10^7K/m, planar solidification will prevail, and a microstructure of uniform composition will occur. However, at intermediate solidification velocities (.012-.06m/s) and high thermal gradients (10^5-10^7K/m) cellular solidification and elemental segregation to the cell walls occurs. Additionally, the cell spacing can be used to estimate the cooling rate and solidification velocity, although the cell spacing is not consistent at intermediate thermal gradients below 10^6K/m [9]. The cell structures present in HR-EBSD and TEM analysis demonstrate similar diameters and levels of elemental microsegregation, but with varying widths of cell walls. During cellular solidification elemental segregation is not dependent on diffusion during solidification, so the level of elemental segregation and the presence of small Nb inclusions at the cell wall is due to

the thermal gradient and cooling rate at each location (Figure 5-6). The thermal gradient in this sample is not found to be high enough to result in planar solidification and therefore the Nb inclusions at the cell wall are to be expected. The level of Mo segregation was not seen to be as high here as in other laser processed Ni superalloys, but the level of Nb segregation and the presence of Nb heavy intermetallics along cell boundaries agree with simulations of cellular solidification during single track laser processing [5,9].

Dislocation cell boundary width was shown using TEM to increase at higher thermal gradients, resulting in a more diffuse organization of dislocations seen in HR-EBSD. The diffusive nature of the cell walls in sample G demonstrates that the cooling rate was too fast to allow for fully discrete cell walls to form, while the thinner cell walls in sample B+++ suggest a slightly slower cooling rate, allowing a greater degree of dislocation arrangement. The experimental results shown here demonstrate evolution of the non-equilibrium structures commonly seen in laser processed alloys. In location E, where the thermal gradient and cooling rate are relatively low compared to location G, the elastic strain is highly localized to the cell boundaries where dislocation density is also increased. However, in location G the high elastic strain is largely contained within diffuse dislocation structures. The TEM images mimic these differences in dislocation organization – showing more dislocations within cells in location G than in location E. The combined results of HR-EBSD, TEM and thermal gradient show that the increased time at elevated temperature in location E enables increased microstructural evolution, including strain relaxation and dislocation movement. This slower solidification rate enables the development of non-equilibrium cell structures, where increased strain and dislocation density are localized to cell boundaries between 20-30nm wide. The increased elastic strain that is initially induced

by the laser, when given time and elevated temperature, relaxes and drives dislocation movement to cell boundaries, where elemental segregation has occurred (Figure 5-11).

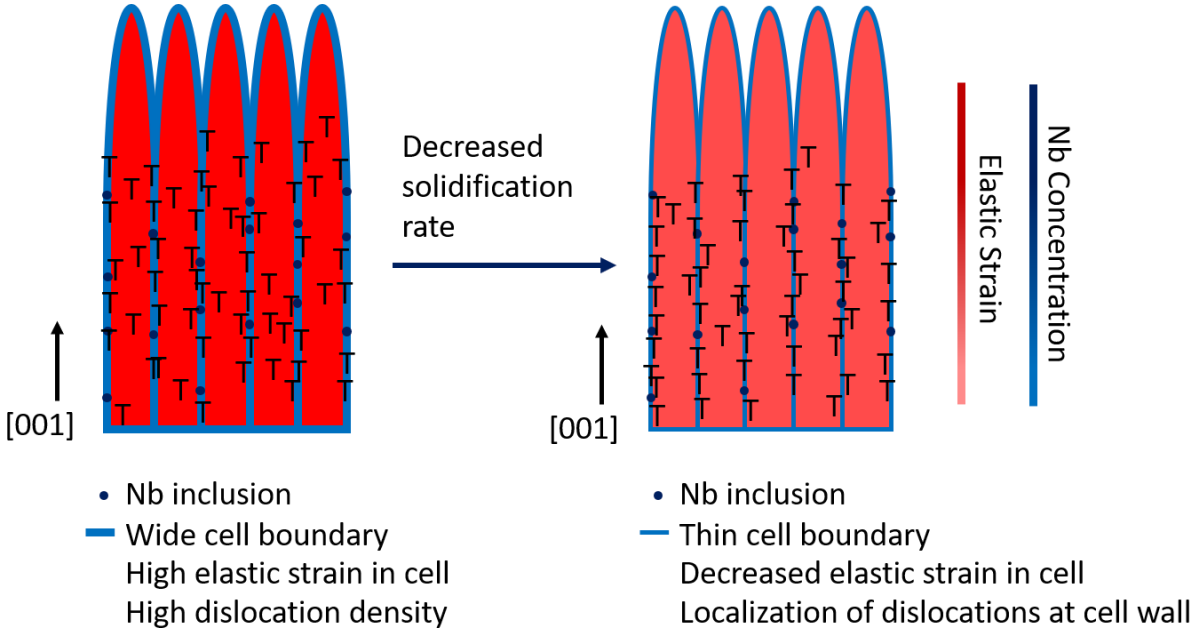

Figure 5-47. Evolution of non-equilibrium cells during L-PBF of IN625. High strain within diffuse cells drives dislocation movement toward walls with increased Nb content

Spatial analysis using MosaicIA resulted in a non-random spatial relationship between elastic strain and GND density in all locations analyzed by HR-EBSD. As proximity to the end of the track increased, the relationship between these two features increased as well. Dislocation density (HR-EBSD) does not significantly change throughout the build, however the organization of dislocations does. Elastic strain (HR-EBSD) increases significantly at relatively high thermal gradients and increased cooling rates. The strength of relationship between elastic strain and dislocation density increases with proximity to the end of the track and the elevated level of elastic strain within cells is distributed more heterogeneously. It also suggests that the elastic

strain and dislocations, when they are solidified relatively quickly, are ‘frozen’ near each other, neither has the time to move and so these are ‘metastable’ microstructures.

Due to computational constraints, and preliminary simulations which suggest the thermal profile in the single track does not change significantly until approximately 300um away from the end of the track, a single track of only 1mm long was modelled. The thermal environment defined by our CFD simulation is well withing the range of rapid solidification (RS) and the regime for cellular solidification under steep thermal gradients. In other thermal simulations of laser AM IN718, the thermal gradient has been reported to reach between 8,000-13,000 K/mm, while the solid can reach a thermal gradient of 7,000-12,000 K/mm after the laser has passed [47]. The difference in thermal gradient here can be attributed to the processing parameter of the laser, which resulted in relatively low volumetric energy density (VED) due to the speed of laser tracking.

Results from the DDD simulation mimic our experimental results when Nb and Mo segregation occurs as defined by [41,42]. The inputs of the DDD model are temperature and stress (from an FEM model of the laser track), showing that the level of stress within the melt pool does affect the level of dislocation organization. The level of Mo segregation was not seen to be as high here as in other laser processed Ni superalloys, but the level of Nb segregation and the presence of Nb heavy intermetallics along cell boundaries agree with simulations of cellular solidification during single track laser processing [5,9].

Conclusions

- Peak temperatures and cooling rates differ by location and effect stress state and evolution of dislocation cells
- Using thermal modeling combined with characterization, we have shown that the evolution of dislocation structures is dependent on increased time above elevated temperature (dislocations near the end of the track which solidified more quickly have less organization than those in the center of the track)
- Elastic strain characterization has also showed that increased elastic strain occurs under higher thermal gradients and faster cooling rates, as well as heterogeneous elastic strain distributions.
- Slower solidification rate results in dislocation movement driven by elastic strain within solidification cells, creating non-equilibrium dislocation dense structures where strain is localized at cell boundaries

References

[1] T. Voisin, J.-B. Forien, A. Perron, S. Aubry, N. Bertin, A. Samanta, A. Baker, Y.M. Wang, New insights on cellular structures strengthening mechanisms and thermal stability of an austenitic stainless steel fabricated by laser powder-bed-fusion, Acta Mater. 203 (2021) 116476. https://doi.org/10.1016/j.actamat.2020.11.018.

[2] K.N. Amato, S.M. Gaytan, L.E. Murr, E. Martinez, P.W. Shindo, J. Hernandez, S. Collins, F. Medina, Microstructures and mechanical behavior of Inconel 718 fabricated by selective laser melting, Acta Mater. 60 (2012) 2229–2239. https://doi.org/10.1016/j.actamat.2011.12.032.

[3] K.M. Bertsch, G. Meric de Bellefon, B. Kuehl, D.J. Thoma, Origin of dislocation structures in an additively manufactured austenitic stainless steel 316L, Acta Mater. 199 (2020) 19–33. https://doi.org/10.1016/j.actamat.2020.07.063.

[4] K.A. Small, Z. Clayburn, R. DeMott, S. Primig, D. Fullwood, M.L. Taheri, Interplay of dislocation substructure and elastic strain evolution in additively manufactured Inconel 625, Mater. Sci. Eng. A. 785 (2020) 139380. https://doi.org/10.1016/j.msea.2020.139380.

[5] S. Ghosh, L. Ma, L.E. Levine, R.E. Ricker, M.R. Stoudt, J.C. Heigel, J.E. Guyer, Single-Track Melt-Pool Measurements and Microstructures in Inconel 625, JOM. 70 (2018) 1011–1016. https://doi.org/10.1007/s11837-018-2771-x.

[6] Y.M. Wang, T. Voisin, J.T. McKeown, J. Ye, N.P. Calta, Z. Li, Z. Zeng, Y. Zhang, W. Chen, T.T. Roehling, R.T. Ott, M.K. Santala, P.J. Depond, M.J. Matthews, A. V. Hamza, T. Zhu, Additively manufactured hierarchical stainless steels with high strength and ductility, Nat. Mater. 17 (2018) 63–71. https://doi.org/10.1038/nmat5021.

[7] R. Ghiaasiaan, M. Muhammad, P.R. Gradl, S. Shao, N. Shamsaei, Superior tensile properties of Hastelloy X enabled by additive manufacturing, Mater. Res. Lett. 9 (2021) 308–314. https://doi.org/10.1080/21663831.2021.1911870.

[8] T. De Terris, O. Castelnau, Z. Hadjem-Hamouche, H. Haddadi, V. Michel, P. Peyre, Analysis of As-Built Microstructures and Recrystallization Phenomena on Inconel 625 Alloy Obtained via Laser Powder Bed Fusion (L-PBF), Metals (Basel). 11 (2021) 619. https://doi.org/10.3390/met11040619.

[9] T. Pinomaa, M. Lindroos, M. Walbrühl, N. Provatas, A. Laukkanen, The significance of spatial length scales and solute segregation in strengthening rapid solidification microstructures of 316L stainless steel, Acta Mater. 184 (2020) 1–16. https://doi.org/10.1016/j.actamat.2019.10.044.

[10] R. Jiang, A. Mostafaei, Z. Wu, A. Choi, P.-W. Guan, M. Chmielus, A.D. Rollett, Effect of heat treatment on microstructural evolution and hardness homogeneity in laser powder bed fusion of alloy 718, Addit. Manuf. 35 (2020) 101282. https://doi.org/10.1016/j.addma.2020.101282.

[11] A. Hussein, L. Hao, C. Yan, R. Everson, P. Young, Advanced lattice support structures for metal additive manufacturing, J. Mater. Process. Technol. 213 (2013) 1019–1026. https://doi.org/10.1016/j.jmatprotec.2013.01.020.

[12] L.A. Parry, I.A. Ashcroft, R.D. Wildman, Geometrical effects on residual stress in selective laser melting, Addit. Manuf. 25 (2019) 166–175. https://doi.org/10.1016/j.addma.2018.09.026.

[13] K.A. Small, M.L. Taheri, Role of Processing in Microstructural Evolution in Inconel 625: A Comparison of Three Additive Manufacturing Techniques, Metall. Mater. Trans. A. (2021). https://doi.org/10.1007/s11661-021-06273-x.

[14] T. Machirori, F.Q. Liu, Q.Y. Yin, H.L. Wei, Spatiotemporal variations of residual stresses during multi-track and multi-layer deposition for laser powder bed fusion of Ti-6Al-4V, Comput. Mater. Sci. 195 (2021) 110462. https://doi.org/10.1016/j.commatsci.2021.110462.

[15] A. Dutta, T.M. Park, J.-H. Nam, S.-I. Lee, B. Hwang, W.S. Choi, S. Sandlöbes, D. Ponge, J. Han, Enhancement of the tensile properties and impact toughness of a medium-Mn steel through the homogeneous microstrain distribution, Mater. Charact. 174 (2021) 110992. https://doi.org/10.1016/j.matchar.2021.110992.

[16] T.M. Rodgers, D. Moser, F. Abdeljawad, O.D.U. Jackson, J.D. Carroll, B.H. Jared, D.S. Bolintineanu, J.A. Mitchell, J.D. Madison, Simulation of powder bed metal additive manufacturing microstructures with coupled finite difference-Monte Carlo method, Addit. Manuf. 41 (2021) 101953. https://doi.org/10.1016/j.addma.2021.101953.

[17] X. Zhao, J. Chen, X. Lin, W. Huang, Study on microstructure and mechanical properties of laser rapid forming Inconel 718, Mater. Sci. Eng. A. 478 (2008) 119–124.

https://doi.org/10.1016/j.msea.2007.05.079.

[18] T.M. Rodgers, J.D. Madison, V. Tikare, Simulation of metal additive manufacturing microstructures using kinetic Monte Carlo, Comput. Mater. Sci. 135 (2017) 78–89. https://doi.org/10.1016/j.commatsci.2017.03.053.

[19] W.E. King, H.D. Barth, V.M. Castillo, G.F. Gallegos, J.W. Gibbs, D.E. Hahn, C. Kamath, A.M. Rubenchik, Observation of keyhole-mode laser melting in laser powder-bed fusion additive manufacturing, J. Mater. Process. Technol. 214 (2014) 2915–2925. https://doi.org/10.1016/j.jmatprotec.2014.06.005.

[20] S.K. Nayak, S.K. Mishra, C.P. Paul, A.N. Jinoop, K.S. Bindra, Effect of energy density on laser powder bed fusion built single tracks and thin wall structures with 100 μm preplaced powder layer thickness, Opt. Laser Technol. 125 (2020) 106016. https://doi.org/10.1016/j.optlastec.2019.106016.

[21] I. Yadroitsev, P. Krakhmalev, I. Yadroitsava, S. Johansson, I. Smurov, Energy input effect on morphology and microstructure of selective laser melting single track from metallic powder, J. Mater. Process. Technol. 213 (2013) 606–613. https://doi.org/10.1016/j.jmatprotec.2012.11.014.

[22] R. Shi, S. Khairallah, T. Wook Heo, M. Rolchigo, J.T. Mckeown, M.J. Matthews, Integrated Simulation Framework for Additively Manufactured Ti-6Al-4V: Melt Pool Dynamics, Microstructure, Solid-State Phase Transformation, and Microelastic Response, JOM. 71 (2019) 3640–3655. https://doi.org/10.1007/s11837-019-03618-1.

[23] M. Gerstgrasser, R. Jakob, K.S. Pandya, J. Stirnimann, K. Wegener, CA single track microstructure simulation of nickel base alloy CM247LC and stainless steel S316L, including experimental validation of S316L, Mater. Des. 199 (2021) 109395. https://doi.org/10.1016/j.matdes.2020.109395.

[24] M. Lindroos, T. Pinomaa, A. Antikainen, J. Lagerbom, J. Reijonen, T. Lindroos, T. Andersson, A. Laukkanen, Micromechanical modeling approach to single track deformation, phase transformation and residual stress evolution during selective laser melting using crystal plasticity, Addit. Manuf. 38 (2021) 101819. https://doi.org/10.1016/j.addma.2020.101819.

[25] E.A. Lass, M.R. Stoudt, M.E. Williams, M.B. Katz, L.E. Levine, T.Q. Phan, T.H. Gnaeupel-Herold, D.S. Ng, Formation of the Ni3Nb δ-Phase in Stress-Relieved Inconel 625 Produced via Laser Powder-Bed Fusion Additive Manufacturing, Metall. Mater. Trans. A Phys. Metall. Mater. Sci. 48 (2017) 5547–5558. https://doi.org/10.1007/s11661-017-4304-6.

[26] S. Qin, T.C. Novak, M.K. Vailhe, Z.-K. Liu, A.M. Beese, Plasticity and fracture behavior of Inconel 625 manufactured by laser powder bed fusion: Comparison between as-built and stress relieved conditions, Mater. Sci. Eng. A. 806 (2021) 140808. https://doi.org/10.1016/j.msea.2021.140808.

[27] G. Marchese, S. Parizia, M. Rashidi, A. Saboori, D. Manfredi, D. Ugues, M. Lombardi, E. Hryha, S. Biamino, The role of texturing and microstructure evolution on the tensile behavior of heat-treated Inconel 625 produced via laser powder bed fusion, Mater. Sci. Eng. A. 769 (2020) 138500. https://doi.org/10.1016/j.msea.2019.138500.

[28] BYU - OpenXY, (2018). https://github.com/BYU-MicrostructureOfMaterials/OpenXY.

[29] A.C. Leff, C.R. Weinberger, M.L. Taheri, Estimation of dislocation density from precession electron diffraction data using the Nye tensor, Ultramicroscopy. 153 (2015) 9–21.

https://doi.org/10.1016/j.ultramic.2015.02.002.

[30] A. Shivanandan, A. Radenovic, I.F. Sbalzarini, MosaicIA: an ImageJ/Fiji plugin for spatial pattern and interaction analysis, BMC Bioinformatics. 14 (2013) 349. https://doi.org/10.1186/1471-2105-14-349.

[31] M. Bayat, A. Thanki, S. Mohanty, A. Witvrouw, S. Yang, J. Thorborg, N.S. Tiedje, J.H. Hattel, Keyhole-induced porosities in Laser-based Powder Bed Fusion (L-PBF) of Ti6Al4V: High-fidelity modelling and experimental validation, Addit. Manuf. 30 (2019) 100835. https://doi.org/10.1016/j.addma.2019.100835.

[32] Y.S. Lee, W. Zhang, Modeling of heat transfer, fluid flow and solidification microstructure of nickel-base superalloy fabricated by laser powder bed fusion, Addit. Manuf. 12 (2016) 178–188. https://doi.org/10.1016/j.addma.2016.05.003.

[33] Y.-C. Wu, C.-H. San, C.-H. Chang, H.-J. Lin, R. Marwan, S. Baba, W.-S. Hwang, Numerical modeling of melt-pool behavior in selective laser melting with random powder distribution and experimental validation, J. Mater. Process. Technol. 254 (2018) 72–78. https://doi.org/10.1016/j.jmatprotec.2017.11.032.

[34] S.A. Khairallah, A.T. Anderson, A. Rubenchik, W.E. King, Laser powder-bed fusion additive manufacturing: Physics of complex melt flow and formation mechanisms of pores, spatter, and denudation zones, Acta Mater. 108 (2016) 36–45. https://doi.org/10.1016/j.actamat.2016.02.014.

[35] A. Arsenlis, W. Cai, M. Tang, M. Rhee, T. Oppelstrup, G. Hommes, T.G. Pierce, V. V Bulatov, Enabling strain hardening simulations with dislocation dynamics, Model. Simul. Mater. Sci. Eng. 15 (2007) 553–595. https://doi.org/10.1088/0965-0393/15/6/001.

[36] A.M. Hussein, S.I. Rao, M.D. Uchic, D.M. Dimiduk, J.A. El-Awady, Microstructurally based cross-slip mechanisms and their effects on dislocation microstructure evolution in fcc crystals, Acta Mater. 85 (2015) 180–190. https://doi.org/10.1016/j.actamat.2014.10.067.

[37] No Title, (n.d.) 463–473.

[38] C. Varvenne, A. Luque, W.A. Curtin, Theory of strengthening in fcc high entropy alloys, Acta Mater. 118 (2016) 164–176. https://doi.org/10.1016/j.actamat.2016.07.040.

[39] C. Varvenne, G.P.M. Leyson, M. Ghazisaeidi, W.A. Curtin, Solute strengthening in random alloys, Acta Mater. 124 (2017) 660–683. https://doi.org/10.1016/j.actamat.2016.09.046.

[40] G.P.M. Leyson, W.A. Curtin, Solute strengthening at high temperatures, Model. Simul. Mater. Sci. Eng. 24 (2016) 065005. https://doi.org/10.1088/0965-0393/24/6/065005.

[41] F. Zhang, L.E. Levine, A.J. Allen, M.R. Stoudt, G. Lindwall, E.A. Lass, M.E. Williams, Y. Idell, C.E. Campbell, Effect of heat treatment on the microstructural evolution of a nickel-based superalloy additive-manufactured by laser powder bed fusion, Acta Mater. 152 (2018) 200–214. https://doi.org/10.1016/j.actamat.2018.03.017.

[42] M. Rozmus-Górnikowska, Ł. Cieniek, M. Blicharski, J. Kusiński, Microstructure and Microsegregation of an Inconel 625 Weld Overlay Produced on Steel Pipes by the Cold Metal Transfer Technique, Arch. Metall. Mater. 59 (2014) 1081–1084. https://doi.org/10.2478/amm-2014-0185.

[43] O.N. Senkov, D.B. Miracle, Effect of the atomic size distribution on glass forming ability of amorphous metallic alloys, Mater. Res. Bull. 36 (2001) 2183–2198. https://doi.org/10.1016/S0025-5408(01)00715-2.

[44] S. Keshavarz, S. Ghosh, Hierarchical crystal plasticity FE model for nickel-based superalloys: Sub-grain microstructures to polycrystalline aggregates, Int. J. Solids Struct. 55 (2015) 17–31. https://doi.org/10.1016/j.ijsolstr.2014.03.037.

[45] G. Fleury, F. Schubert, H. Nickel, Modelling of the thermo-mechanical behaviour of the single crystal superalloy CMSX-4, Comput. Mater. Sci. 7 (1996) 187–193. https://doi.org/10.1016/s0927-0256(96)00079-1.

[46] P.J. Withers, Residual stress and its role in failure, Reports Prog. Phys. 70 (2007) 2211–2264. https://doi.org/10.1088/0034-4885/70/12/R04.

[47] M. V Pantawane, S. Sharma, S. Dasari, S.A. Mantri, A. Sharma, R. Banerjee, S. Banerjee, N.B. Dahotre, Spatial Variation of Thermokinetics and Associated Microstructural Evolution in Laser Surface Engineered IN718: Precursor to Additive Manufacturing, Metall. Mater. Trans. A. 52 (2021) 2344–2360. https://doi.org/10.1007/s11661-021-06227-3.

[48] T.W. Heo, S.A. Khairallah, R. Shi, J. Berry, A. Perron, N.P. Calta, A.A. Martin, N.R. Barton, J.D. Roehling, T. Roehling, J.-L. Fattebert, A. Anderson, A.L. Nichols, S. Wopschall, W.E. King, J.T. McKeown, M. Matthews, A mesoscopic digital twin that bridges length and time scales for control of additively manufactured metal microstructures, J. Phys. Mater. (2021) 11–14. https://doi.org/10.1088/2515-7639/abeef8.

[49] B. Farber, K.A. Small, C. Allen, R.J. Causton, A. Nichols, J. Simbolick, M.L. Taheri, Correlation of mechanical properties to microstructure in Metal Laser Sintering Inconel 718, Mater. Sci. Eng. A. 712 (2018) 539–547. https://doi.org/10.1016/j.msea.2017.11.125.

[50] A.T. Polonsky, M.P. Echlin, W.C. Lenthe, R.R. Dehoff, M.M. Kirka, T.M. Pollock, Defects and 3D structural inhomogeneity in electron beam additively manufactured Inconel 718, Mater. Charact. 143 (2018) 171–181. https://doi.org/10.1016/j.matchar.2018.02.020.

Chapter 6. Conclusions

Using a combination of electron microscopy, statistical analysis and computer simulation, this thesis aimed to address each of these gaps in understanding of laser processing microstructures:

1. The use of lasers for direct part marking (DPM) is common in medicine and transportation, but there is not sufficient research to determine whether these markings effect the microstructure or mechanical properties of a component.
2. Residual stress is a known drawback of AM techniques, and type III strains are important for the material properties of a system. However, the microstructure of AM techniques results in high intragranular misorientation and leads to unreliable measurement of this feature using HR-EBSD cross-correlation.
3. AM techniques vary widely in raw material and in processing parameters, giving rise to microstructures that are unique to each individual method. The relative type III strains and dislocation densities, as well as other microstructural features including misorientation and cell structures, have not been explicitly tied to the relative thermal environments across different techniques. There is currently no statistical description of the relationship between microstructural features resulting from different thermal environments in AM.
4. The thermal environment during laser processing, including AM, varies based on location giving rise to anisotropic microstructures and strain distributions. The evolution of dislocation structures and elastic strain has not been linked to the temperature gradients and cooling rates within the laser melt pool.

Fatigue testing was performed on laser engraved P/M FC-0208 to demonstrate the effects of surface laser processes on bulk fatigue life. Laser engraved samples resulted in a 50% decrease in fatigue life under high cycle fatigue, and a significantly decreased life in low cycle fatigue. FC-0208 was laser engraved using two different sets of parameters, specifically, the number of laser passes varied between light engraving (LE, one laser pass) and deep engraving (DE, five laser passes), to determine whether DPM could be optimized to result in visible marking without the altered surface microstructure. It was found that the extent of laser processing impacted the presence of martensite at the surface, providing guidance for DPM and laser processing for precision microstructural modification. This shows that the number of laser passes can be chosen in order to use surface laser processing for local microstructural modification of for DPM without altering the microstructure.

The presence of high intragranular misorientation in laser processes materials lead to high levels of phantom strain during HR-EBSD cross-correlation. In order to optimize this method of strain characterization for complex materials, a rotation tolerance was added to the open source software OpenXY [1]. This rotation tolerance enables the measurement of elastic strain in metals with high intragranular misorientation and allows the description of microstructure under varying thermal environments when combined with computer simulation and dislocation density calculation. The resulting cross-correlation algorithm can now be applied to laser processed materials for calculation of elastic strain.

While it is known that different methods of AM lead to characteristic microstructures, the relative levels of microscale strain and dislocation density had not been reported. In this thesis, the use of three different AM methods with widely varying thermal histories allowed

relative levels of elastic strain and dislocation density to be measured. Additionally, the description of spatial distribution was quantified in varying thermal environments, with L-PBF showing a high spatial relationship between elastic strain and dislocation density, while decreasing temperatures and cooling rates resulted in significantly decreased spatial relationship between the two. Defining the spatial relationship of these difficult-to-characterize features will enable future microstructural descriptors to be used in predictive simulations and ML algorithms.

The dislocation cells and elastic strains typical of laser processed and laser AM metals have been widely reported. Despite this, their development is not well understood and so the manipulation of these features for bulk properties cannot be usefully implemented. Using thermal simulations, DDD modeling and elastic strain and dislocation density measurement, this thesis demonstrated in-process evolution of dislocation cells as well as elastic strain levels and organization. The change from heterogeneous to homogeneous distribution of elastic strain under high and low thermal gradients, respectively, suggest that elastic strain is a key driver of cell formation during laser processing.

The characterization methods outlined in this research provide a path for the full characterization of laser processed and laser AM alloys. Future work on predicting AM microstructures can benefit from the statistical analysis combined with characterization in AM, providing microstructural descriptors for AM components which will be useful in development of machine learning (ML) algorithms. Already, dislocation simulations depend on the stress state of the material as predicted by FEM (as discussed in Chapter 5); however, the stresses predicted by FEM are of type II (grain level residual stresses). Future microstructural

simulations could use subgrain level, type III, strains to predict the microstructural evolution under laser processing conditions to arrive at even more accurate microstructural and material properties. The improvement of predictive simulations and ML frameworks using these results will not only impact the way industries which use laser AM, including automotive, biomedical and aerospace, prepare for fabrication of complex parts, but also the design process for parts requiring surface laser melting or local properties. The knowledge of the extent of phase transformation with the extent of laser engraving as well as the knowledge of microscale strain distribution with exposure to certain thermal environments will improve the fabrication process of laser AM components.

Future Work

While the results presented in this thesis have an impact on the manufacturing and design process in several industries, the AM community still has several open questions regarding elastic strain, dislocation cells, and material properties. The characterization methods outlined here can help to uncover further process-microstructure relationships during laser processing. For one, the role of solute segregation on the stability of these cell structures is not understood. Preliminary results using pure Ni and IN625 under laser surface processing and L-PBF suggest that alloying elements are necessary for the formation of dislocation cells during laser processing. The necessity of alloying elements for the formation of dislocation cells would fit the mechanism of cellular solidification in the presence of high thermal gradients and would provide space for dislocations to congregate, while the absence of solute cell walls may result in slightly lower dislocation density because dislocations are not trapped in the cell walls. Additionally, the cell boundaries reported here are known the be non-equilibrium, in the sense

that under further heating they can be processed away. The character of the non-equilibrium features should be observed more fully if their contribution to mechanical and material properties is to be fully understood or engineered for desired components.